GEOCELLULAR CONFINEMENT SYSTEMS IN LOW-VOLUME PAVED ROADS

by

BRANDON STALLONE BORTZ

B.S., Kansas State University, 2008
M.S., Kansas State University, 2010

AN ABSTRACT OF A DISSERTATION

submitted in partial fulfillment of the requirements for the degree

DOCTOR OF PHILOSOPHY

Department of Civil Engineering
College of Engineering

KANSAS STATE UNIVERSITY
Manhattan, Kansas

2015

Abstract

Geocellular confinement systems (geocells), three-dimensional honeycomb-like structures containing an infill of available materials such as sand or crushed limestone, vastly improve shear strength of infill materials. Geocells are potential solutions for challenges associated with low-volume paved road reconstruction. The objectives of this study were to test geocell designs with various infill materials and a thin hot-mix asphalt overlay under full-scale traffic load and to numerically model this problem. Therefore, eight pavement test sections were constructed at the Civil Infrastructure System Laboratory at Kansas State University, Manhattan, Kansas. Repeated loads (80-kN, single axle) were applied to the pavement sections using an accelerated pavement testing machine till failure. Pavement sections were modeled three-dimensionally using Abaqus, a commercially available finite element software package. Effects of geocell height and location were simulated in the geocell-reinforced bases, and pavement structures were modeled as three-layered systems. Results showed that proper geocell height, infill material and cover depth to protect the geocells during construction are necessary to ensure long-term performance of geocell-reinforced pavements. Such pavement structures with low-quality infill materials can perform as well as conventionally-constructed pavement structures.

GEOCELLULAR CONFINEMENT SYSTEMS IN LOW-VOLUME PAVED ROADS

by

BRANDON STALLONE BORTZ

B.S., Kansas State University, 2008
M.S., Kansas State University, 2010

A DISSERTATION

submitted in partial fulfillment of the requirements for the degree

DOCTOR OF PHILOSOPHY

Department of Civil Engineering
College of Engineering

KANSAS STATE UNIVERSITY
Manhattan, Kansas

2015

Approved by:

Major Professor
Dr. Mustaque Hossain

Copyright

Abstract

Geocellular confinement systems (geocells), three-dimensional honeycomb-like structures containing an infill of available materials such as sand or crushed limestone, vastly improve shear strength of infill materials. Geocells are potential solutions for challenges associated with low-volume paved road reconstruction. The objectives of this study were to test geocell designs with various infill materials and a thin hot-mix asphalt overlay under full-scale traffic load and to numerically model this problem. Therefore, eight pavement test sections were constructed at the Civil Infrastructure System Laboratory at Kansas State University, Manhattan, Kansas. Repeated loads (80-kN, single axle) were applied to the pavement sections using an accelerated pavement testing machine till failure. Pavement sections were modeled three-dimensionally using Abaqus, a commercially available finite element software package. Effects of geocell height and location were simulated in the geocell-reinforced bases, and pavement structures were modeled as three-layered systems. Results showed that proper geocell height, infill material and cover depth to protect the geocells during construction are necessary to ensure long-term performance of geocell-reinforced pavements. Such pavement structures with low-quality infill materials can perform as well as conventionally-constructed pavement structures.

Table of Contents

List of Figures

List of Tables

Acknowledgements

Thanks are not enough for everyone that has helped on this journey. Dr. Mustaque Hossain has been a great supporter of mine since I arrived at Kansas State University as a freshman in 2004. He has always believed that I could do more than I thought possible. All of his roles as teacher, mentor, cheerleader, peer, motivator, and friend could not have been easy, but he has always been there for me.

The Department of Civil Engineering and UTC have given me the opportunity to complete this dissertation though tuition support, financial support, and job opportunities. Thanks have to be given to the faculty and staff of the civil engineering department for their continual support throughout my time here. Mrs. Jeanette Grauerholz and Mrs. Danita Deters have always had a smile when I had a question or needed help from them.

I sincerely thank Steven Hammerschmidt, Joey Holste, Luke McIntosh, Randy Testa, Ryan Benteman, Lisa Burris, Andrew Wiederholt, Milad Saghebfar, Nassim Sabahfar, and Quinn Jacobs. A small village is needed to help in the varying aspects of a project of this magnitude and these people were willing and did go beyond the call of duty. My wife, Cari, knew I was a little out there when we met, but she has been very supportive throughout this process. She wouldn't complain when she did my asphalt-covered laundry or the interruptions of date nights to check the "Machine" at CISL. I am very lucky to have a wife like her.

I have to thank all the companies for their donations to this project, especially PRS Mediterranean Ltd, Shilling Construction, KDOT, C.B. Farms, and MCM. Because companies such as these are willing to share knowledge, supplies, and time, these projects can be successful.

Jim and June Klotz have taken me in like a child of their own and have been my Manhattan parents. They have been great supporters of my work and my family. A friend once said about my family, "Thanksgiving dinner at your house is all about not being the child who did the least." This statement is mostly true. Amber, Darnell, and I have always pushed each other in all aspects of our lives. We have always been there for each other. My parents have been an inspiration to me throughout my life and have always pushed me to succeed.

Dedication

This dissertation is dedicated to my Dad. Since the first day of kindergarten Dad has told me, “Be good have fun. Do it right the first time, on time, every time.” This advice has served me well.

Chapter 1 - Introduction

1.1 Research Background

Low-volume roads account for approximately 80% of the world's road infrastructure. A majority of these roads are farm-to-market roads that tend to be thin hot-mix asphalt (HMA) pavements as a result of lower initial capital costs. Reduced transportation budgets have motivated highway and road agencies to seek new innovations in reconstruction of pavements and other road structures. Currently, most road reconstruction consists of stabilizing the subgrade via mechanical compaction, adding a stabilizing agent such as cement or lime or a combination of the two, and then applying a thick, high quality base layer such as crushed stone over the subgrade before placing the HMA layer. However, geosynthetics have been promoted to reinforce geomaterials in various layers in the road structure, including the road base.

The American Society for Testing and Materials (ASTM) defines geosynthetics as "a planar product manufactured from polymeric material used with soil, rock, earth, or other geotechnical engineering-related material as an integral part of a man-made project, structure, or system (ASTM 4439 2004)." Various types of geosynthetics have varying functions that can be grouped as separation, reinforcement, filtration, drainage, and containment (Koerner 2005). Material engineers have been researching geosynthetics in pavement structures since the mid-1970s. A combination of geotextile and geo-grid reinforcements has been shown to increase bearing capacity of the road structure when placed over a weak subgrade.

Geocellular confinement systems (geocells) are a type of geosynthetics that have garnered increased interest in reinforcement for base courses of pavement structures. Earlier geocells were comprised of high-density polyethylene (HDPE) strips 200 mm (8 in.) wide and approximately 1.2 mm (50 mils) thick (Koerner 1994). They are ultrasonically welded along their 200-mm width (8 in.) at approximately 33 cm (13 in.) intervals and are shipped to the job site in a collapsed configuration, as shown in Figure 1-1. At the job site they are placed directly on the subgrade and propped open in an accordion fashion with an external stretcher assembly. The section shown in Figure 1-1 expands into a 2.4 meter x 6.1 meter (8 ft. x 20 ft.) series of 561 cells, each approximately 200 mm (8 in.) in diameter. They are then filled with infill materials and compacted using a hand-operated, vibratory plate compactor (Koerner 1994).

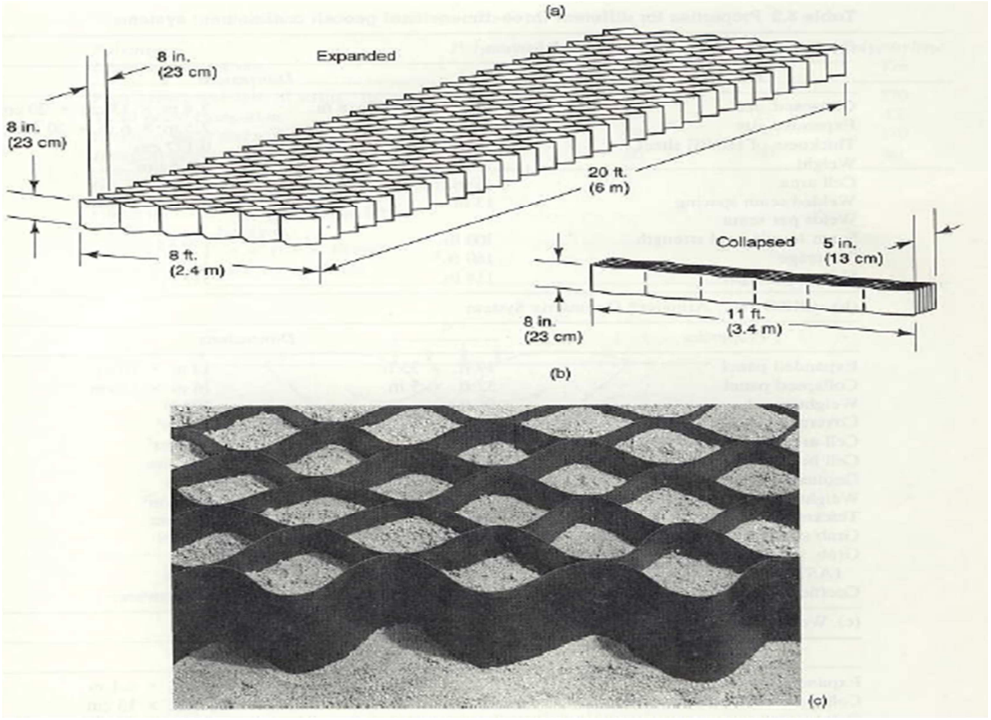

Figure 1-1 Geocell materials (Koerner 1994)

1.2 Problem Statement

Because of their three-dimensional (3-D) structure, geocells currently have more widespread use for confinement applications than any other planar geosynthetic reinforcement (Yuu et al. 2008). However, most studies have demonstrated use of geocells for increasing bearing capacity and reducing settlement of soft soil foundations (Dash et al. 2001a, 2001b, 2003, and 2004, and Sitharam et al. 2005). Bathurst and Jarrett (1988) showed that geocell-reinforced bases had higher load capacity when compared to soft-peat subgrades. Geocells can stiffen the base layer, reducing normal stresses while reorienting shear stresses on the subgrade that limit lateral movement of base material and subgrade soil (Giroud and Han 2004 a).

Although these studies have demonstrated that geocells provide higher degree of soil confinement and potentially enhance the performance of base courses on weak subgrade, use of geocells in unpaved and paved roads is still limited due to lack of accepted design methods and research (Yuu et al. 2008). Giroud and Han (2004a and 2004b) developed a theoretical equation for the thickness of a base layer incorporating planar geogrid–reinforced unpaved roads.

Pokharel (2010) adjusted the Giroud and Han equation to design unpaved roads with geocell-reinforced base layer.

Geocells are advantageous because they reduce base and HMA layer thicknesses needed over a marginal or weak subgrade. In addition, because geocells have a confining nature, low-quality infill materials such as reclaimed asphalt pavement (RAP) and quarry waste can be used in geocells. Therefore, geocells are a potential economical option for rehabilitation of pavements, including rehabilitation of low-volume roads.

1.3 Research Objectives

The objectives of this study are:

- To test a geocell design with various infill materials and a thin HMA layer under simulated full-scale traffic on a marginal subgrade using accelerated pavement testing (APT).

- To develop a finite element (FE) model for geocell-reinforced paved roads with consideration of the quality of the infill material so that design of such pavements can be studied.

1.4 Hypothesis

The author believes that geocells confine geomaterials and do not allow movement of the infill. When the infill reaches a certain density, the base layer behaves like a slab. The "slab" effect reduces the vertical stress on the subgrade and the shear stress in the infill/base layer.

1.5 Scope of the Research Program

For this study, eight test sections were built in two pits at the Kansas State University (KSU) Civil Infrastructure System Laboratory (CISL). Two experiments of four test sections each were conducted. Each experiment consisted of three sections with three infill materials (quarry waste, crushed limestone (AB-3), and RAP) in the geocellular reinforcement and one unreinforced control section with an AB-3 base layer. The accelerated pavement testing (APT) machine was used to apply repeated moving-wheel loads to the test sections. The original design

had thinner cross sections and failed rapidly. Therefore, thicker sections were designed, constructed, and tested.

A 3-D FE model was developed using commercial FE software, Abaqus. The developed model, calibrated with results found from the CISL tests, was used to study the design of geocell-reinforced pavements. A flowchart of the work completed in this study is shown in **Error! Reference source not found.**.

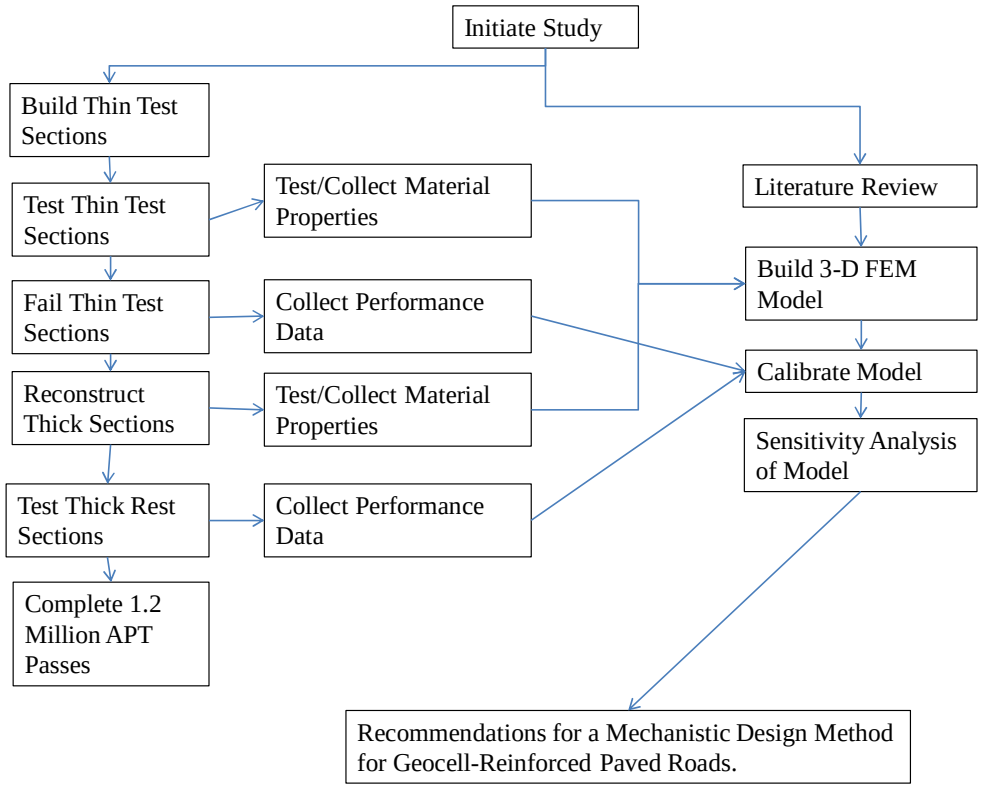

Figure 1-2 Study Flowchart

1.6 Dissertation Outline

This dissertation is divided into eight chapters. Chapter 1 includes research background, problem statement, objectives of the study, hypothesis, scope of the study, and dissertation outline. Chapter 2 contains the review of relevant literature, and Chapter 3 describes the properties of materials used in the study. Chapter 4 explains the APT testing of this study, and Chapter 5 details the numerical simulation of the APT testing. Chapter 6 compares results of the APT testing and numerical simulation. Chapter 7 presents conclusions and recommendations based on this study.

Chapter 2 - Literature Review

2.1 Low-Volume Roads

A precise definition of low-volume roads is difficult to formulate due to complex usage of these roads. Therefore, the definition of low-volume roads is typically based on the function of the road. Approximately 80% of the world's transportation infrastructure is estimated to be low-volume (Tingle and Jersey 2007). The American Association of State Highway and Transportation Officials (AASHTO) defines very low-volume roads as roads with average daily traffic (ADT) less than 400 (AASHTO 2001). Depending on population and traffic, some state departments of transportation (DOTs) consider any route less than 5,000 ADT to be a low-volume road. However, for county authorities, an ADT of 1,000 to 2,000 is a more useful definition of a low-volume road (personal communication, Michael Long 2011). Although low-volume roads tend to be unpaved, increased traffic volume often includes paved roads classified as low-volume. Farm-to-market roads, which are vital to transport agricultural products, tend to have very low volumes of traffic during majority of the year, but these roads experience a significant jump in traffic volume during planting and harvesting times.

2.2 Geocellular Confinement Systems

Geocellular confinement systems (geocells) are 3-D honeycomblike structures that contain an infill of granular material, as shown in Figure 2-1. Such containment (or confinement) vastly improves the shear strength of granular materials. Geocells are comprised of strips of polymer sheet or geotextile connected at staggered points, resulting in formation of a large honey-combed mat when the strips are pulled apart. Geocells provide physical containment of infill geo material and a path for load transfer (Koerner 2005).

Figure 2-1 Geocellular confinement

2.2.1 Geocell Testing

Webster and Watkins (1977), Webster and Alford (1978), and Webster (1979a and 1979b) were among the first researchers to investigate the feasibility of a 3-D soil confinement structure. The researchers primarily focused on military use in poorly-graded beach sand. Investigations considered material properties and geocell geometry. Major conclusions from these investigations stated that geocells must be protected by adequate "surfacing" or cover and that geocell performance is related to geocell size and type of sand used as infill. Many subsequent studies have analyzed multiple aspects of geocells. A majority of the studies can be categorized as one of the following seven areas of study focus: geometric ratio of geocell (Rea and Mitchell 1978, Shimizu and Inui 1990, Mhaiskar and Mandal 1992a, 1992b, 1994, 1996, Mandal and Gupta 1994); failure mechanism (Mitchell et al. 1979); properties of geocell (Shimizu and Inui 1990, Dash et al. 2001a, 2001b); effectiveness of geocell (Bathurst and Jarrett 1988, Dash et al. 2003, 2004); loading area, position, and type (Rea and Mitchel 1978, Shimizu and Inui 1990, Mhaiskar and Mandal 1992a, 1992b, 1994, 1996, Chang et al. 2007 and 2008);, infill density (Mhaiskar and Mandal 1992a, 1992b, 1994, 1996, Dash et al. 2001a, 2001b); type

and size of geocell (Dash et al. 2001a, 2001b). Testing in most geocell studies can be grouped into three test types: as triaxial compression tests, laboratory model tests, and field tests.

2.2.1.1 Triaxial Compression Tests

Bathurst and Karpurapu (1993) were among the first researchers to suggest that geocells behave similarly to the elastic membrane model (Henkel and Gilbert 1952). That model proposes addition of apparent cohesion (c_r), as shown in Equation (2-1). Figure 2-1 shows a model that relates the composite geocell-infill Mohr-Coulomb strength to the unreinforced infill. Triaxial compression tests were conducted on single composite specimens consisting of geocell-reinforced infill. These tests used the confinement effect to show the stiffening effect and strength increase of the soil.

$$c_r = \frac{\Delta\sigma_3}{2}\tan\left[\frac{\pi}{4}+\frac{\emptyset}{2}\right] \tag{2-1}$$

Where $\Delta\sigma_3$ = additional confining stress induced by geocell confinement, and $\emptyset$ = peak friction angle of the infill soil.

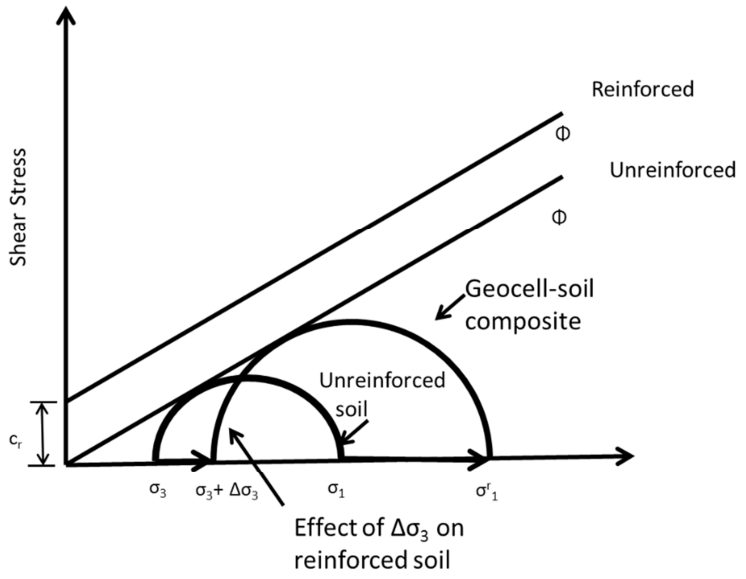

Figure 2-2 Mohr circles for apparent cohesion of geocell-infill composite (after Bathurst and Karpurapu 1993)

Gourves et al. (1996) compared the triaxial compression test to a composite FE model of a single geocell-reinforced cell. Triaxial compression test results showed the stiffening effect and

strength increase due to confinement, and the FE model was able to accurately reproduce the results of the above-mentioned triaxial compression test.

Rajagopal et al. (1999) supported the apparent cohesion effect while studying geocell confinement on single and multiple geocells. In their study, the tensile modulus of the geocell dictated the induced apparent cohesive strength. The conclusion was made that use of a single cell during triaxial compression tests did not represent accurate behavior of geocell-reinforced soils. Therefore, a minimum of three interconnected cells was suggested to represent a geocell-reinforced infill.

2.2.1.2 Laboratory Model Tests

In laboratory model tests, geocells are placed into a soil box and loaded with static or dynamic loads. The study focus dictates setup of the subgrade layer, reinforced layer, and cover. The following section provides chronological history of the major findings of studies that used geocells to reinforce an infill layer in laboratory model tests.

Rea and Mitchell (1978) used square-shaped paper cells in plate-loading tests in a soil box. Tests were used to identify various modes of failure and to arrive at optimum dimensions of cells. Results from this study indicated that geocell failures were generally sudden and well-defined and typically occurred as a result of reinforcement rupture. Ultimate bearing capacity of the geocell increased with subgrade stiffness, geocells improved resistance to repeated loads, and infill in geocells could be lost during repeated loading due to lack of cover layer. Mitchell et al. (1979) identified seven failure modes of geocells:

1. Penetration of cell into the subgrade underlying layer
2. Bursting of the cell when infill stressed the geocell wall
3. Buckling of the cell wall
4. Bearing capacity failure due to shear failure of the subgrade
5. Bending failure
6. Durability failure
7. Excessive rutting

Jamnejad et al. (1986) demonstrated advantages of geocell reinforcement in pavement construction; geocell reinforcement showed an increase in stiffness and a failure load that correlated to increased infill density. Elastic properties of the base layer also increased with geocells, and the reinforced layer had retarded cyclic degradation. The study also included

investigation of failure modes; filled cells failed by buckling, while unfilled cells failed at welds as a result of bursting. Similarly, Kazerani and Jamnejad (1987) demonstrated an improvement in stress-distributing characteristics of poorly-graded materials. Their study concluded that base layer thickness when using geocells could be reduced by 20-30% leading to savings in construction.

de Garidel and Morel (1986) conducted tests on geocell-reinforced base layers on a weak subgrade (CBR = 3.0). Rigidity of the base layer increased when a large-displacement load was applied; however, the increase in rigidity was not observed when a small-displacement load was applied. Bathurst and Jarrett (1988) demonstrated improved bearing capacity; stiff geocells performed better, potentially leading to a 40-50% reduction in base thickness.

Shimizu and Inui (1990) also showed an increase in bearing capacity of the base layer when reinforced with geocells. This study was unique because lead particles in the cells were x-rayed, thereby allowing particle movements in the cells to be tracked. X-rays showed that particles were constrained by geocells at small displacements, but particles were able to pass under the cell wall at large displacements. Bearing capacity was found to increase when cell height increased, and horizontal stiffness of the geocell material was found to control the extent of bearing capacity increase.

Mhaiskar and Mandal (1992a, 1992b, 1994, and 1996) investigated the effect of the geocell's geometric ratio and infill soil density during static and dynamic loading. Their tests concluded that a higher height-to-width ratio of the geocell, higher density of the infill, and higher modulus of geocell material corresponded to better performance of the base layer. In addition, geocell-reinforced sand layers were shown to outperform sand layers reinforced with planar reinforcement. Mandal and Gupta (1994) also showed that increased cell height is directly related to higher bearing capacity. Settlement ratio in this study was defined as the settlement-to-width ratio of the load plate. Geocell-reinforced sand showed beam action when the settlement ratio was 5-10% and a membrane effect when the settlement ratio was over 20%.

Dash et al. (2001a) investigated use of geocells in strip footings, specifically the influence of factors such as pattern of geocell formation, cell opening, height and width of geocells, depth of geocells, tensile stiffness, and relative density of infill material. Investigators found that bearing capacity could be increased up to eight times the capacity for the unreinforced section. However, tensile stiffness of the geocell showed very little influence on bearing

capacity. In order to intercept failure planes, the recommendation was made that the ratio of geocell width to the footing width should be 4.0. High infill density correlated with better structural performance of strip footings. Dash et al. (2001b) added additional planar geosynthetic reinforcement in similar tests. When additional reinforcement was placed at the bottom of the geocells, bearing capacity increased; however, when planar reinforcement was placed on top of the geocells, no noticeable increase in bearing capacity was observed.

Dash et al. (2003) conducted testing on circular footings with geocell-reinforced bases. Use of geocells showed increases in bearing capacity with reduced surface heaving. Dash et al. (2004) compared geocells to other geosynthetic reinforcement. Geocell advantages include better composite material, redistribution of the load, and reduction of heaving and settlement.

Madhavi Latha et al. (2006) conducted studies on the performance of geocell-reinforced earth embankments constructed over weak soil. A theoretical model, as shown in Equation (2-2), was suggested to calculate cohesive strength of a geocell-reinforced composite based on membrane stress in the wall of the geocell.

$$c_r = \frac{\Delta\sigma_3}{2}\sqrt{k_p} \tag{2-2}$$

where

c_r = additional cohesive strength of geocell

k_p = coefficient of passive earth pressure

$\Delta\sigma_3$ = additional confining stress provided by geocell membrane.

$$\Delta\sigma 3 = \frac{2M}{D_0} * \frac{1-\sqrt{1-\varepsilon_a}}{1-\varepsilon_a} \tag{2-3}$$

where

ε_a = vertical strain

M = modulus of geocell material

D_0 = diameter of the cell.

Chang et al. (2007 and 2008) tested geocell-reinforced sandy soil under both static and dynamic plate loading. Results from the study showed a 140% increase in road strucutre bearing capacity and reduction in settlement. Geocells of higher height performed better than those with

smaller height. Friction resistance between geocells and infill materials and tensile strength of the geocell material were found to significantly affect the performance of geocell sections.

Han et al. (2008b and 2010), Pokharel et al. (2009a, 2009b, 2009c, 2010, and 2011a), Pokharel (2010), and Yang (2010) conducted static and dynamic plate loading tests on geocell-reinforced base layers. Similar to previous studies, results showed that bearing capacity could be improved up to 2.5 times the capacity for unreinforced sections and that geocell welds were a failure point in geocells. Geocell–reinforced cohesionless sand showed better performance in static loading than geocell-reinforced quarry waste with apparent cohesion. Permanent deformation was reduced in geocell-reinforced sections, vertical stresses were reduced on the subgrade, and the stress distribution angle was increased. Infill stiffness was maximized only after the geocell was deformed up to a certain point.

2.2.1.3 Field Tests

Field testing of geocell-reinforced layers consisted of using geocells to reinforce larger areas than box test areas in the laboratory and application of full-scale loads. In this literature review, APT of geocell-reinforced layers is considered to be part of the field tests.

Webster and Watkins (1977) used plastic tube assemblies as geocellular reinforcement in access roads over soft subgrades. The initial study was followed by an investigation of aluminum geocells by Webster and Alford (1978). Initial tests indicated that geocells reduced surface permanent deformation, suitable for wet weather base course construction, and reduced design thickness up to 40%. Webster (1979a and 1979b) showed that as geocells were reduced in height the quality of infill had to be improved and a deep in-fill cover was necessary to achieve improved road structure performance in terms of resisting traffic repetitions. In that study, square and hexagonal geocells outperformed rectangular geocells. However, benefits of geocells decreased with increased width of the geocell openings.

Road embankments with geocell-reinforced foundations over soft clay were studied by Cowland and Wong (1993). Road embankments performed well, and investigators concluded that the geocell-reinforced foundation performed as well as the plastic-reinforced rockfill rafts. Edil et al. (2002) investigated various types of geosynthetics and by-products as infills; infill materials in the geocell consisted of foundry slag. The geocell-reinforced layer met the performance requirements set in the study.

Pokharel (2010), Yang (2010), Han et al. (2011), and Pokharel et al. (2011) performed accelerated pavement testing (APT) of unpaved road sections using geocellular reinforcement and quarry waste (QW), RAP, and crushed limestone (AB-3) as infill materials. The studies showed that geocells are useful on unpaved road sections. Stability of the road sections improved and permanent deformations reduced in the geocell-reinforced sections. Stability was based on thickness of the reinforced base layer; base layer thickness reduction and extension of the life of the section were observed with all types of infill material. In addition, all infill materials increased the stress distribution angle. Although tall geocells showed better performance, compaction of infill materials in tall geocells was difficult but critical to the success of reinforced sections. Results showed that infill material can be of reduced quality and still perform as well as high quality materials. Geocells are a sustainable alternative when byproducts (QW) and recycled products (RAP) are used as infill materials. However, adequate cover over the geocells is necessary in order to minimize geocell damage during compaction.

2.2.1.4 Summary of Test Results

Geocell-reinforced base layers have shown to outperform unreinforced layers of the same thickness. Geocells increase bearing capacity and reduce permanent deformation of the surface. Infill quality dictates ultimate bearing capacity of the layer; however, low quality infill materials can meet performance specifications. Quality control of geocell weld seams and increased tensile strength of the geocell are needed in order to limit premature failures. Compaction of infill material inside geocells is critical in order to achieve the total benefits of reinforcement.

2.2.3 Reinforcement Mechanisms

Giroud and Noiray (1981) identified lateral confinement, increased bearing capacity, and membrane-under-tension effect as major reinforcement mechanisms for geotextile reinforcement. These mechanisms are described in details here.

2.2.3.1 Confinement Effect

Lateral and vertical confinement is produced when infill material is reinforced with geocells. The 3-D structure of the geocell provides lateral confinement of infills. Lateral spreading is reduced under repeated loading (Gourves et al. 1996). Friction between the infill material and geocell wall provides vertical confinement, and the geocell-reinforced base acts as a

mattress. Mhasiskar (1992) suggested that geocells with higher modulus and less extensibility are desired since hoop stresses in the geocell wall significantly impact geocells' resisting loading. Gourves et al. (1996) used compression tests and FE analysis to explain the confinement effect. Han et al. (2008a and 2008b) showed that geocells provide confinement to infill material, potentially increasing the bearing capacity and elastic modulus of the infill.

2.2.3.2 Beam (Tension) Effect

Tension produced in the curved geocell-reinforced mattress to resist the vertical load has been referred to as the membrane under tension, or beam effect (Rajagopal et al. 1999, Dash et al. 2004, and Zhou and Wen 2008). Giroud and Han (2004a) described how the reinforced layer must deform significantly before the beam effect is mobilized.

2.2.3.3 Stress Distribution

Since the study by Webster and Alford (1978), all research involving geocell have shown that geocell-reinforced layers can demonstrate increased bearing capacity, even with reduced thickness of geocell-reinforced layers as compared to the unreinforced layers. Geocells spread load over a wide area, thereby providing increased load-carrying capacity (Mhaiskar and Mandal 1992a and 1992b and Dash et al. 2004). Stress reduction at the interface between the reinforced layer and subgrade and the increase in bearing capacity result from wider stress distribution.

2.2.3.4 Summary of Reinforcement Mechanisms

Geocells provide reinforcement via three distinct mechanisms: confinement effect, beam effect, and stress distribution. Each mechanism results in increased bearing capacity, reduced stress on the subgrade, and reduced permanent deformation. A combination of mechanisms could be why geocell reinforcement works.

2.2.4 Influence Factors

Researchers have studied the effects of geocell features in order to design the most efficient system. Geocell dimension, geocell material stiffness, infill material and cover thickness, and subgrade strength and thickness have been shown to influence performance of the geocell-reinforced base layer.

2.2.4.1 Effect of Geocell Dimension

Various ratios of geocell dimensions have been determined for specific applications. Geocell height is defined as the thickness or depth of the geocell, and geocell width is the opening size of the geocell and width of the loading area of a plate. Optimum dimension ratios obtained in past studies are summarized in Table 2-1. Although tall geocells seem to perform better in terms of structural capacity, compaction of infill material becomes more difficult (Pokharel 2010).

Table 2-1 Optimum dimensions of geocell structures (after Yuu et al. 2008)

Study	*Geocell height/ Geocell width*	*Plate width/ Geocell width*	*Geocell height/ Plate width*
Rea and Mitchell (1978)	1.59	1.05 to 1.41	*
Mitchell et al. (1979)	1.42 to 2.13	1.42	*
Dash et al. (2001a)	1.67	0.84 to 1.15	2.0

2.2.4.2 Effect of Stiffness of Geocell Material

Stiff geocell material showed improvement in performance of reinforced infill (Bathurst and Jarrett 1988, Shimizu and Inui 1990, Chang et al. 2007 and 2008, and Pokharel et al. 2010). Mhaiskar and Mandal (1996) showed that the elastic modulus of geocell materials affects the performance of the geocell-reinforced layer more than the seam strength at given dimension ratios.

2.2.4.3 Effect of Infill Material and Cover Thickness

Although high quality materials have been shown to result in better performance (Kazerani and Jamnejad 1987), geocell-reinforced sections with low quality materials meet specified performance requirements (Edil et al. 2002, Han et al. 2008a, 2008b and 2010, Pokharel et al. 2009a, 2009b, 2009c, 2010, and 2011a, Pokharel 2010, and Yang 2010). Infill material when compacted performs better (Mhaiskar and Mandal 1996 and Dash et al. 2001a). Sekine et al. (1994) showed that achieving compaction in geocell-reinforced sections requires more compactive effort than that for the unreinforced layer. Cover over the geocell-reinforced layer was shown to have little effect on bearing capacity of the layer; however, cover was shown

to protect geocells during compaction of infill and application of loading (Mitchell et al. 1979 and Pokharel 2010).

2.2.4.4 Effect of Subgrade Strength

High subgrade stiffness results in high ultimate bearing capacity of the reinforced layer (Rea and Mitchell 1978, Shimizu and Inui 1990). A majority of testing has been conducted on geocell-reinforced layers over soft and/or wet subgrades, with results indicating that geocell-reinforced layers outperform unreinforced layers compared to soft subgrade, and geocell-reinforced layers meet performance requirements (Sekine et al. 1994).

2.2.4.5 Possible Effects of Hot-Mix Asphalt Layer

Control of vertical stress on top of the subgrade is critical for a better performing pavement. HMA sections reduce the vertical stress applied to the subgrade (Huang 2004). Therefore, the geocell-reinforced section would not require as high a bearing capacity if the HMA layer was present.

2.2.5 Design Methods

2.2.5.1 Giroud and Han Equation

Giroud and Han (2004a and 2004b) developed a theoretical equation for the thickness of base layer with incorporation of planar geogrid–reinforced unpaved roads, as shown in Equation (2-4) and simplified to Equation (2-5). Han et al. (2008a) suggested a modulus improvement factor to account for slowing of the rate of deterioration of base quality.

$$h = \frac{1 + k * logN}{tan\alpha_0[1 + 0.204 * (R_E - 1)} * \left(\sqrt{\frac{P}{\pi r^2 \left(\frac{s}{f_s}\right) * \{1 - \xi \exp[-\omega \left(\frac{r}{h}\right)^n]\} N_c c_u}} - 1 \right) r \quad (2\text{-}4)$$

where

r = radius of tire contact area (m)

N = number of passes

P = wheel load (kN)

c_u = undrained cohesion of the subgrade soil (kPa), = f_c*CBR_{sg}

f_c = factor determined by CBR testing and unconfined compression test

N_c = bearing capacity factor, assumed to be 5.14 for geocell-reinforced unpaved roads (Giroud and Han 2004b)

R_E = modulus ratio of base course to subgrade reaction:

$$R_E = I_f \frac{E_{bc}}{E_{sg}} = Max\left\{7.6, I_f\left(\frac{3.48CBR_{bc}^{0.3}}{CBR_{sg}}\right)\right\} \quad (2\text{-}5)$$

E_{bc} = resilient modulus of base course (MPa)

E_{sg} = resilient modulus of subgrade soil (MPa)

CBR_{bc} = California Bearing Ratio (CBR) of base course

CBR_{sg} = CBR of subgrade

α_0 = reference stress distribution angle (degrees)

k = constant depending on base course thickness and reinforcement

s = allowable rut depth (mm)

f_s = factor equal to 75 mm

ξ, ω, n are constants.

$$I_f = \left(\frac{E_{bc\,(reinfroced)}}{E_{bc(unreinforced)}}\right) \quad (2\text{-}6)$$

$$h = \frac{1.26 + (0.96 - 1.46 * J^2)\left(\frac{r}{h}\right)\log N}{f_E} * \left(\sqrt{\frac{P}{\pi r^2 m N_c c_u}} - 1\right) r \quad (2\text{-}7)$$

where

J = aperture stability modulus of geogrid (N-m)

f_E = modulus ratio factor

m = bearing capacity mobilization factor (Giroud and Han 2004b), shown in Equation (2-8).

$$m = \left(\frac{s}{f_s}\right)\left\{1 - 0.9exp\left[-\left(\frac{r}{h}\right)^2\right]\right\} \quad (2\text{-}8)$$

Based on the calibration of factors by Hammit (1970) and Gabr (2001), Giroud and Han (2004b) inserted calibrated values, resulting in Equation (2-9).

$$h = \frac{0.868 + (0.661 - 1.006J^2)\left(\frac{r}{h}\right)^{1.5} \log N}{\{1 + 0.204 * (R_E - 1)\}} * \left(\sqrt{\frac{P}{\pi r^2 * m * N_c * c_u}} - 1\right) r \quad (2\text{-}9)$$

where

$E_{bc(reinforced)}$ = the modulus of the reinforced base

$E_{bc(unreinforced)}$ = the modulus of the unreinforced base.

Pokharel (2010) suggested a k' factor to replace the term $(0.661 - 1.066J^2)\left(\frac{r}{h}\right)^{1.5}$ in Equation 2-7. The k' factor was calibrated using test data from geocell-reinforced base layers over weak subgrade. The k' factor for the same type of (nano-composite alloy of polyester/polyamide nano fibers, dispersed in polyethylene matrix, NPA) geocell used in this study was found to be $k' = 0.52\left(\frac{r}{h}\right)^{1.5}$. The resulting design equation for NPA geocells is shown in Equation (2-10).

$$h = \frac{0.868 + 0.52\left(\frac{r}{h}\right)^{1.5} \log N}{\{1 + 0.204 * (R_E - 1)\}} * \left(\sqrt{\frac{P}{\pi r^2 m * N_c * c_u}} - 1\right) r \quad (2\text{-}10)$$

where the variables have been explained before.

2.2.5.2 Mechanistic-Empirical Design Guide

The AASHTO has developed a Mechanistic-Empirical Design Guide (MEPDG) to design roads through applications of mechanistic principles. MEPDG contains three basic elements: 1) theory to predict critical pavement responses as a function of traffic and climatic loading (mechanistic); 2) material characterization; and 3) "Defined relationships between the critical pavement response parameter and field-observed distress (empirical)" (AASHTO 2008). Results

of the design guide include predicted distresses and smoothness at a certain reliability level. The process is iterative in order to assess trial designs.

For characterization and design of unbound base materials in MEPDG, two models are used: response model and permanent deformation model, or damage model. The resilient modulus, M_r, and Poisson's ratio, ν, are used to estimate the resilient response of pavement layers in the response model, while an empirical correlation is available between the permanent strain, ε_p, and the resilient strain, ε_r, with the number of wheel passes, N. MEPDG uses Equation (2-11) to estimate the resilient modulus, M_r, of granular and soil materials (AASHTO 2008).

$$M_r = k_1 p_a \left(\frac{\theta}{P_a}\right)^{k_2} \left(\frac{\tau_{oct}}{P_a} + 1\right)^{k_3} \quad (2\text{-}11)$$

where

M_r = resilient modulus

θ = bulk stress, $\sigma_1 + \sigma_2 + \sigma_3$:

σ_1 = major principal stress

σ_2 = intermediate principal stress

σ_3 = minor principal stress, confining pressure

τ_{oct}= octahedral shear stress, $= \frac{1}{3} * \sqrt{(\sigma_1-\sigma_2)^2+(\sigma_1-\sigma_3)^2+(\sigma_2-\sigma_3)^2}$

P_a = normalizing stress

k_1,k_2,k_3 = regression constants

p_a = atmospheric pressure.

Tangent modulus is used instead of secant modulus in FE analysis. Tangent resilient modulus, E_t, shown in Equation (2-12), is derived from Equation (2-11) because the maximum stress state can be rewritten as $\sigma_1 > \sigma_2 = \sigma_3$ (NCHRP 2011 and Perkins 2004).

$$E_t = \frac{M_r}{1 - (\sigma_1 - \sigma_3) * \left(\frac{k_2}{\theta} + \frac{\sqrt{2} * k_3}{3(\tau_{oct} + p_a)}\right)} \quad (2\text{-}12)$$

Where the variables have been defined earlier.

MEPDG calculates incremental permanent deformation or rutting within each sublayer. Deformation is calculated each subseason at mid-depth of each sublayer in the structure. Plastic

vertical strain under specific conditions is calculated for a number of axle-load repetitions. The "strain hardening" approach is used to accumulate plastic vertical strains within each subsection in a cumulative deformation subsystem (AASHTO 2008). MEPDG uses Equation (2-13) in order to determine permanent deformation in the unbound layers.

$$\Delta_{p(soil)} = \beta_{s1} k_{s1} \varepsilon_v h_{soil} \left(\frac{\varepsilon_0}{\varepsilon_r}\right) e^{-\left(\frac{\rho}{n}\right)^{\beta}} \quad (2\text{-}13)$$

where

$\Delta_{p(soil)}$ = permanent or plastic deformation for the layer/sublayer, in.

n = number of axle-load applications

ε_0= intercept determined from laboratory repeated laod permanent deformation tests, in./in.

ε_r= resilient strain imposed in laboratory test to obtain material properties ε_0, ε, and ρ, in./in.

ε_v= average vertical resilient or elastic strain in the layer/sublayer and calculated by the structural response model, in./in.

h_{soil} = thickness of the unbound layer/sublayer, in.

k_{s1} = global calibration coefficients, 1.673 for granular materials and 1.35 for fine-grained materials

ε_{s1}= local calibration constant for rutting in unbound layers

$Log\ \beta = -0.61119 - 0.017638(W_c)$;

W_c = Water Content,% .

$$\rho = 10^9 \left(\frac{-4.89285}{(1-(10^9)^{\beta})}\right)^{\frac{1}{\beta}}$$

Deformation of the HMA layer (rut depth) is found using Equation (2-14).

$$\Delta_{\rho(HMA)} = \varepsilon_{p(HMA)} h_{HMA} = \beta_{1r} k_z \varepsilon_{r(HMA)} 10^{k_{1r}} n^{k_{2r}\beta_{2r}} T^{k_{3r}\beta_{3r}} \quad (2\text{-}14)$$

where

$\Delta_{\rho(HMA)}$ =accumulated permanent or plastic vertical deformation in the HMA layer/sublayer, in.

$\varepsilon_{p(HMA)}$= accumulated permanent or plastic axial strain in the HMA layer/sublayer, in/in

h_{HMA} = thickness of the HMA layer/sublayer, in.

$\varepsilon_{r(HMA)}$ = resilient or elastic strain calculated by the structural response model at the mid-depth of each HMA sublayer, in./in.

n = number of axle-load repetitions

T = mix or pavement temperature, °F

k_z = depth of confinement factor

$k_{1r,2r,3r}$ = global field calibration parameters, k_{1r} = -3.35412, k_{2r} = 0.4791, k_{3r} = 1.5606

β_{1r}, β_{2r}, β_{3r} = local or mixture field calibration constants.

$k_z = (C_1+C_2D)*0.328196^D$

$C_1 = -0.1039(H_{HMA})^2+2.4868H_{HMA}-17.342$

$C_2 = 0.0172(H_{HMA})^2-1.7331H_{HMA}+27.428$

where

D = depth below the surface, in.

H_{HMA} = total HMA thickness, in.

2.3 Modeling

2.3.1 Subgrade Layer Modeling

Modeling of soil behavior in the subgrade layer is very complicated due to variables such as soil type, density, and water content. Constitutive models are mathematical approximations of stress-strain behavior of a material. Due to the complicated nature of soil, constitutive models have been developed to focus on certain characteristics of a given soil.

2.3.1.1 Linear Elastic Modeling

Linear elastic modeling determines stress-strain relationships based on two of the four material properties, which include Young's modulus E, Poisson's ratio v, bulk modulus K, and shear modulus, G. A generalized Hooke's Law can be used to define the stress-strain relationship of an isotropic, linear elastic model, as expressed in Equation (2-15) through Equation (2-20). Linear elasticity simulates recoverable deformation of soil in response to external forces.

$$\varepsilon_{11} = \frac{1}{E}[\sigma_{11} - v(\sigma_{22} + \sigma_{33})] \quad (2\text{-}15)$$

$$\varepsilon_{22} = \frac{1}{E}[\sigma_{22} - v(\sigma_{11} + \sigma_{33})] \quad (2\text{-}16)$$

$$\varepsilon_{33} = \frac{1}{E}[\sigma_{33} - v(\sigma_{11} + \sigma_{22})] \quad (2\text{-}17)$$

$$\epsilon_{12} = \frac{\sigma_{12}}{2G} \quad (2\text{-}18)$$

$$\epsilon_{13} = \frac{\sigma_{13}}{2G} \quad (2\text{-}19)$$

$$\epsilon_{23} = \frac{\sigma_{23}}{2G} \quad (2\text{-}20)$$

2.3.1.2 Elastoplastic modeling

Elastoplastic models use specific yield criteria, hardening/softening laws, and flow rules.

2.3.1.2.1 Mohr-Coulomb Model

Mohr-Coulomb is a simple elastoplastic model commonly used for linearly elastic, perfectly plastic modeling. A yield criterion and non-associated flow rule for shear failure are used in this model. A simple form of the Mohr-Coulomb yield criterion is shown in Equation (2-21). Mohr-Coulomb assumes that elastic properties of the soil are constants. Shear strength can be modeled accurately; however, soil shear strength is stress-dependent, requiring a nonlinear model.

$$\tau = c + \sigma tan\emptyset \quad (2\text{-}21)$$

where

τ = shear stress

σ = normal stress on the plain which slip is initiated

c = cohesion

$\emptyset$ = internal friction angle of the soil.

2.1.1.2.2 Duncan-Chang Model

Mohr-Coulomb equations were modified by Duncan et al. (1980) to account for stress dependency of soil. The resulting equations are known as the simple, effective Duncan-Chang model. However, this model has limitations, as stated by Duncan et al. (1980):

1. The intermediate principal stress σ_2 will be ignored in a 3-D problem.
2. Results may be unreliable in extensive failures.
3. Volume changes due to changes in shear stress are not considered.

4. Model is intended for quasi-static analysis.

Konder (1963) suggested use of a hyperbolic equation to fit the triaxial stress-strain curves of soil, as shown in Equation (2-22). Janbu (1963) related E_i and σ_3 in Equation (2-23). According to Equation 2-23, E_i increases with σ_3; however, σ_3 can only be positive, unlike a soil element that can experience tensile stress in a numerical model. A very small confining stress is used to avoid errors in computation if $\sigma_3 \leq 0$.

$$(\sigma_1 - \sigma_3) = \frac{\varepsilon_1}{\frac{1}{E_i} + \frac{\varepsilon_1}{(\sigma_1 - \sigma_3)_{ult}}} \tag{2-22}$$

where

E_i = initial tangent modulus

$(\sigma_1-\sigma_3)_{ult}$ = asymptotics value of the deviatoric stress

ε_1 = axial strain.

$$E_i = K p_a (\frac{\sigma_3}{p_a})^n \tag{2-23}$$

where

K = modulus number

n = modulus exponent

p_a = atmospheric pressure.

K and n are dimensionless parameters determined by a series of triaxial tests under varying confining stress σ_3. The term $(\sigma_1-\sigma_3)_{ult}$ can be related to the triaxial compressive strength $(\sigma_1-\sigma_3)_f$ using Equation (2-24), and $(\sigma_1-\sigma_3)_f$ is calculated based on Mohr-Coulomb's yield criterion, shown in Equation (2-25).

$$(\sigma_1 - \sigma_3)_f = R_f (\sigma_1 - \sigma_3)_{ult} \tag{2-24}$$

where

R_f = failure ratio determined by a series of triaxial tests.

$$(\sigma_1 - \sigma_3)_f = \frac{2c \cos \emptyset + 2\sigma_3 \sin\emptyset}{1 - \sin\emptyset} \tag{2-25}$$

Where the variables have been explained earlier.

The tangent Young's modulus E_t can be found from Equation (2-26) by substituting Equations (2-24), (2-2) and (2-3) into Equation (2-23) and then differentiating Equation (2-23) with respect to axial strain ε_1, shown in Equation (2-26) (Duncan et al. 1980).

$$E_t = \left[1 - \frac{R_f(1 - sin\emptyset)(\sigma_1 - \sigma_3)}{2c\ cos\emptyset + 2\sigma_3 sin\emptyset}\right]^2 Kp_a\left(\frac{\sigma_3}{p_a}\right)^n \tag{2-26}$$

Where the variables have been explained earlier.

Bulk modulus *B*, Equation (2-27), and stress dependency of friction angle, Equation (2-28), are two elastic properties Duncan et al. (1980) suggested be determined. Equations (2-26), (2-27), and (2-28) are known as the Duncan-Chang Model.

$$B = K_b p_a\left(\frac{\sigma_3}{p_a}\right)^m \tag{2-27}$$

where

K_b = dimensionless bulk modulus number

m = dimensionless bulk modulus exponent.

$$\emptyset = \emptyset_0 - \Delta\emptyset log_{10}\left(\frac{\sigma_3}{p_a}\right) \tag{2-28}$$

where

$\emptyset_0$ = friction angle when σ_3 = 1 atmosphere

$\Delta\emptyset_0$ = reduction of friction angle for every 10 times increase in σ_3.

Boscardin et al. (1990) proposed Equation (2-29) instead of Equation (2-26) to calculate the tangent bulk modulus B_t because the bulk modulus in *B* is the secant modulus. In order to overcome limitations of the model, Rodriguez-Roa (2000) suggested substituting all $\frac{\sigma_3}{p_a}$ in the Duncan-Chang equations with $\frac{\sigma_2+\sigma_3}{2p_a}$.

$$B_t = B_i\left(1 + \frac{\sigma_m}{B_i\varepsilon_u}\right)^2 \tag{2-29}$$

where

B_i = initial bulk modulus when σ_3 = 1 atmosphere

ε_u = asymptotic value of the volumetric strain

σ_m = mean effective stress ($\sigma_m = \frac{\sigma_1+\sigma_2+\sigma_3}{3}$).

2.3.1.3 Shakedown Theory

Sharp and Booker (1984) introduced the shakedown theory for pavement. Collins et al. (1993) described four types of long-term responses: purely elastic, elastic shakedown, plastic shakedown, and ratcheting (or incremental) collapse. According to the shakedown theory, maximum cyclic stress in layers that exceed the plastic shakedown limit is to be avoided. However, shakedown limits are difficult to estimate, so the use of upper and lower bound theorem has been suggested to estimate shakedown limits (Collins et al. 1993, and Collins and Boulbibane 2000). Werkmeister et al. (2003) suggested using Equation (2-30) to estimate the critical stress condition at the shakedown limit. However, the simplified equation is not widely accepted; even Werkmeister et al. (2003) suggested using alternative means to verify predicted values.

$$\sigma_{1\,max} = \alpha\left(\frac{\sigma_{1\,max}}{\sigma_c}\right)^{\beta} \tag{2-30}$$

where

$\sigma_{1\,max}$ = peak axial stress

σ_c = confining pressure

α,β = material parameters determined by a series of cyclic triaxial tests.

2.4 Finite Element Modeling

Finite element modeling (FEM) is a numerical method that provides approximations of solutions to initial boundary value problems. The basic concept of FEM involves dividing a complicated geometry into smaller elements for which differential equations can be solved to approximate behavior of the element and geometry. FEM consists of three phases: preprocessing phase, solution phase, and postprocessing phase. Moaveni (1999) described each phase in the following manner:

Preprocessing Phase: In the preprocessing phase, the user must create and discretize the domain into finite elements. The user must define a shape function to represent the physical behavior of the elements, and equations must be developed for the elements. Then the global

stiffness matrix must be developed after the elements are arranged into an assembly. The loading, boundary, and initial conditions also must be defined.

Solution Phase: In the solution phase, a set of linear and nonlinear algebraic equations are solved simultaneously in order to obtain nodal results. These results refer to displacements, temperature, stresses, or other desired outputs.

Postprocessing Phase: In the postprocessing phase, the user is able to obtain and manipulate outputs at desired locations.

Abaqus was the chosen software package for this study because of its availability at KSU and ability to handle nonlinear layer properties. The Abaqus/CAE is used to create, edit, monitor, diagnose, analyze, and visualize results from Abaqus/Standard and Abaqus/Explicit (Abaqus 2011).

2.4.1 Finite Element Modeling of HMA

HMA behavior is unique because it varies depending on service temperature or loading rate. At low temperatures and/or fast loading rates, HMA behaves in an elastic/linear viscoelastic manner; at high temperatures and/or slow loading rates, it behaves in a nonlinear viscoelastic and viscoplastic/plastic manner. Various mechanistic models developed for HMA have struggled for acceptance due to the difficulty of obtaining elastoplastic or viscoplastic properties of HMA materials (Onyango 2009). Abaqus has built-in models for creep, Drucker-Prager, and visco-elastoplastic behavior. The following sections discuss each of these models.

2.4.1.1 Creep Model

Creep is a time-dependent material, and the rate of creep in HMA is accelerated by increased stress or temperature. Primary, secondary, and tertiary are the three stages of this creep. “In the primary stage, the strain rate decreases with loading time. In the secondary zone, the strain rate becomes constant with loading time before its starts increasing rapidly (NCAT 2009).” When creep reaches the tertiary stage, creep rate increases to the point of fracture or failure. The tertiary stage is difficult to model due to failure. The first two stages can be modeled using the Bailey-Norton Law (Kraus 1980). Equation (2-31) assumes that creep in the material is solely dependent on the current stress state. Strain rate is obtained by differentiating Equation (2-32) (Onyango 2009 and Wu 2001).

$$\varepsilon^c = \frac{A}{m+1}\sigma^n t^{m+1} \quad (2\text{-}31)$$

where

A, *m*, *n* = user-defined functions of temperature

σ = uniaxial equivalent deviatoric stress

t = total time.

$$\dot{\varepsilon_{cr}} = A\sigma^n t^m \quad (2\text{-}32)$$

where

$\dot{\varepsilon}_{cr}$= creep strain rate.

Creep model in Abaqus can use either time hardening or strain hardening behavior. In time hardening, the stress state remains constant. Strain hardening is used when stress varies throughout the analysis. Five material properties define the creep model- creep parameters (A, m, & n) ; elastic parameters: elastic modulus (*E*); and Poissons's ratio (*v*).

Huang (2001), Sivasubramaniam (2005), and Onyango (2009) performed Abaqus modeling of rut depths in HMA structures. The modeling results were encouraging in some of the HMA sections. However, some properties, such as modified binders and initial densities, created inaccurate results for rut depth prediction (Sivasubramaniam 2005). Huang (2001) and Onyango (2009) included wheel wander into rut depth prediction, achieving reasonably accurate prediction.

2.4.1.2 Drucker-Prager Model

In Abaqus, an elastoplastic model can be implemented using the extended Drucker-Prager model to model materials with friction that exhibit pressure-dependent yield. The model can also be used to model materials with compressive yield strength greater than tensile yield strength. Yield surface, linear form, hyperbolic form, or a general exponent form in the meridional plane is the basis of yield criteria. The linear yield Drucker-Prager model is expressed in Equations (2-33) and (2-34) (Abaqus 2010). HMA material parameters for the Drucker-Prager model are obtained by a uniaxial compressive strength test and a triaxial compression test.

$$F = t - p * tan\beta - d = 0 \quad (2\text{-}33)$$

$$t = \frac{q}{2}\left[1 + \frac{1}{K} - \left(1 - \frac{1}{K}\right) * \left(\frac{r}{q}\right)^3\right] \quad (2\text{-}34)$$

where

p = equivalent pressure stress

β = friction angle

d = cohesion of the material:

$d = \left(1 - \frac{1}{3} tan\beta\right)\sigma_c$ if hardening is defined by uniaxial compression stress, σ_c

$d = \left(\frac{1}{K} + \frac{1}{3}\tan\beta\right)\sigma_t$, if hardening is defined by uniaxial tension yield stress, σ_t

$d = \frac{\sqrt{3}}{2} r \left(1 + \frac{1}{K}\right)$, if the hardening is defined by the cohesion

q = von mises equivalent stress

r = third invariant of deviator stress

K = ratio of yield stress in triaxial tension to the yield stress in triaxial compression, $0.778 \leq K \leq 1$.

Huang (2000) used the Drucker-Prager model to successfully model the base material and subgrade in HMA FEM. Onyango (2009) attempted to use the Drucker-Prager model to model the HMA layer, but results were not accurate, demonstrating overprediction up to 2,590% and asymmetrical profile results. The Drucker-Prager model is more suitable for granular materials or HMA at high temperatures (>60 °C) (Onyango 2009). Park (2004) also suggested that the model cannot predict tertiary deformation without damage parameters.

2.4.1.3 Visco-Elasto-Plastic Model

Zhao (2002) combined a viscoplastic model and a viscoelastic model to individually model elastic, plastic, viscoelastic, and viscoplastic strain components and integrate them into the final model. The viscoelastic model is based on Schapery's (1990) potential theory, while the viscoplastic model is based on work done by Uzan et al. (1985) on a strain-hardening model. The resulting Zhao formulation is shown in Equation 2-35.

$$\varepsilon_{vp} = E_R \int_0^{\xi} D(\xi - \xi') \frac{d\left(\frac{\sigma}{C(S^*)}\right)}{d\xi'} d\xi' + \left(\frac{p+1}{D}\right)^{\frac{1}{p+1}} \left(\int_0^{\xi} \sigma^q d\xi\right)^{\frac{1}{p+1}} \quad (2\text{-}35)$$

This model requires stress (σ), reduced time (ξ), and calibrated material parameters in order to be solved. Zhao showed that model results were accurate up to the peaks of the stress-strain curves. The viscoelastic model is based on the continuum damage theory that was discussed as the reasoning of error in the post-peak region. The model was calibrated with uniaxial stress state data, meaning that the confinement effect was not taken into account.

2.4.2 Geocell Modeling

Geocells that support embankment loads (Evan 1994, Madhavi Latha and Rajagopal 2007) or geocells that support footings have been numerically modeled (Mhaiskar and Mandal 1996, Han et al. 2008b, Madhavi et al. 2008 and 2009, Madhavi Latha and Somwanshi 2009). Evan (1994), Han et al. (2008b), and Yang (2010) modeled reinforcement separately from the infill material. Evan (1994) modeled planar reinforcement using a two-dimensional (2-D) Duncan-Chang model, while Han et al. (2008b) modeled the 3-D structure of the geocell separately from the infill. Han et al. (2008b) used a Mohr-Coulomb model for the infill material, which returned inaccurate results because Mohr-Coulomb models ignore stress-dependency of the soil.

Yang (2010) built models of geocellular confinement systems using a commercially-available FE software, Fast Lagrangian Analysis of Continua ($FLAC^{3D}$). For static loading test, a Duncan-Chang model was used to model the infill material, and linear elastic plate elements were used to model the geocells. A Mohr-Coulomb yield criterion was used to model the stress-strain relationship between the geocell and the infill soil. Yang successfully modeled the geocells and infill separately.

In this study, the mechanistic-empirical model was used for the numerical model of the APT sections. However, the mechanistic-empirical model was designed for an axisymmetric model that does not take into account 3-D geometry of the geocells. Therefore, the tangent resilient modulus had to be re-derived to account for the intermediate principal stress σ_2. Initial stress increase due to initial compaction effort and residual stress accumulated in the soil due to the presence of geosynthetics were also considered. Diamond-shaped pockets were used to model the geocells. One quarter of the test sections was modeled to accelerate the calculations. The load was applied in small time steps to allow for formulation of the tangent resilient modulus.

The permanent deformation was calculated using Equation (2-36).

$$PD = k\varepsilon_v h_{soil}\left(\frac{\varepsilon_0}{\varepsilon_r}\right) * e^{-\left(\frac{\rho}{N}\right)^{\beta}} \quad (2\text{-}36)$$

where

PD = permanent deformation

ε_v= average vertical resilient strain along the centerline of the model in this layer

h_{soil} = thickness of the soil layer

ρ,β, $\left(\frac{\varepsilon_0}{\varepsilon_r}\right)$ = material parameters obtained from the cyclic triaxial tests

N = number of axle load repetitions.

2.4.3 Summary of Modeling

Multiple models had to be combined in this study in order to develop an accurate modeling approach. The Drucker-Prager model accurately models granular materials, but it tends to give inaccurate results when modeling HMA. The geocells have only been modeled in previous studies a few times. Linear elastic plate elements used by Yang (2010) were found to be the most accurate approach to model geocells.

2.5 Full-Scale Accelerated Pavement Testing

Hugo and Martin (2004) described APT as "the controlled application of wheel loading to pavement structures for the purpose of simulating the effects of long in-service loading conditions in a compressed time period." APT allows new design and analysis techniques to be related to actual performance under full-scale testing (Willis 2008). In 2004, 48 APT facilities were in existence worldwide, with 28 of those facilities classified as active (Hugo and Martin 2004). Full-scale APT facilities can be classified as full scale test roads/tracks or load simulation devices.

2.5.1 Test Roads/Tracks

Test roads are full-scale, full-size experimental pavement sections subjected to actual traffic loading (Coetzee et al. 2000). Test roads involve building of a full-scale pavement and use of a full-scale vehicle to load the sections. Various aspects of pavements have been studied on test roads since 1920's. Bates Road test studied the effect of solid rubber tires on road pavements in the early 1920s (NCAT 2011). In 1941 the Highway Research Board started studying relative

effects of four loadings on a particular concrete pavement. In the early 1950s, the Western Association of State Highway Officials (WASHO) conducted similar tests on flexible pavements (Huang 2004). In the late 1950s, the American Association of State Highway Officials (AASHO) began to conduct road tests in which "the objective of the project was to determine any significant relationship between the number of repetitions of specified axle loads of different magnitudes and arrangements and the performance of different thicknesses of flexible and rigid pavements" (Huang 2004). Results from the AASHO Road test are the basis of the AASHTO Pavement Design Guide currently in use. The Pennsylvania Transportation Institute conducted a road test in the 1970s as a satellite to the AASHO Road test (Metcalf 1996).

In 1993, the Federal Highway Administration (FHWA) funded the construction of a test road facility, WesTrack, in Nevada. Objectives of the tests were:

"*1. To continue the development of performance-related specifications (PRS) for hot-mix asphalt construction by evaluating the impact on performance of deviations in materials and construction properties (e.g., asphalt content, air void content, and aggregate gradation) from design values in a large-scale, accelerated field test, and*

2. To provide early field verification of the Strategic Highway Research Program (SHRP) Superior Performing Pavement (SUPERPAVE) Level III mix design procedures" (WesTrack 2011).

The Minnesota Department of Transportation (MnDOT) built the MnROAD test road in 1994, a portion of which currently comprises part of the Interstate 94 roadway. MnRoad test program also has a low-volume road portion. The I-94 section utilizes traffic control to divert traffic from the test sections in order to allow pavement construction and pavement testing in absence of traffic. The test road has allowed researchers to evaluate pavement performance, examine factors affecting pavement performance, and develop tools and methods to improve design, construction, and maintenance (MnROAD 2011).

The National Center for Asphalt Technology (NCAT) was established in 1986 in order to investigate technical issues related to asphalt pavement. In 2000, NCAT constructed a 1.7-mile oval to be used as a test track, shown in Figure 2-3. The objective of the test track was to reduce the life cycle cost of flexible pavements. The test data allowed for performance comparison of laboratory test results and field performance. Numerous pavement studies incorporating different pavement design features and materials have been conducted since 2000 (Pavetrack 2011).

Figure 2-3 NCAT Test Track (Pavetrack 2011)

2.5.2 Load Simulation Devices

As early as 1912, simulation devices were used to apply loading to pavements. The United Kingdom Transportation Research Laboratory had built many versions of their "Road Machine" to test pavements. Various load simulation setups have been constructed by road authority agencies over the past 100 years. Heavy vehicle simulators (HVS), shown in Figure 2-4, were first used to simulate traffic loading in the 1960s in South Africa. A circular test track was built in France with a four-arm rotating loading system to test pavement structures as shown in Figure 2-5. Kansas State University has built a load frame with a belt-driven axle bogie, as shown in Figure 2-6. Majority of APT testing devices are assorted versions or setups of the HVS, circular track, or load frame devices (HVS 2011).

Figure 2-4 U.S. Army Corp of Engineers HVS (USACE 2011)

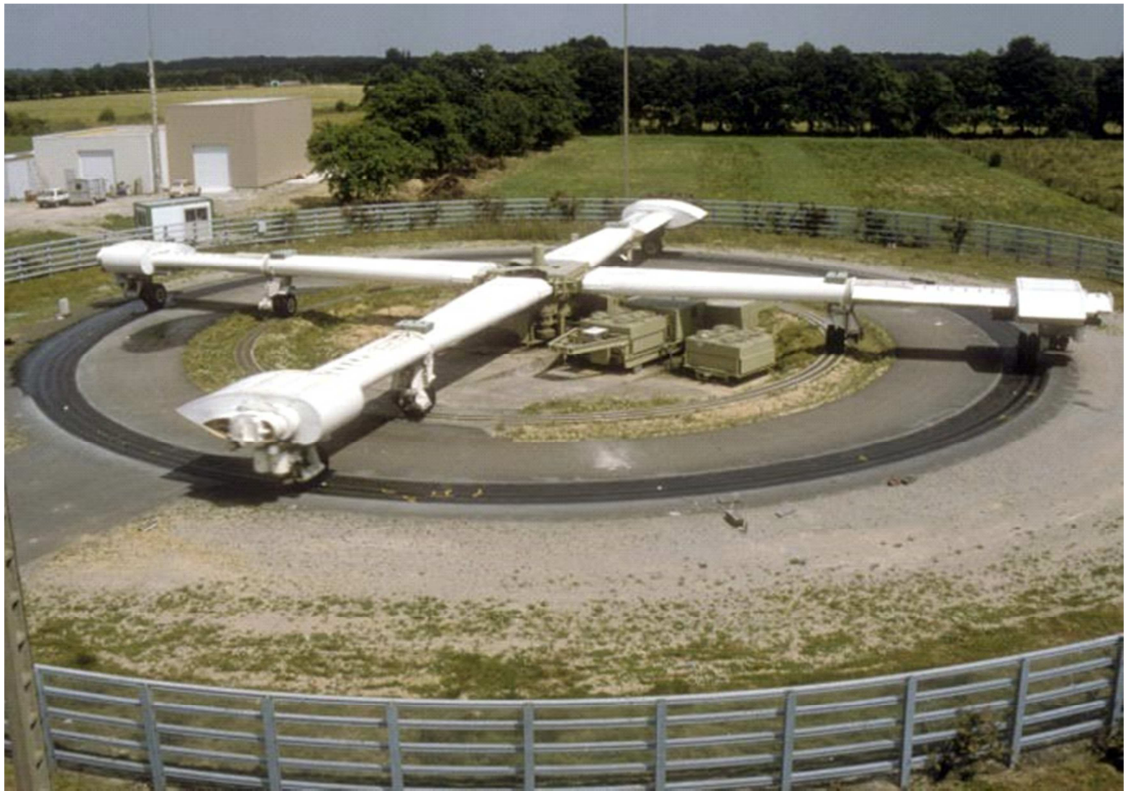

Figure 2-5 The French Rotating Loading Arm (LCPC 2011)

Figure 2-6 Kansas State University APT

2.6 Summary of Literature Review

A large majority of road infrastructure in the world has low traffic volumes. Geosynthetics, especially Geocells, can be a viable rehabilitation material for these roads. Geocell-reinforced base layers have shown to outperform unreinforced layers of the same thickness by increasing bearing capacity and reducing permanent deformation of the surface. The Drucker-Prager model accurately models granular materials, but it tends to give inaccurate results when modeling HMA. The geocells have been modeled in the past using linear elastic plate elements. As of 2004, there were 48 APT facilities in existence worldwide, with 28 of those facilities classified as active. Full-scale APT facilities can be classified as full-scale test roads/tracks or load simulation devices like the CISL APT at Kansas State University.

Chapter 3 - Material Properties

3.1 Geocells and Geotextile

Geocells used in this study were NEOLOY™ polymeric alloy (nanocomposite alloy of polyester/polyamide nano fibers, dispersed in polyethylene matrix) (NPA) geocells. The polymeric alloy has similar flexibility at low temperatures to the high density polyethylene (HDPE) and similar elastic behavior to engineering thermoplastics. The NPA geocell has a wall thickness of 1.1 mm. Han et al. (2011) calculated that NPA geocell materials have a tensile strength of 19.1 MPa (2.77 ksi) and secant elastic modulus of 355 MPa (51.5 ksi) at 2% strain. In this study, a 100-g (3.5 oz) nonwoven geotextile was used in this study as a separator between the subgrade and the base in the geocell-reinforced sections.

3.2 Subgrade

In this study, an AASHTO A-7-6 clay was used in subgrade construction. Optimum moisture content was found to be 21%, with a maximum dry density of 1.61 g/cm^3 (100.5 pcf) (Han et al. 2011). Yang (2010) conducted tests on subgrade material and calculated the Young's modulus to be 10.3 MPa (1,493 psi) and unconfined compressive strength to be 104.6 kPa (15.2 psi).

Plastic Limit (PL), Liquid Limit (LL), and percent finer than 75 μm sieve were found to be 22%, 43%, and 97.7%, respectively, and the plasticity index was 21. For the first four test sections, a subgrade CBR of approximately 6% was achieved in the subgrade at a moisture content of 21%. In the next four test sections, a CBR of 12% was used at a moisture content of 18%.

3.3 Base Material

3.3.1 AB-3

Crushed limestone, AB-3, was used in the control section of this study with no geocells as well as in a test lane with geocell reinforcement. KDOT uses AB-3, a well-graded base material, in a variety of road applications. KDOT specifications and particle size distribution of AB-3 are shown in Figure 3-1. A mean particle size of (d_{50}) of 4.4 mm (0.17 in.), a coefficient of curvature of 7.4, and a coefficient of uniformity of 86 were found.

At optimum moisture content of 10.2%, the CBR of AB-3 is 45% (Pokharel 2010). The maximum dry density was found to be 2.13 g/cm^3 (133.0 pcf). For the first set of four test sections, the AB-3 layer was compacted at a moisture content of 9.17% in the control lane and 9.01% in the geocell lane. In the second set of test sections, the AB-3 layer was compacted at a moisture content of 6.7% in the control lane and 6.3% in the geocell-reinforced lane.

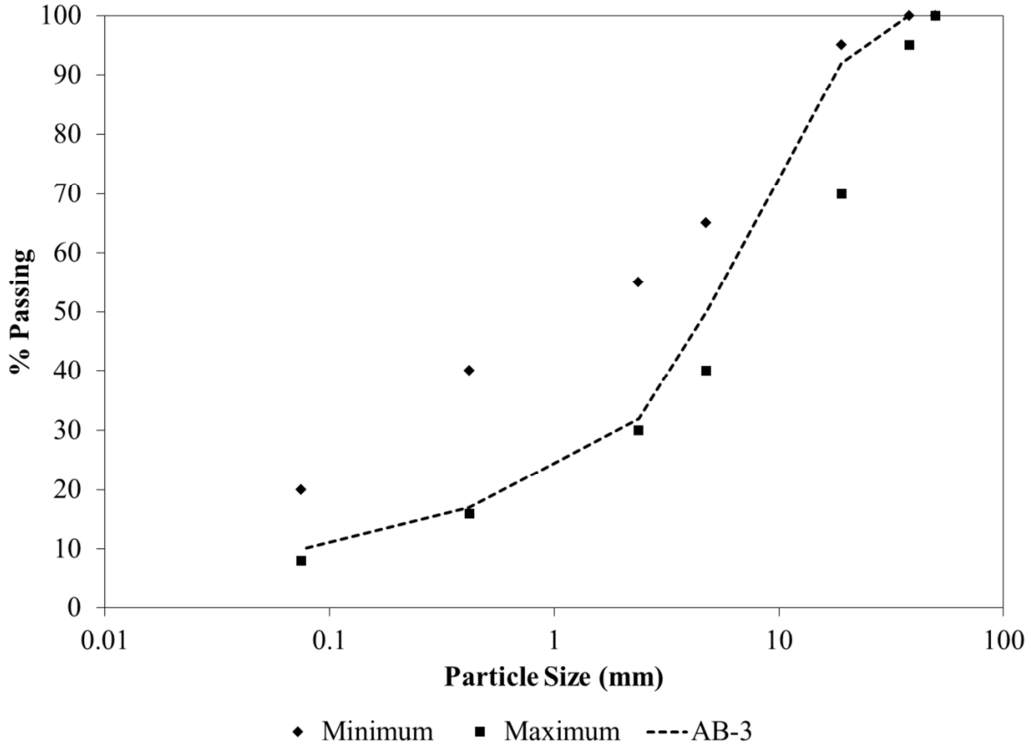

Figure 3-1 KDOT AB-3 control points and grain size distribution of AB-3 base material

3.3.2 Quarry Waste

Eighteen to twenty million tonnes (20 to 22 million tons) of crushed rock are produced annually in Kansas. It is estimated that approximately 35% to 40% of the crushed rock is reduced to fines, or Quarry Waste (QW), some of which is used in HMA production or agricultural applications, leaving approximately 10-20% of QW stockpiled or land-filled annually in Kansas (Frank Rockers and Woody Moses unpublished data). The QW in this study was obtained from a quarry near Manhattan, Kansas. Sieve analysis results from the test done in this study and illustrated in Figure 3-2, showed a mean particle size (d_{50}) of 1.3 mm, a coefficient of curvature of 2.3, and a coefficient of uniformity of 24. Pokharel (2010) found the optimum moisture content to be 11% and maximum dry density to be 2.06 g/cm^3. The optimum moisture content

resulted in a CBR of 19%. In the first and second set of test sections, QW was compacted at moisture contents of 10.6% and 6.8%, respectively.

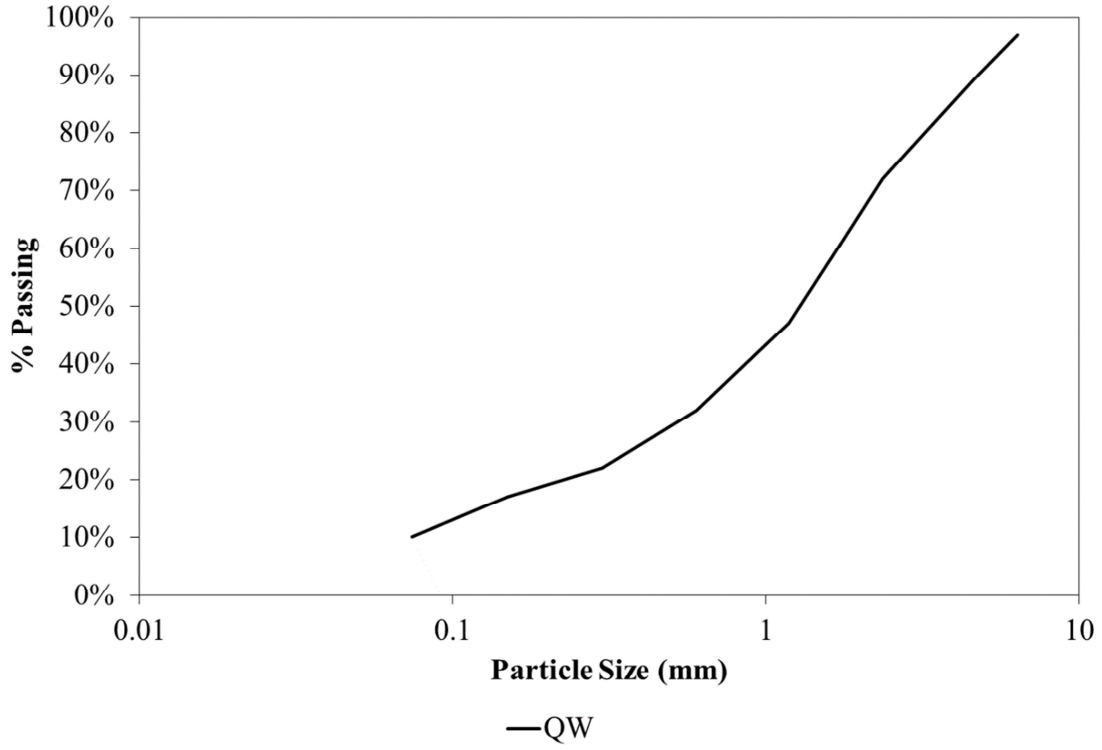

Figure 3-2 Grain size distribution of QW

3.3.3 Reclaimed Asphalt Pavement

In the United States, approximately 91 million tonnes (100 million tons) of RAP are produced each year. Approximately 73 million tonnes (80 million tons) are reused in various aspects of pavement construction (MAPA 2012). The RAP in this study was collected from a local HMA plant in Manhattan, Kansas. Han et al. (2011) found that RAP had an optimum moisture content of 6%, maximum dry density of 1.81 g/cm^3 (113.0 pcf), and CBR value of 10% at 5% moisture content and 8% at optimum moisture content. RAP grain size distribution is shown in Figure 3-3. The ignition oven method was used to determine the binder content of RAP to be 6.5%. In the first and second tests, RAP was compacted at moisture contents of 6.4% and 10.4%, respectively. Water was added to RAP in the second test in order to help compact the RAP into the NPA geocells.

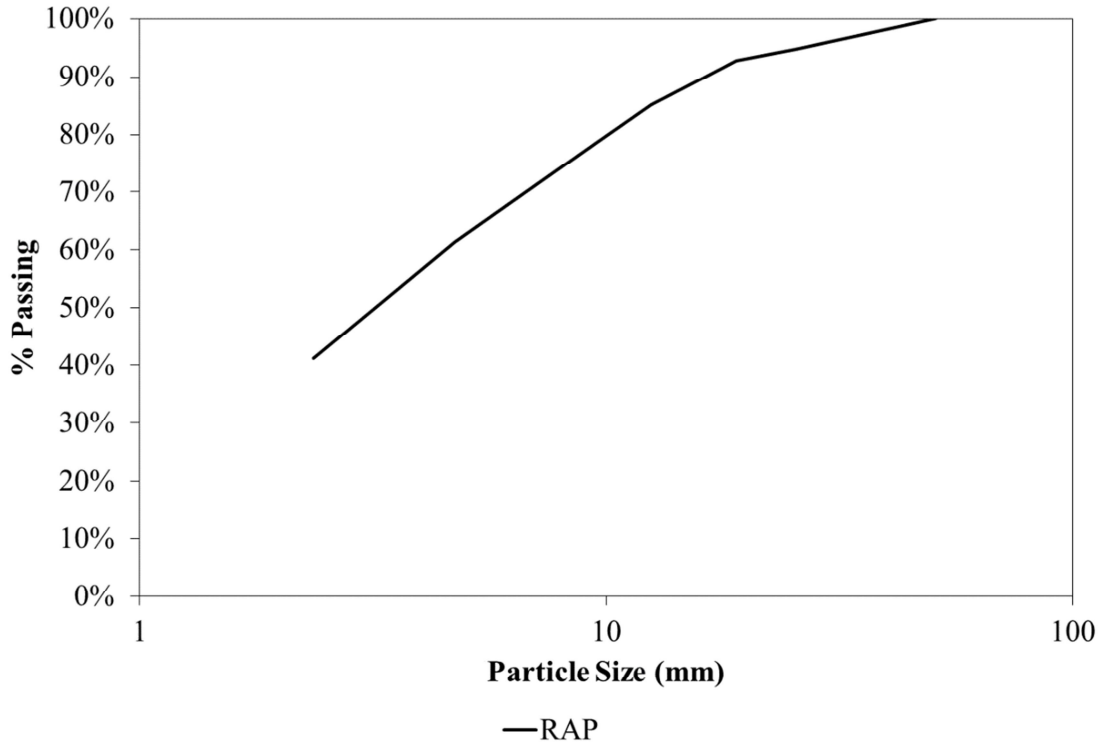

Figure 3-3 Grain size distribution of RAP

3.4 Hot-Mix Asphalt

This study utilized a Superpave mixture (HMA) with 12.5-mm Nominal Maximum Aggregate Size and fine gradation, referred to as SM-12.5A by KDOT. The aggregate blend consisted of 26% 19-mm (0.75-in.) rock, 17% 9.5-mm (0.375-in.) chips, 20% manufactured sand, and 17% concrete sand, with a final gradation, as shown in Figure 3-4. A PG 70-28 binder was used, and the total air void content at N_{design} was 4.04%. HMA properties were found using various laboratory and in-place testing.

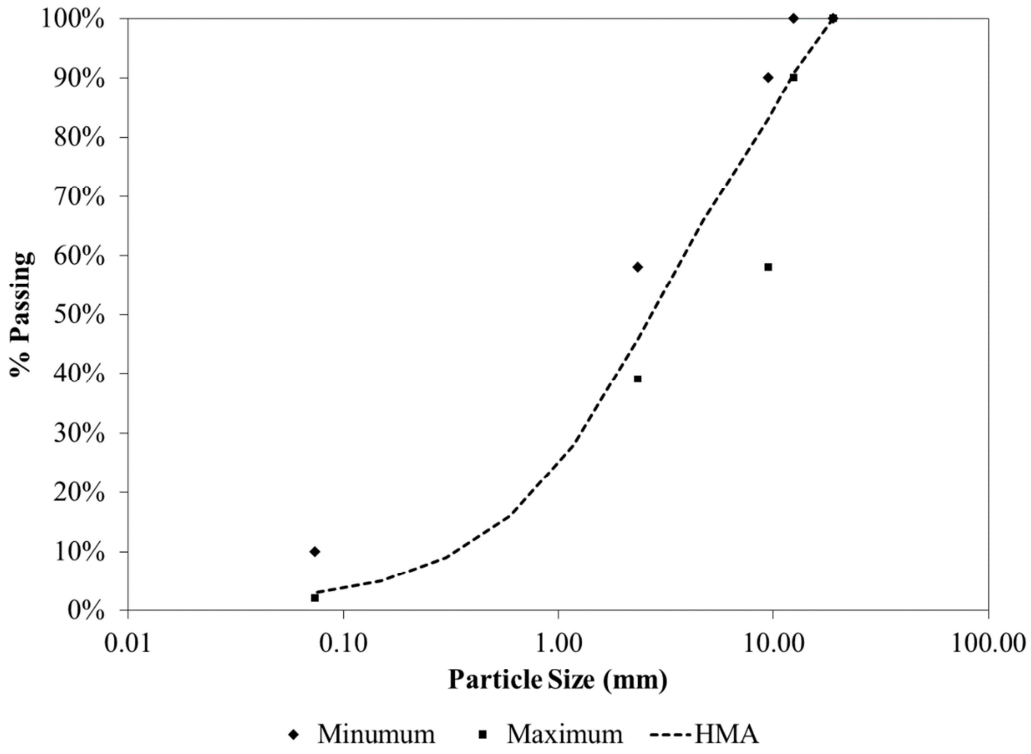

Figure 3-4 HMA gradation with KDOT SM-12.5A control points

3.4.1 Laboratory Testing

3.4.1.1 Dynamic Modulus

The dynamic modulus is the absolute value of the complex modulus. As stated by Brown et al. (2009), "The complex modulus (E*) is defined as a complex number that relates the stress to strain for a linear viscoelastic material subjected to sinusoidal loading." For this study, the dynamic modulus test was performed following AASHTO TP79 (2011) at 4º, 21º, and 37 ºC (40º, 70º, and 100 ºF). A sinusoidal vertical load was applied to 100-mm (4 in.) diameter and 150-mm (6 in.) tall HMA cylinders. During the test, applied stresses and resulting strains were recorded as a function of time and then used to calculate the dynamic modulus and phase angle. The test was conducted in the Asphalt Mixture Performance Tester (AMPT), as shown in Figure 3-5. Four replicates were used during dynamic modulus testing, and results are presented in Table 3-1.

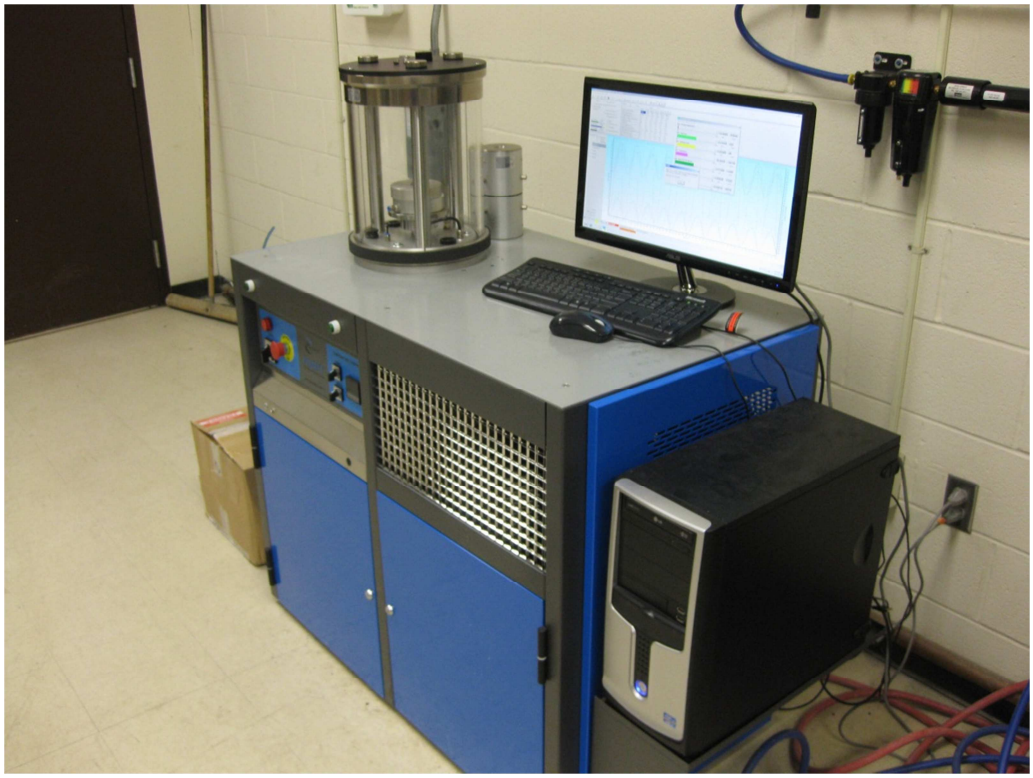

Figure 3-5 KSU AMPT machine

A dynamic modulus master curve was plotted at 23 ºC (73 ºF) as a reference temperature, the temperature of APT testing. The master curve was plotted using Mastersolver Version 2.3 released by Advance Asphalt Technologies, LLC. Three replicate samples were used to calculate the master curve. The sigmoid function equation solved during plotting of the master curve is shown in Equation (3-1). The master curve for HMA is shown in Figure 3-6.

$$\log|E^*| = \log(Min) + \frac{(\log(Max) - \log(Min))}{1 + e^{\beta+\gamma(log\omega+\frac{\Delta E_a}{19.14714}[(\frac{1}{T})-(\frac{1}{T_r})]}} \quad (3\text{-}1)$$

where

$|\boldsymbol{E}^*|$ = dynamic modulus

Min = limiting minimum modulus, ksi

Max = limiting maximum modulus, ksi

ω_r = reduced frequency at the reference temperature

ω = loading frequency at the test temperature, Hz

T_r = reference temperature, ºK

T = test temperature, ºK

ΔE_a = activation energy (treated as a fitting parameter)

B and γ = fitting parameters.

Table 3-1 Dynamic modulus test results (6.89 MPa = 1 ksi)

a. 4 °C (40 °F)

	Sample ID	4 °C (40 °F)					
		25 Hz	10 Hz	5 Hz	1 Hz	0.5 Hz	0.1 Hz
Dynamic Modulus (MPa)	1	15634	14276	13435	11488	10655	8791
	2	17636	18615	17592	15635	14512	12180
	3	16953	16191	15352	13647	12676	10524
	4	17962	16320	15798	13622	12610	10364
	Average	17046.25	16350.5	15544.25	13598	12613.25	10464.75
	SD	1031.1	1775.5	1707.1	1693.5	1575.2	1385.3
	CV (%)	6.05	10.86	10.98	12.45	12.49	13.24
Phase Angle (Degrees)	1	7.44	8.47	9.15	10.89	11.72	13.95
	2	3.73	6.57	7.65	8.98	9.79	11.64
	3	7.13	9.92	8.58	9.73	10.51	12.61
	4	7.36	9.88	8.88	10.36	11.19	13.59
	Average	6.4	8.7	8.5	9.9	10.8	12.9
	SD	1.794	1.577	0.652	0.823	0.837	1.039
	CV (%)	27.98	18.1	7.6	8.2	7.75	8.03

b. 21 °C (70 °F)

	Sample ID	21 °C (70 °F)					
		25 Hz	10 Hz	5 Hz	1 Hz	0.5 Hz	0.1 Hz
Dynamic Modulus (MPa)	1	10005	9160	8300	6333	5599	3948
	2	15179	11958	10830	8426	7383	5348
	3	12608	11822	9801	7588	6695	4752
	4	10735	9356	8322	6133	5327	3633
	Average	12131.7	10574	9313.2	7120	6251	4420.25
	SD	2308.4	1522.7	1231.2	1082.9	958.72	777.5
	CV (%)	19.03	14.40	13.22	15.21	15.34	17.59
Phase Angle (Degrees)	1	16.33	14.05	15.03	17.95	19.28	22.85
	2	21.04	12.82	13.53	16.18	17.45	20.75
	3	5.08	11.53	14.01	16.67	17.97	21.52
	4	15.36	15.81	16.92	20.29	21.64	25.29
	Average	14.4525	13.5525	14.8725	17.7725	19.085	22.6025
	SD	6.722	1.823	1.501	1.836	1.869	1.990
	CV (%)	46.5	13.45	10.10	10.3	9.79	8.81

c. 37 °C (100 °F)

	Sample ID	37 °C (100 °F)					
		25 Hz	10 Hz	5 Hz	1 Hz	0.5 Hz	0.1 Hz
Dynamic Modulus (MPa)	1	4480	3566	2983	1840	1503	859
	2	5159	4162	3512	2253	1870	1128
	3	4429	3513	2929	1815	1480	860.9
	4	4341	3393	2789	1651	1317	728.5
	Average	4602.25	3658.5	3053.25	1889.75	1542.5	894.1
	SD	375.58	343.37	316.57	256.26	233.50	167.79
	CV (%)	8.16	9.39	10.37	13.56	15.14	18.77
Phase Angle (Degrees)	1	24.19	26.08	27.16	29.77	29.99	30.87
	2	23.36	24.82	25.85	28.45	28.73	29.81
	3	24.37	26.11	27.09	29.36	29.42	29.9
	4	25.94	27.81	28.79	31.1	31.08	31.33
	Average	24.465	26.205	27.2225	29.67	29.805	30.4775
	SD	1.077	1.227	1.2058	1.101	0.993	0.743
	CV (%)	4.40	4.68	4.43	3.71	3.33	2.44

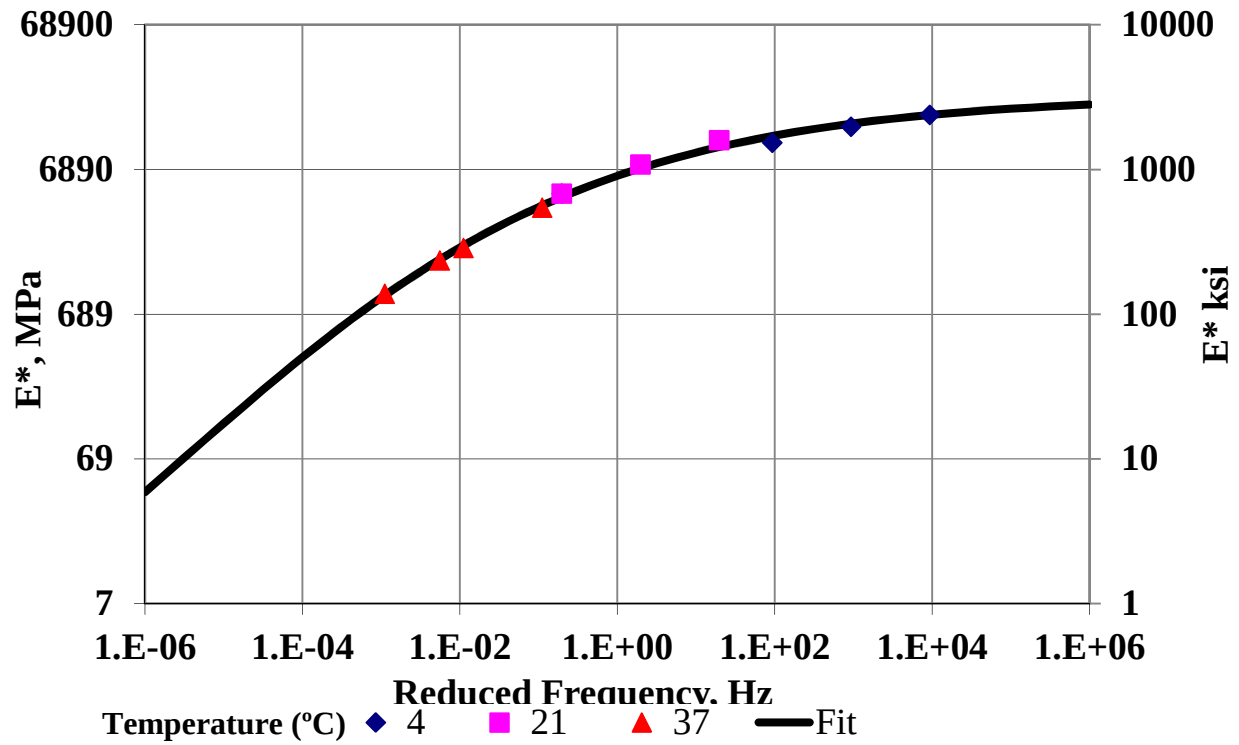

Figure 3-6 Master curve plot at 23 ºC (73 ºF)

Vehicles traveling across HMA pavement induce loading with a corresponding frequency. Therefore, HMA has a typical dynamic modulus corresponding to the specific pavement service temperature and traffic loading frequency. MEPDG provides recommendations for the frequency to be used for determination of dynamic modulus. The approximation ratio of speed (mph) to frequency (Hz) is approximately 2:1 (NCHRP 2011). APT testing was conducted at 11.3 km/hr (7 mph), thereby inducing loading with a frequency of 3.5 Hz. As shown in Figure 3-6, the corresponding dynamic modulus at 3.5 Hz is approximately 7,500 MPa (1,090 ksi).

3.4.1.2 Hamburg Wheel-Tracking Machine Test

Rutting and moisture susceptibility of HMA were tested following AASHTO T 324. Hamburg wheel-tracking tests, typically used to "determine the premature failure susceptibility of HMA due to weakness in the aggregate structure, inadequate binder stiffness, or moisture damage" (AASHTO T 324 2004), is completed by rolling loaded wheels across HMA specimens immersed in a temperature-controlled water bath. Figure 3-7 shows the Hamburg wheel-tracking machine, and Figure 3-8 shows samples being tested.

Figure 3-7 Hamburg wheel-tracking machine

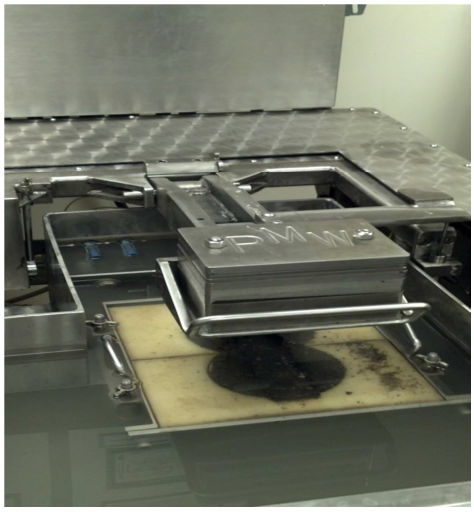

Figure 3-8 Hamburg samples under testing

Rut depths measured during testing are graphically represented in Figure 3-9. AASHTO T 324 is typically run until 20,000 passes and the failure depth is set by a highway agency. The Texas Department of Transportation (TXDOT) sets a failure depth of 12.5 mm (0.5 in.) (Button et al. 2004). However, for this study, 40,000 passes were completed without reaching the study failure depth of 12.5 mm. Figure 3-10 shows the tested specimens.

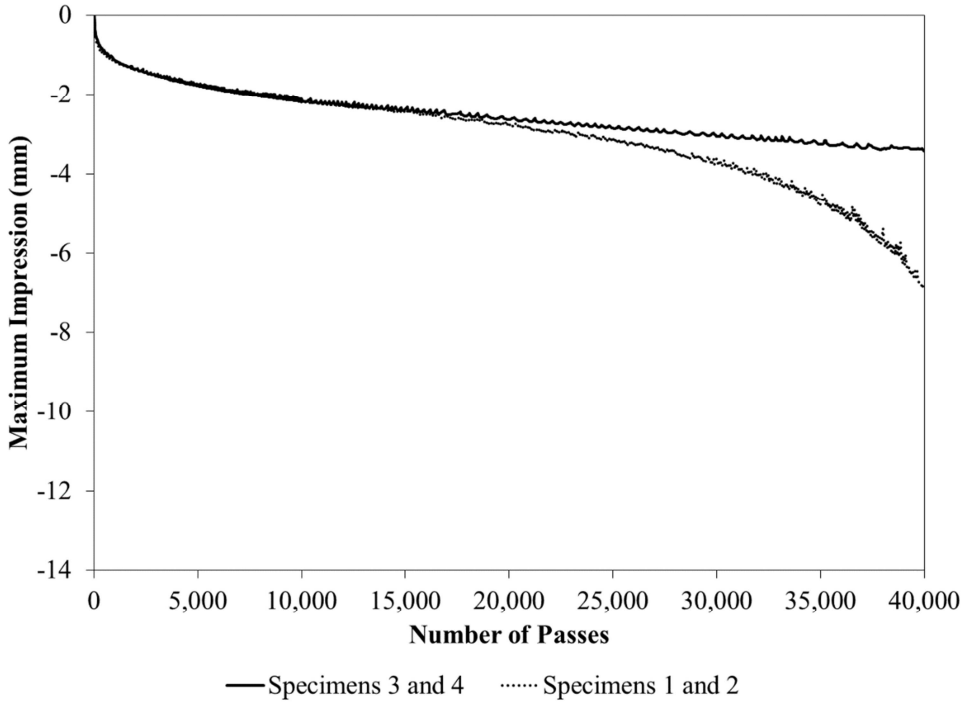

Figure 3-9 Hamburg results

The creep slope, which is the inverse of the rate of deformation in the linear region of the deformation curve after compaction happens, was obtained from the Hamburg wheel-tracking test results. Rutting from the plastic flow is related to the creep slope, and the stripping slope begins at the Stripping Inflection Point (SIP). Stripping slope is the inverse of the rate of deformation in the linear region of the deformation curve after the SIP (Aschenbrener et al. 1994 and Brown et al. 2009). Figure 3-11 illustrates these slopes on a typical plot of Hamburg wheel test results. A comparison of Figure 3-9 and Figure 3-11 reveals that the HMA used in this study reached 20,000 passes without reaching the SIP, thereby indicating a high quality HMA in regards to rutting performance goes.

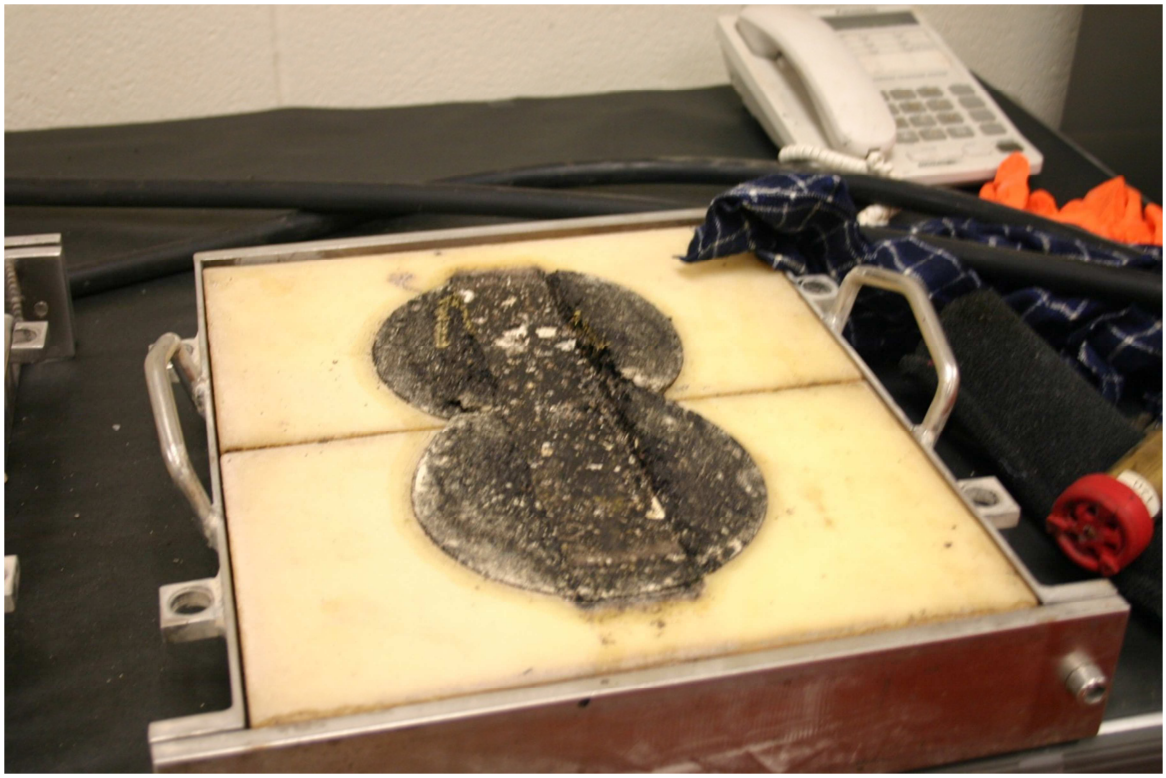

Figure 3-10 Completed Hamburg samples

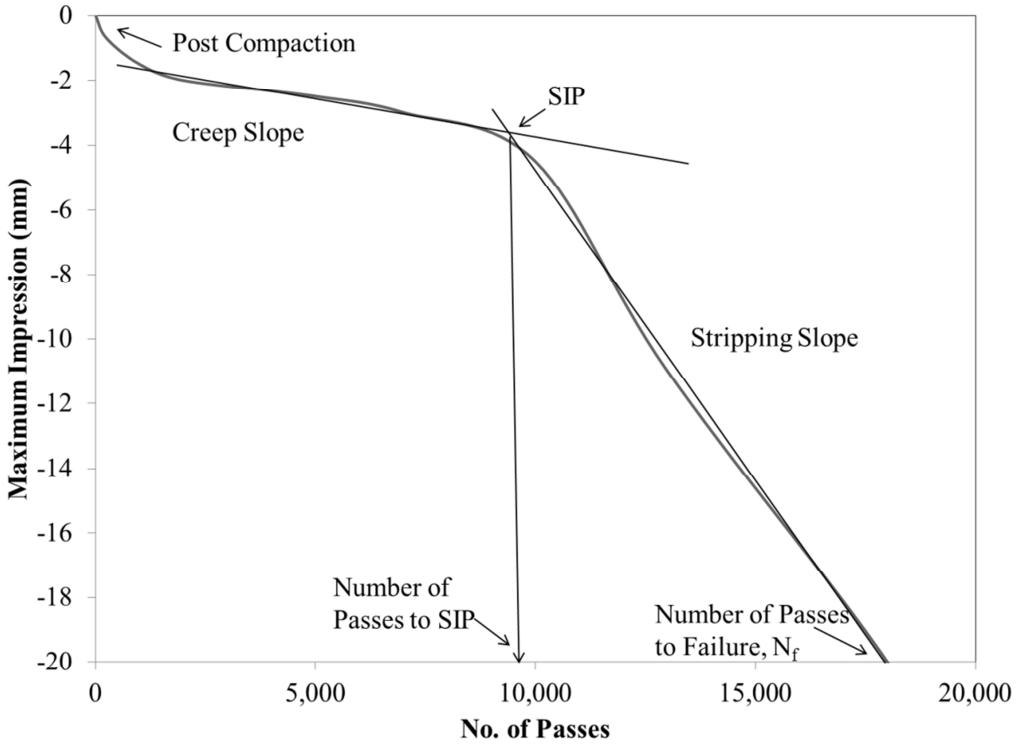

Figure 3-11 Hamburg test output with test parameters (after AASHTO T 324 2004)

3.4.1.3 Flow Time Test

The flow time test is a static creep test that gives flow time or "… the length of time the pavement can withstand steady pressure until flow occurs, causing permanent deformation" (Brown et al. 2009). Appendix C of the NCHRP Report No. 465 (NCHRP 2002) outlines the flow time test procedure. This test can be conducted with or without use of a confining stress. A specimen is loaded with a target deviator stress, and the load is held until total stain reaches 5%. Three stages of creep (primary, secondary, and tertiary) were obtained in this test. A nonlinear relationship between strain and time was evident in the primary and tertiary stages. Secondary creep typically has a constant strain rate with loading. Flow time is the point at which tertiary creep begins. Figure 3-12 shows the three stages of creep.

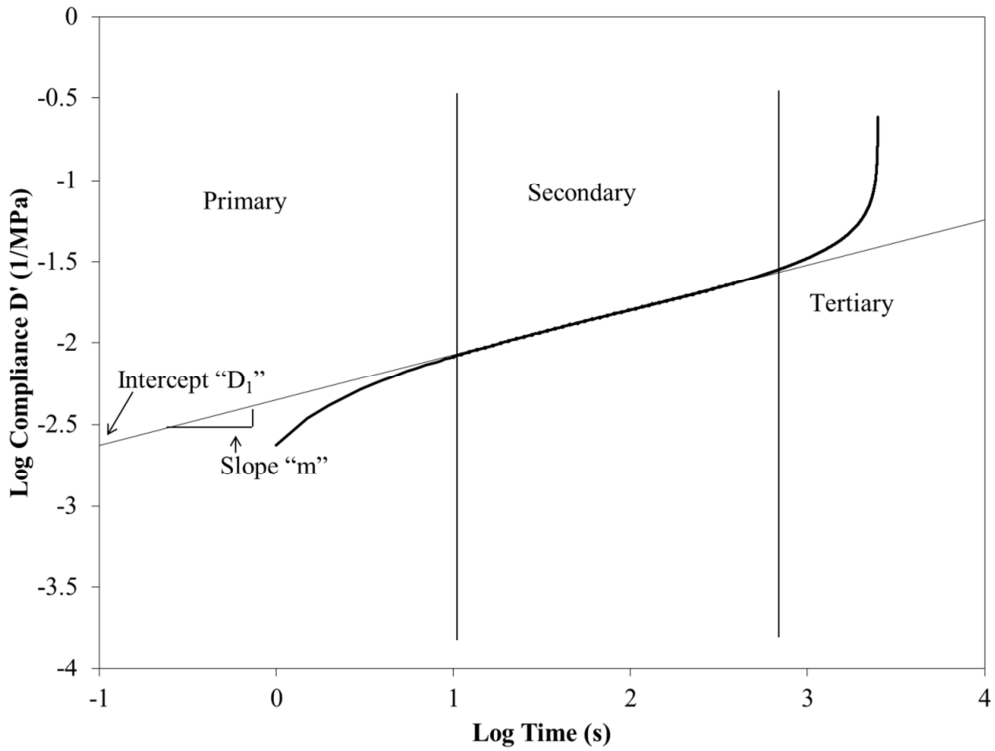

Figure 3-12 Creep compliance versus time (after Brown et al. 2009)

Secondary creep is linear, and creep information can be obtained from the secondary region of Figure 3-12. Axial creep compliance at any time can be determined by Equation (3-2). A power law model was used to describe the secondary stage of creep compliance, as shown in Equation (3-3) (Brown et al. 2009).

$$D(t) = \frac{\varepsilon(t)}{\sigma_0} \tag{3-2}$$

where

$D(t)$ = creep compliance

$\varepsilon(t)$ = strain response

σ_0 = applied stress.

$$D(t) = D_0 + D_1 t^m \tag{3-3}$$

where

D_0 = instantaneous compliance

t = time

D_1 = time-dependent creep compliance at a time of one second

m = slope of the creep compliance-time relationship in log-log scale.

Flow time was conducted at 57 ºC (135 ºF) with no confining stress and deviator stress of 207 kPa (30 psi). Two specimens were tested, and results are presented in Table 3-2.

Table 3-2 Flow time test results

Sample ID	D_1	m	D_0	Flow Time
1	0.00445	0.2766	0.00627	603.5
2	0.00417	0.256	0.00571	1284
Average	0.00431	0.2663	0.00599	943.75

3.4.1.4 Flow Number Test

The flow number test gives the number of load cycles a pavement can tolerate before the HMA deforms in a plastic manner. Appendix B in the NCHRP Report No. 465 (NCHRP 2002) outlines specifications of the test. In general, flow number tests and flow time tests are similar; however, the flow number test uses haversine loading of 0.1 second, followed by 0.9 second of rest. This cyclic loading simulates a heavy vehicle driving repeatedly over a pavement structure (Brown et al. 2009). Again, the three stages of creep can be observed during testing, and data collected during this test is used to calculate dynamic creep parameters, intercept "a," slope "b," and flow number (F_n), as shown in Figure 3-13. F_n is defined as the cycle at which tertiary flow begins. A power law can be used to model the relationship between permanent strain and the number of loading cycles in the secondary zone, as shown in Equation (3-4).

$$\varepsilon_p = aN^b \tag{3-4}$$

Confining stress is again optional in this Flow Number test and was not used in this study. A deviator stress of 207 kPa (30 psi) at 57 ºC (135 ºF) was used. Results for the HMA used in this study are presented in Table 3-3, and a specimen after the flow time test is shown in Figure 3-14.

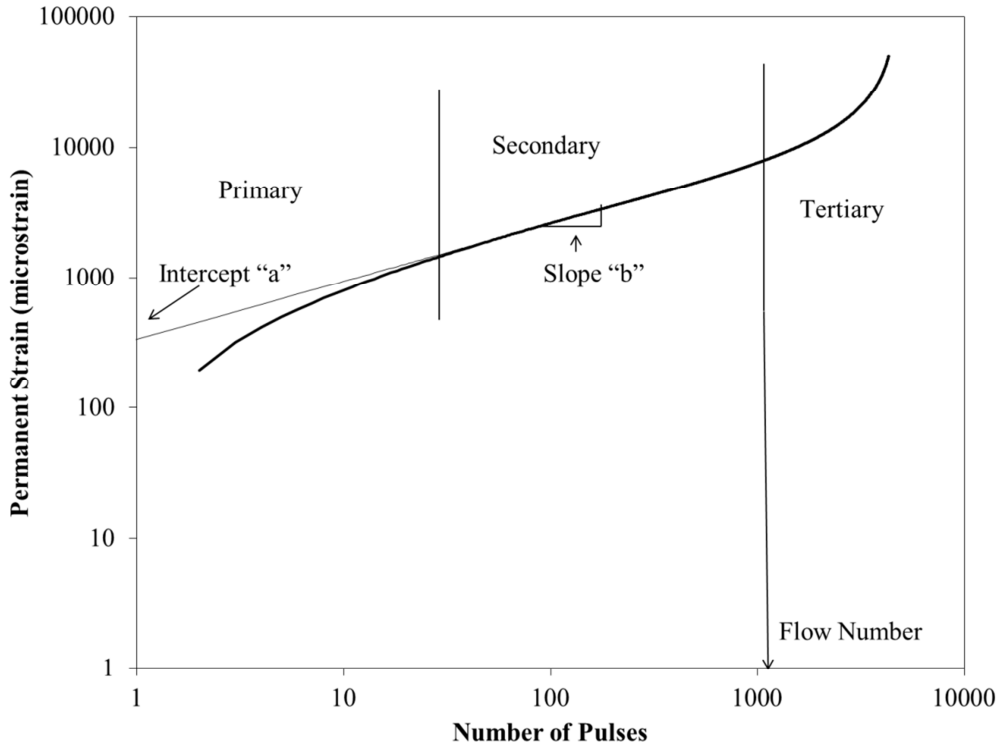

Figure 3-13 Permanent strain versus number of cycles (after Brown et al. 2009)

Table 3-3 Flow number test results

Sample ID	Dynamic Creep Parameters		
	a ($x10^{-6}$)	b	FN
1	335.02	0.4459	1494
2	341.71	0.4518	842
Average	338.37	0.4489	1168

Figure 3-14 Failed specimen

3.4.2 In-place Testing

3.4.2.1 Density

In-place density in both set of APT test sections was 92% of the theoretical maximum specific gravity of 2.452. This density was measured using a nuclear gage.

3.4.2.2 Falling Weight Deflectometer

Falling weight deflectometer (FWD) testing is a nondestructive test used to evaluate pavement structural condition. In FWD, a mass is dropped from a certain height in order to transmit a dynamic load to the pavement structure to simulate a moving wheel load. Geophones at various distances from the loading plate measure surface deflections on the pavement, and deflection measurements are input into a backcalculation program to determine the modulus of each pavement structure layer (TxDOT 2008). In most cases, backcalculation is an iterative elastic analysis of pavement surface deflection basin. Measured deflections are then compared to calculated deflections with associated layer moduli until a pre-determined match is reached (WSDOT 2005). KDOT performed FWD testing for this study using a Dynatest FWD, as shown

in Figure 3-15. Testing was conducted after completion of paving and at scheduled intervals during APT loading. The Washington State Department of Transportation (WSDOT) developed the Everseries backcalculation program used in this study. Variables set in the backcalculation process are listed in Table 3-4, and resulting backcalculated moduli are tabulated in Table 3-5 and Table 3-6. Because the pits were surrounded by concrete on three sides and at the bottom and in order to reduce the percent root mean square (%RMS) error, only the first four sensors were used during backcalculation. During the first test, the control section had the strongest base layer. In the second test, the modulus increased through the first 500,000 passes and then began to decrease. Backcalculation results verified a stronger subgrade in the second test compared to the first test.

Figure 3-15 KDOT Dynatest FWD

Table 3-4 Everseries variables

Variable	Set Point
Depth	Cross section dependent
Poisson Ratio	
HMA	0.35
Base/Geocell Layer	0.4
Subgrade	0.45
Concrete Bottom	0.45
Targeted %RMS	<1%
Analyzed Loads	≈9,000 lbs
Number of Sensors used	4

Table 3-5 Backcalculated moduli for first experiment and overlay experiment

	Layer	Number of Passes		
		0K	**0K OL**	**50K OL**
CTL	**HMA (MPa)**	3954	2557	3789
	Base (MPa)	115	93	106
	Subgrade (MPa)	64	61	60
QW	**HMA (MPa)**	3083	1417	2053
	Base (MPa)	43	338	308
	Subgrade (MPa)	39	47	54
RAP	**HMA (MPa)**	2165	1426	2518
	Base (MPa)	34	36	115
	Subgrade (MPa)	43	43	47
AB3	**HMA (MPa)**	2154	1416	2057
	Base (MPa)	35	235	596
	Subgrade (MPa)	45	44	49

Table 3-6 Backcalculated moduli for second experiment

	Layer	Number of Passes				
		0K	250K	500K	1M	1.2M
CTL	HMA (MPa)	6468	5425	5507	4333	8650
	Base (MPa)	308	352	358	179	69
	Subgrade (MPa)	68	63	71	88	101
QW	HMA (MPa)	4867	6569	4511	3451	6602
	Base (MPa)	328	388	545	112	122
	Subgrade (MPa)	52	55	58	63	71
RAP	HMA (MPa)	4947	4947	3977	3608	9000
	Base (MPa)	140	311	325	89	58
	Subgrade (MPa)	58	66	75	84	81
AB3	HMA (MPa)	3848	5212	3020	3268	5536
	Base (MPa)	193	212	279	35	44
	Subgrade (MPa)	59	53	55	64	62

Chapter 4 - Accelerated Pavement Testing

4.1 Civil Infrastructure Systems Laboratory

APT is conducted in the main space of the CISL at KSU. Three testing pits are available for use: each pit is 1.8 m (6 ft.) deep, approximately 6.1 m (20 ft.) long, and 4.9 m (16 ft.) wide. The APT machine used to apply loading to the pits consists of a 12.8 m (42 ft.) reaction frame that can accommodate an assembly containing single, dual, or super-single tires on single or tandem axles. The assembly is driven by a belt powered by a 20 HP electric motor and a variable frequency drive (VFD) to control speed and direction. As shown in Figure 4-1, a chamber around the machine is used to control ambient temperature during testing.

Figure 4-1 Environmental chamber around APT machine

Loading can be completed in a uni-directional or bi-directional mode. The speed of the bogie is 11.3 km/hr (7 mph), resulting in the ability to apply 100,000 wheel load applications bi-directionally per week. Hydraulic cylinders apply and remove the load via an onboard pump. Traffic wander is simulated by a lateral wandering device that moves the entire frame in a lateral direction of ±150 mm (± 6 in.). The wander is input from a user-defined interface in steps of 12.5 mm (0.5 in.) (Lewis 2008).

4.2 CISL 16

This study was the 16th CISL experiment since 1997. The objective of the APT portion of the project was to test a geocell design with various infill materials and a thin HMA overlay under real-world simulated traffic on a marginal subgrade. Three types of infill materials (crushed limestone, AB-3; QW; and RAP) were tested. Two pits were subdivided into two test sections, or lanes, each. These lanes were expected to be loaded to 1,000,000 repetitions in the bi-directional mode by an 80-kN (18-kip) single-axle load assembly. Due to premature failures and machinery breakdowns, three experiments were conducted. The experiments were referred to as first (thin) experiment, overlay experiment, and second (thick) experiment.

All three experiments were conducted with a single-axle, dual-tire bogie with a tire pressure of 552 kPa (80 psi). Experiments were conducted at a temperature of 23 °C (73 °F). A traffic wander of ±150mm (±6 in.) was used in all three experiments. A complete wander from 150 mm (-6 in.) to +150 mm (+6 in.) required 676 passes. Wheel wander distribution, a truncated normal distribution, is shown in Figure 4-2.

Test lanes were fully instrumented with stress and strain sensors, as shown in Figure 4-3. Data was recorded using a compact data acquisition system during load application at prescribed intervals for a full wander cycle (676 passes). Instrumentation for each section included four H-Bar strain gauges below the HMA layer, two Type T thermocouples below the HMA layer, two pressure cells below the base layer, and five strain gauges glued with epoxy to the geocell walls.

4.2.1 General Test Preparation

All pavement test sections in this study were built with the same construction technique. A-7-6 clay soil was placed in 150-mm (6 in.) lifts for building the subgrade layer. In the first experiment, the subgrade was compacted with a combination of a “jumping jack” compactor and a vibratory plate compactor. In the second experiment, a sheepsfoot trench compactor was used for compaction. The degree of compaction was checked using a Dynamic Cone Penetrometer (DCP) until the desired CBR for each lift was reached. Pressure cells were installed on top of the subgrade, as shown in Figure 4-4, and a layer of nonwoven geotextile was placed on top of the subgrade. The geotextile was used as a separation layer only; no reinforcement credit was

expected. Steel bars were driven into the subgrade to hold the geocells during installation and placement of infill, as shown in Figure 4-5.

After infill materials were placed in the geocells, the steel bars were removed and the vibratory plate compactor began compaction of the infill, as shown in Figure 4-6. A 3,600 kg (4 ton) roller compactor was used to finish compaction of the infill and cover, as shown in Figure 4-7. By using the roller compactor, the target density of the infill in all test sections was more easily reached. The target density was 95% of the maximum dry density as determined by standard Proctor tests. Infill density was determined using a nuclear density gauge.

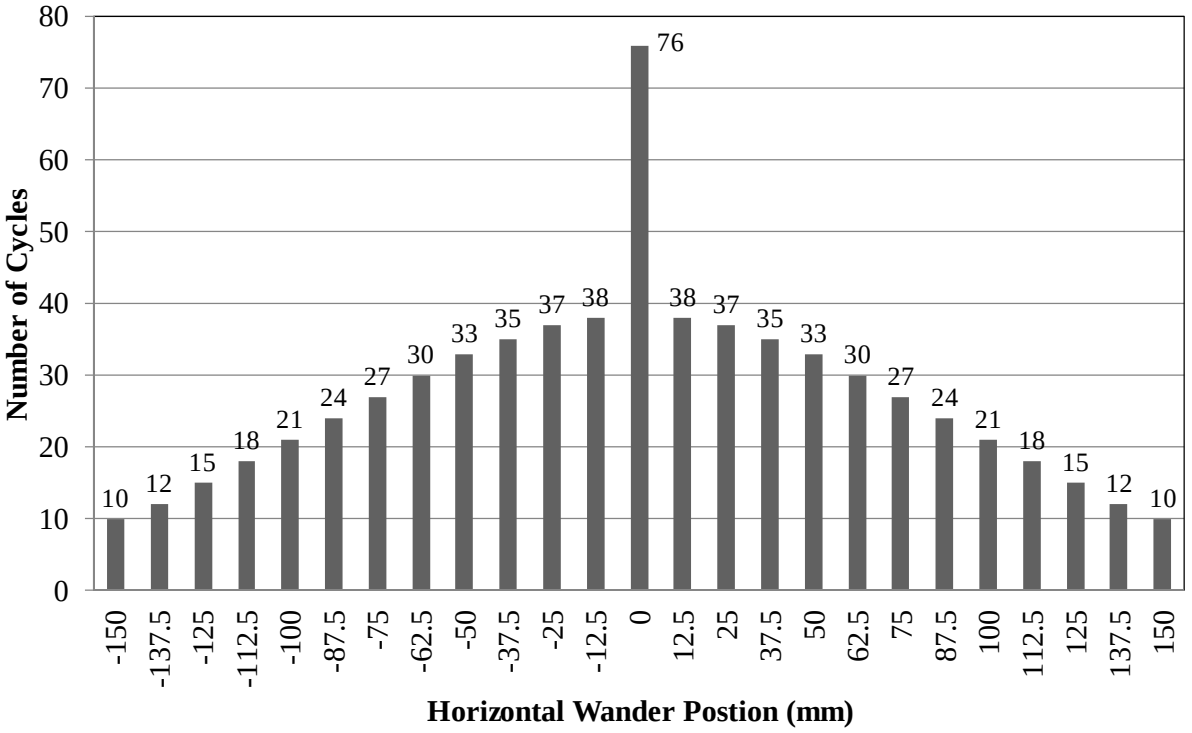

Figure 4-2 Wheel wander distribution

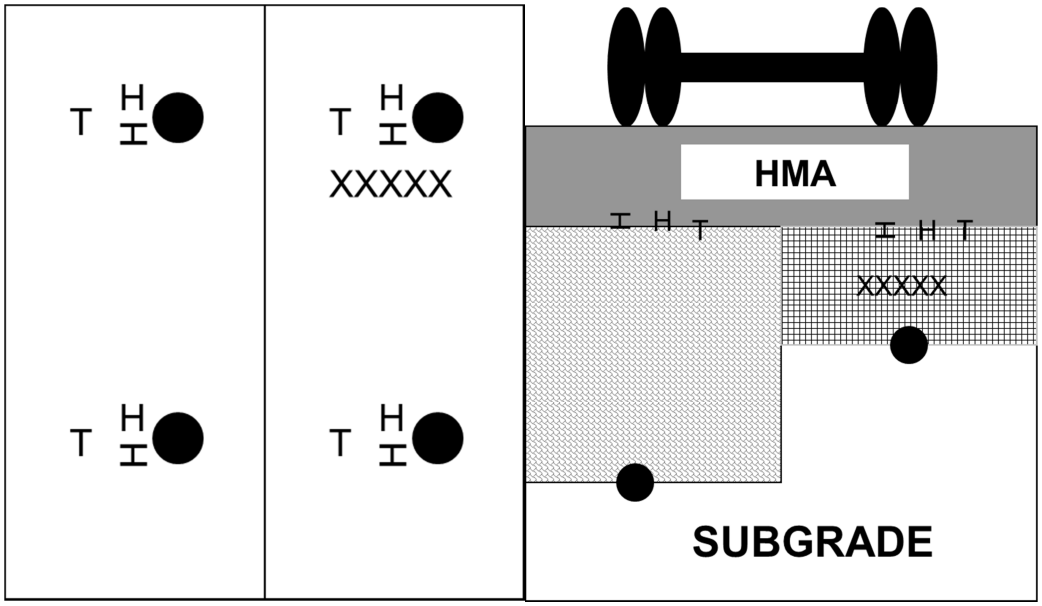

Top View Side View

H – H-Bar Strain Gauge X-Geocell Strain Gauge

T- Thermocouple ● - Pressure Cell

Figure 4-3 Instrumentation layout

Figure 4-4 Pressure cells installed in subgrade

Figure 4-5 Geocell installation

Figure 4-6 Infill after vibratory plate compaction

Figure 4-7 Roller compaction of infill

Once the base layer (geocells with infill) was compacted to the desired level, H-bar strain gauges and thermocouples were installed on top of the base layer. HMA was produced, delivered, and placed by a local contractor. A Superpave HMA mix was placed with a lightweight asphalt paver, as shown in Figure 4-8. In order to protect the strain gauges and thermocouples, they were covered before paving commenced. A 3,940 kg (4.3 ton) asphalt roller compactor was used to compact the HMA, as shown in Figure 4-9. A target density of 92% of theoretical maximum density was intended. A nuclear density gauge was used to test for density compliance. After paving, KDOT performed FWD testing before any APT loading started. An initial profile was taken using a transverse profiler, shown in Figure 4-10. APT testing began as soon as all preliminary testing was completed. Profiles were taken at scheduled intervals. FWD testing was also completed after scheduled intervals.

Figure 4-8 Lightweight asphalt paver

Figure 4-9 Asphalt compactor

Figure 4-10 Transverse profiler

4.2.2 First (Thin) Experiment

The first experiment consisted of four paved test lanes. The original four lanes consisted of the following base thicknesses and a 50-mm HMA layer (Figure 4-11):

- Lane 1 – 300-mm thick crushed limestone (AB-3) aggregate (control)
- Lane 2 – 75-mm geocell-reinforced QW plus 25-mm cover
- Lane 3 – 75-mm geocell-reinforced RAP plus 25-mm cover
- Lane 4– 75-mm geocell-reinforced AB-3 plus 25-mm cover.

The subgrade was compacted to a CBR of 6% at a moisture content of 21%. The control section out of AB-3 was compacted with a moisture content of 9.2% and a dry density of 2.03 g/cm^3 (126.73 pcf). The AB-3 geocell-reinforced section was compacted at 9.0% moisture content to a dry density of 2.03 g/cm^3 (126.73 pcf). The QW geocell-reinforced section was compacted at 10.6% moisture content and dry density of 1.95 g/cm^3 (121.73 pcf); the RAP geocell-reinforced section was compacted at 6.4% moisture content and dry density of 1.78 g/cm^3 (111.12 pcf). HMA was compacted until a density of 2.250 g/cm^3 (140 pcf) was reached. Under APT loading, thin test sections failed. The QW lane failed dramatically, as shown in

Figure 4-12. Therefore, a steel plate was placed over the failed area to allow for continuation of testing other lanes. However, the rest of the lanes also failed quickly, as explained in Chapter 6. An overlay was placed over the pavement sections in order to continue testing.

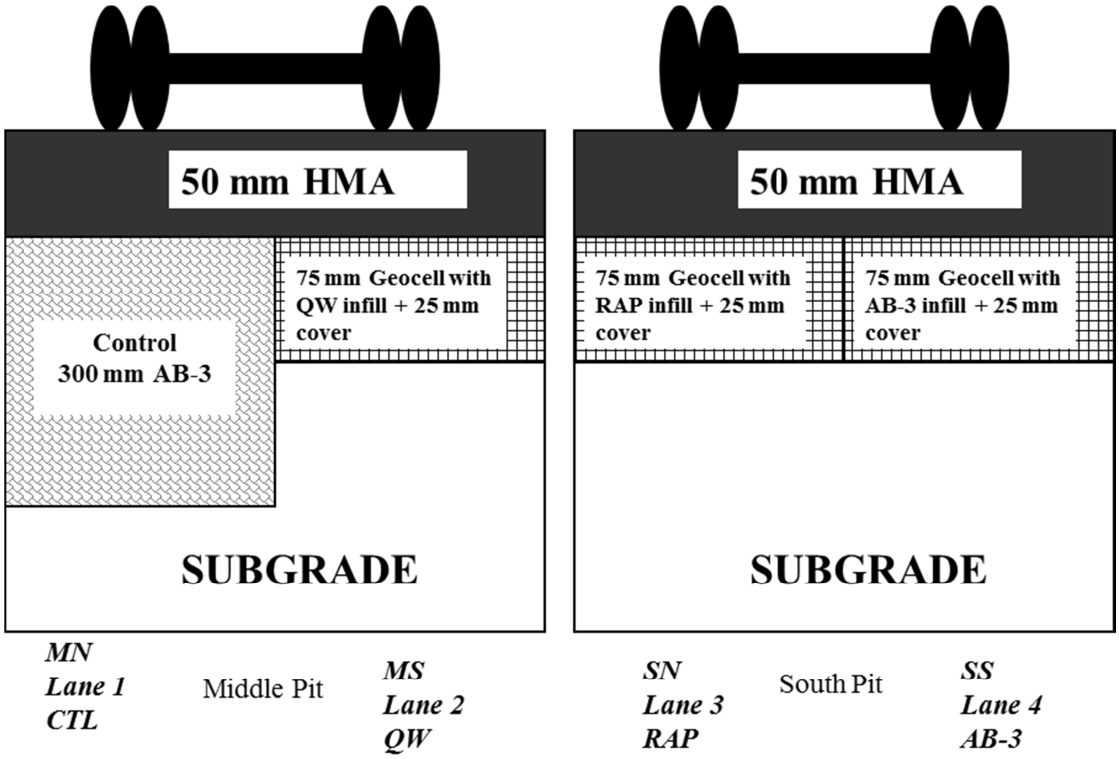

Figure 4-11 Thin cross sections

4.2.3 Overlay Experiment

A 37.5-mm (1.5-inch) HMA overlay was placed over the failing sections, resulting in a cross section shown in Figure 4-13. However, this overlay elevation was beyond the working range of the APT machine, resulting in multiple machine breakdowns. A decision was then made to terminate testing.

Figure 4-12 QW lane failure first experiment

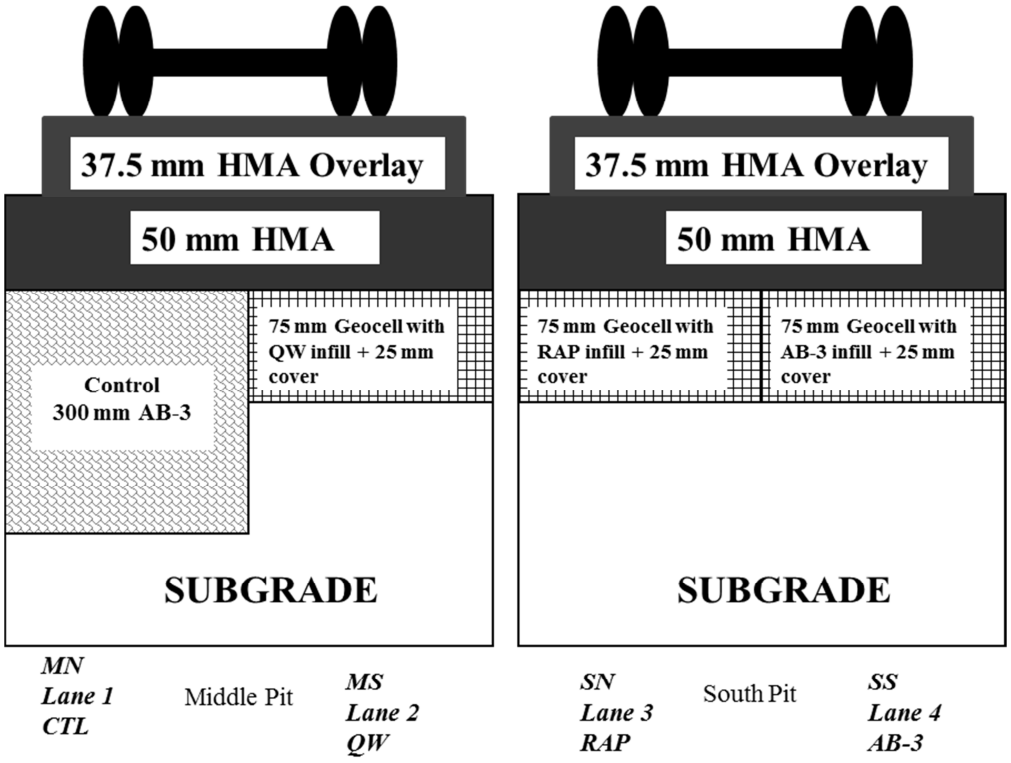

Figure 4-13 Overlay cross sections

4.2.4 Second (Thick) Experiment

Thick cross sections were designed based on linear elastic evaluation of stresses on the subgrade, as described in Chapter 5. The subgrade was compacted to a CBR of 12% after calculations showed similar in-situ CBRs on most KDOT reconstruction projects. The subgrade was compacted at 18% moisture content, and then the sections were reconstructed. The thick cross sections had a 100-mm HMA layer with the following base thicknesses (shown in Figure 4-14):

- Lane 1 – 200-mm thick AB-3 aggregate (control)
- Lane 2 – 100-mm geocell-reinforced QW plus 50-mm cover
- Lane 3 – 100-mm geocell-reinforced RAP plus 50-mm cover
- Lane 4– 100-mm geocell-reinforced AB-3 plus 50-mm cover.

The control section of AB-3 was compacted with a moisture content of 6.7% and a dry density of 2.03 g/cm^3 (126.73 pcf), and the AB-3 geocell-reinforced section was compacted at 6.3% content to a dry density of 1.97 g/cm^3 (122.98 pcf). The QW geocell-reinforced section was compacted at 6.8% moisture content and a dry density of 1.97 g/cm^3 (122.98 pcf), and the RAP geocell-reinforced section was compacted at 6.4% moisture content with a dry density of 1.81 g/cm^3 (112.99 pcf). HMA was compacted until a density of 2.250 g/cm^3 (140 pcf) was reached.

APT machine passes were applied until 500,000 passes or a rut depth of 12.5 mm was reached (whichever came first). The second test section did not fail at the completion of 500,000 passes, the decision was made to apply 1,200,000 passes.

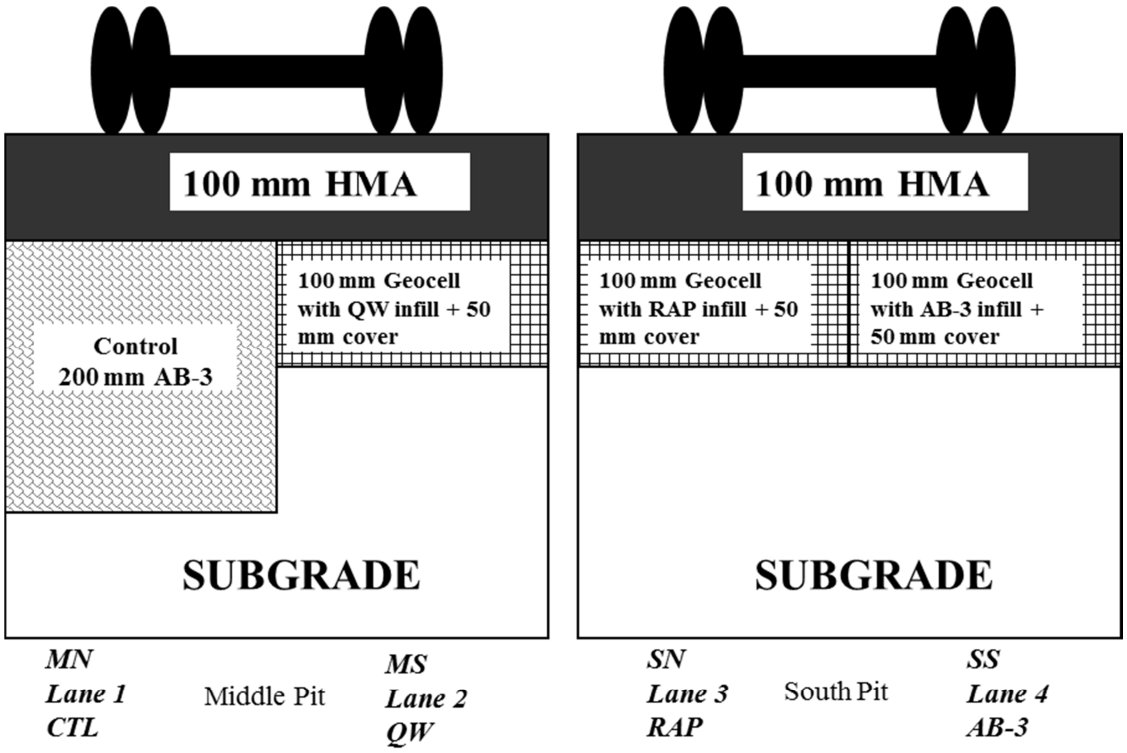

Figure 4-14 Thick cross sections

Chapter 5 - Numerical Simulation of APT Tests

5.1 Introduction

Abaqus, commercially available FE software, was used to numerically simulate the geocell-reinforced sections under APT tests. Material properties obtained from testing and actual geometry and boundary conditions were used in the numerical simulation models developed in this study. Unfortunately, 2-D models cannot account for 3-D effects of geocells. Due to the high cost of APT testing, validation by numerical modeling increases the reliability of future analysis with less cost.

5.2 Numerical Simulations

Two different types of numerical simulations were done. The first simulation evaluated the vertical pressure on the subgrade and the geocell strain response during APT tests. Rutting in the HMA layer was evaluated in the second simulation.

5.2.1 Material Properties

Material properties were determined from laboratory and in-situ tests. In the first simulation, the base material was modeled with Mohr-Coulomb plasticity. HMA layers were considered as linear elastic. Geocells were modeled as elastic materials since no damage to the geocells was observed during testing. Material properties used are tabulated in Table 5-2 Material properties used in first numerical simulation. Geocells were modeled as diamonds to simplify meshing while maintaining basic reinforcing functionality. Yang (2010) and Leshchinsky and Ling (2012) successfully modeled multiple geocells as diamonds. In the first simulation Abaqus/Explicit was used, which handles highly nonlinear behavior of materials better than Abaqus/Standard (Implicit) analysis. Abaqus/Standard has convergence issues and uses very small time increments in soil analysis due to yielding of the soil (Abaqus 2012). The base material in this study had cohesion less than 10% of the applied load. However, the creep material model is not available in Abaqus/Explicit; therefore, the HMA layer was modeled as a linear elastic material.

In the second simulation, where Abaqus/Standard was used, the base material was modeled as linear elastic. HMA layers were considered viscoelastic. Similar to the first test, the

geocells were modeled as elastic materials. Creep tests were conducted on the HMA and subgrade materials. Abaqus uses the creep model presented in Equations (2-29) and (2-30). Creep results are presented in Table 5-1. When rut simulations were conducted with properties obtained from the test data, the results were not within reasonable limits of the observed results. A shallow U-shaped rut profile emerged, as shown in Figure 5-1. A W-shaped rut profile, obtained with a transverse profiler, was developed by calibrating the material properties. Results showed that using one-half of the HMA modulus with creep parameters of 1.00E-04, 0.47, and -0.5 and one-third of the base modulus resulted in results that are similar to that are somewhat expected. A reason for the decrease in modulus is that the Kenlayer software could overestimate the moduli. The material properties used in simulation used are tabulated in Table 5-2 and Table 5-3.

Table 5-1 HMA creep test results

	A	m	N
HMA Sample 1	1.10E-09	-0.764	0.97191
HMA Sample 2	1.0E-09	-0.8277	0.96279
HMA Sample 3	1.00E-09	-0.709	0.93499
Subgrade Average	5.26E-05	-0.58	0.6

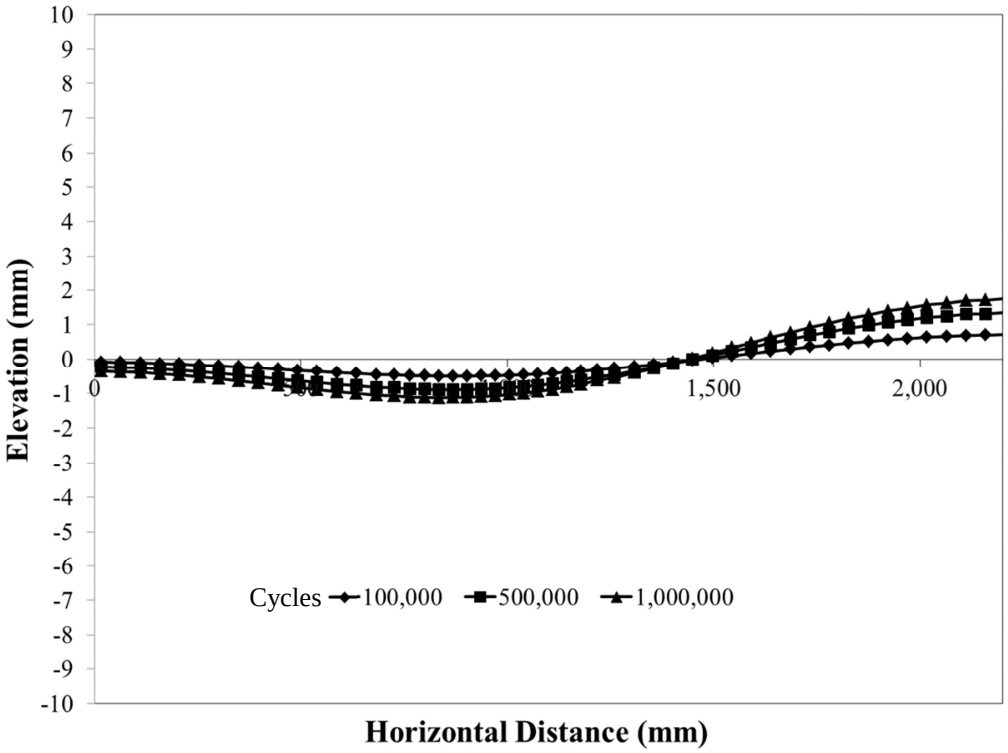

Figure 5-1 Simulated U-shaped rut profile

Table 5-2 Material properties used in first numerical simulation

Material	Lane	Con-trol	Con-trol	Con-trol	QW	QW	QW	RAP	RAP	RAP	AB3	AB3	AB3
	Test #	**1**	**OL**	**2**	**1**	**OL**	**2**	**1**	**OL**	**2**	**1**	**OL**	**2**
Subgrade	**Density (tonne/mm^3)**	1.52E-06	1.52E-06	1.56E-06	1.52E-06	1.52E-06	1.56E-06	1.52E-06	1.52E-06	1.56E-06	1.52E-06	1.52E-06	1.56E-06
	E (MPa)	64	64	68	39	39	52	43	43	58	45	45	59
	v	0.45	0.45	0.45	0.45	0.45	0.45	0.45	0.45	0.45	0.45	0.45	0.45
	Friction Angle	0	0	0	0	0	0	0	0	0	0	0	0
	Dilation Angle	0	0	0	0	0	0	0	0	0	0	0	0
	Cohesion (MPa)	0.104	0.104	0.104	0.104	0.104	0.104	0.104	0.104	0.104	0.104	0.104	0.104
Base	**Density (tonne/mm^3)**	2.03E-06	2.03E-06	2.03E-06	1.95E-06	1.95E-06	1.95E-06	1.78E-06	1.78E-06	1.81E-06	2.03E-06	2.03E-06	1.97E-06
	E (MPa)	115	115	308	43	43	328	34	34	140	35	35	193
	v	0.4	0.4	0.4	0.4	0.4	0.4	0.4	0.4	0.4	0.4	0.4	0.4
	Friction Angle	47.2	47.2	47.2	47.2	47.2	47.2	37	37	37	47.2	47.2	47.2
	Dilation Angle	17.2	17.2	17.2	17.2	17.2	17.2	7	7	7	17.2	17.2	17.2
	Cohesion (MPa)	0.0047	0.0047	0.0047	0.005	0.005	0.005	0.05	0.05	0.05	0.0047	0.0047	0.0047
GC	**E (MPa)**	550	550	550	550	550	550	550	550	550	550	550	550
	v	0.45	0.45	0.45	0.45	0.45	0.45	0.45	0.45	0.45	0.45	0.45	0.45
HMA	**Density (tonne/mm^3)**	2.26E-06	2.26E-06	2.26E-06	2.26E-06	2.26E-06	2.26E-06	2.26E-06	2.26E-06	2.26E-06	2.26E-06	2.26E-06	2.26E-06
	E (MPa)	3954	3954	6468	3083	3083	4867	2165	2165	4947	2154	2154	3848
	v	0.3	0.3	0.3	0.3	0.3	0.3	0.3	0.3	0.3	0.3	0.3	0.3

Table 5-3 Material properties used in second numerical simulation

	Lane	Con-trol	Con-trol	Con-trol	QW	QW	QW	RAP	RAP	RAP	AB3	AB3	AB3
	Test #	1	OL	2	1	OL	2	1	OL	2	1	OL	2
Subgrade	**Density (tonne/mm^3)**	1.52E-06	1.52E-06	1.56E-06	1.52E-06	1.52E-06	1.56E-06	1.52E-06	1.52E-06	1.56E-06	1.52E-06	1.52E-06	1.56E-06
	E (MPa)	64	64	68	39	39	52	43	43	58	45	45	59
	v	0.45	0.45	0.45	0.45	0.45	0.45	0.45	0.45	0.45	0.45	0.45	0.45
	Power Law Multiplier	5.26E-05	5.26E-05	5.26E-05	5.26E-05	5.26E-05	5.26E-05	5.26E-05	5.26E-05	5.26E-05	5.26E-05	5.26E-05	5.26E-05
	Eq Stress Order	0.6	0.6	0.6	0.6	0.6	0.6	0.6	0.6	0.6	0.6	0.6	0.6
	Time Order	-0.58	-0.58	-0.58	-0.58	-0.58	-0.58	-0.58	-0.58	-0.58	-0.58	-0.58	-0.58
Base	**Density (tonne/mm^3)**	2.03E-06	2.03E-06	2.03E-06	1.95E-06	1.95E-06	1.95E-06	1.78E-06	1.78E-06	1.81E-06	2.03E-06	2.03E-06	1.97E-06
	E (MPa)	38	38	102	14	14	109	11	14	47	12	12	64
	v	0.4		0.4	0.4	0.4	0.4	0.4	0.4	0.4	0.4	0.4	0.4
GC	**E (MPa)**	550	550	550	550	550	550	550	550	550	550	550	550
	v	0.45	0.45	0.45	0.45	0.45	0.45	0.45	0.45	0.45	0.45	0.45	0.45
HMA	**Density (tonne/mm^3)**	2.26E-06	2.26E-06	2.26E-06	2.26E-06	2.26E-06	2.26E-06	2.26E-06	2.26E-06	2.26E-06	2.26E-06	2.26E-06	2.26E-06
	E (MPa)	1977	1977	3234	1541	1541	2433	1082	1082	2474	1077	1077	1924
	v	0.3	0.3	0.3	0.3	0.3	0.3	0.3	0.3	0.3	0.3	0.3	0.3
	Power Law Multiplier	1.00E-04	1.00E-04	1.00E-04	1.00E-04	1.00E-04	1.00E-04	1.00E-04	1.00E-04	1.00E-04	1.00E-04	1.00E-04	1.00E-04
	Eq Stress Order	0.47	0.47	0.47	0.47	0.47	0.47	0.47	0.47	0.47	0.47	0.47	0.47
	Time Order	-0.5	-0.5	-0.5	-0.5	-0.5	-0.5	-0.5	-0.5	-0.5	-0.5	-0.5	-0.5

5.2.2 Boundary Conditions

In order to decrease required computational time, only one quarter of the test pit was modeled. Since the pit was surrounded by concrete, displacement was set for the bottom and two sides (back and left) of the model. The left side was restrained from moving in the x direction, and the bottom was restrained from moving in the z direction. The front and right sides used symmetrical boundary conditions. The front used symmetry in the y direction, while the right side used symmetry in the x direction. Symmetry conditions were also included for the geocells as shown in Figure 5-22.

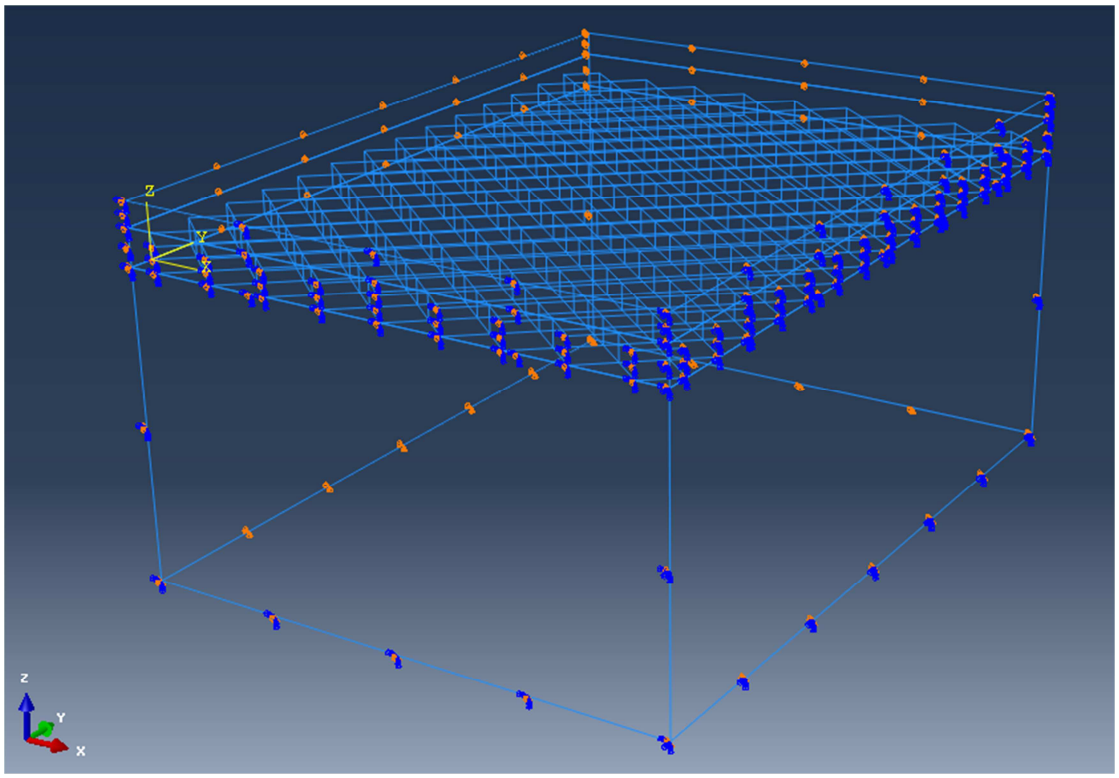

Figure 5-2 Boundary conditions for APT models

5.2.3 Element/Mesh

Solid materials (HMA, base material, and subgrade) were meshed using an 8-noded linear brick, reduced integration hexahedral element (C3D8R). However, a tradeoff was required between accuracy and computational size. Coarser meshes tend to be inaccurate, while finer mesh increases computational time. For simulation of the geocell-reinforced section, a balance

was found with the HMA layer (shown in Figure 5-3), base layer (shown in Figure 5-4), and subgrade (shown in Figure 5-5) with 1,716, 1,449, and 6,279 elements, respectively. Tie constraints were used at the interfaces between the HMA and base material and between the subgrade and base material to help convergence. Geocells were meshed using 10,080 S4R 4-node doubly curved thin or thick shell, reduced integration elements, as shown in Figure 5-6. Shell elements can be used when the ratio of one dimension is higher than the other dimensions (Abaqus 2011).

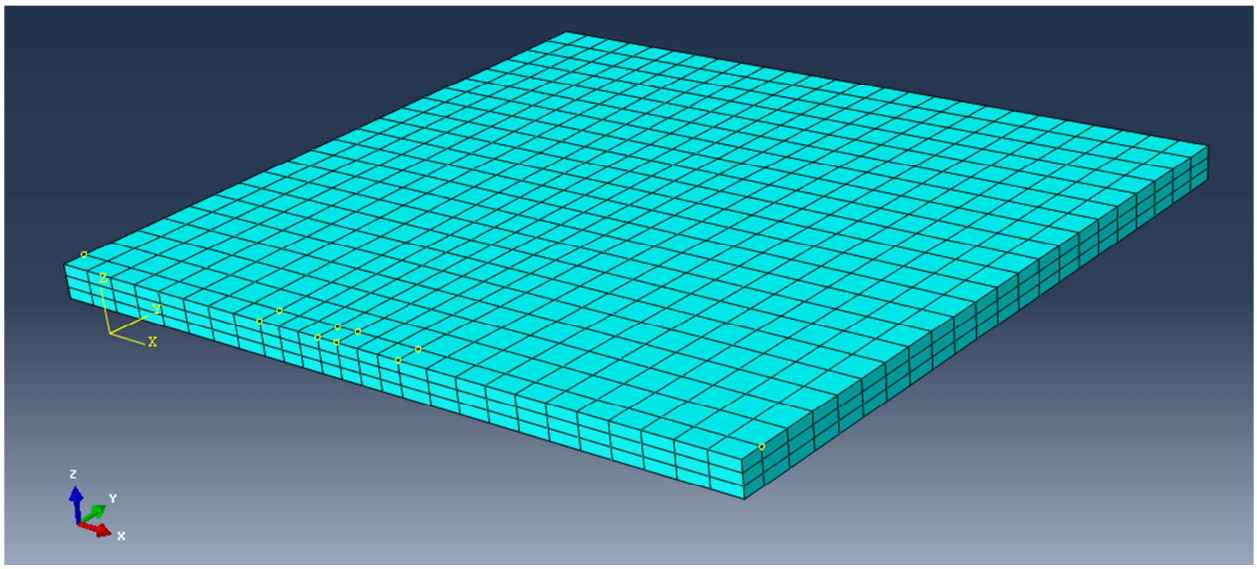

Figure 5-3 HMA mesh

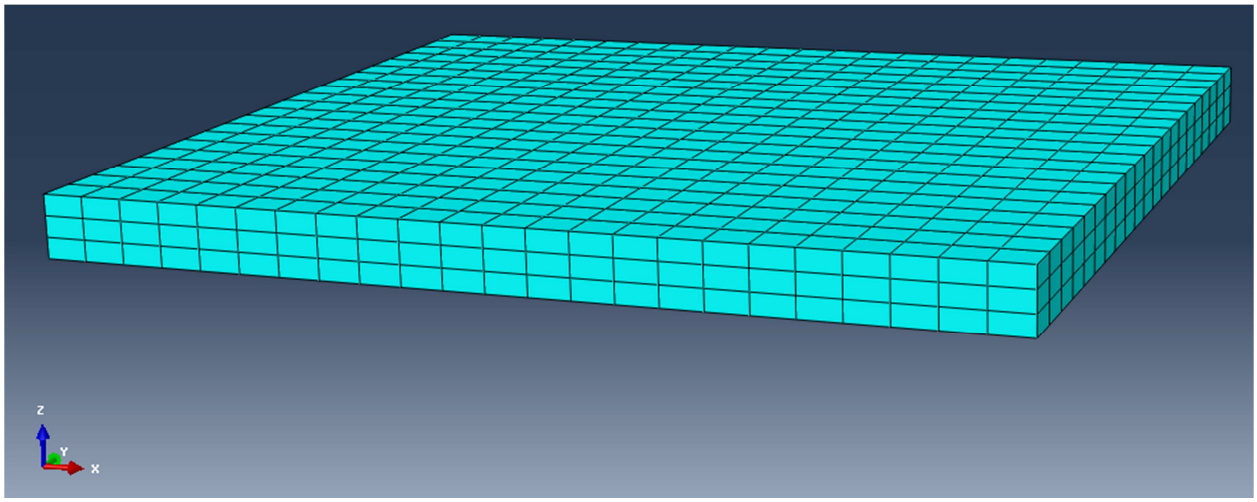

Figure 5-4 Base mesh

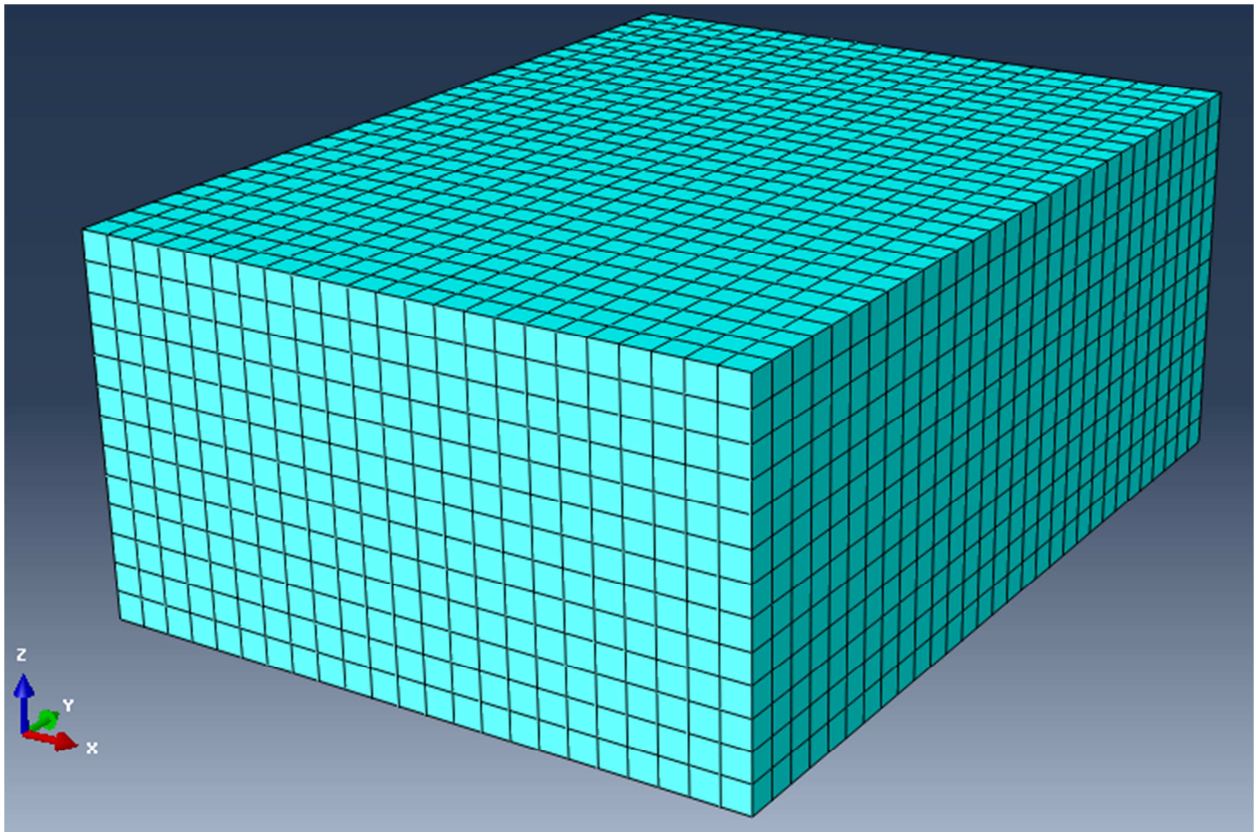

Figure 5-5 Subgrade mesh

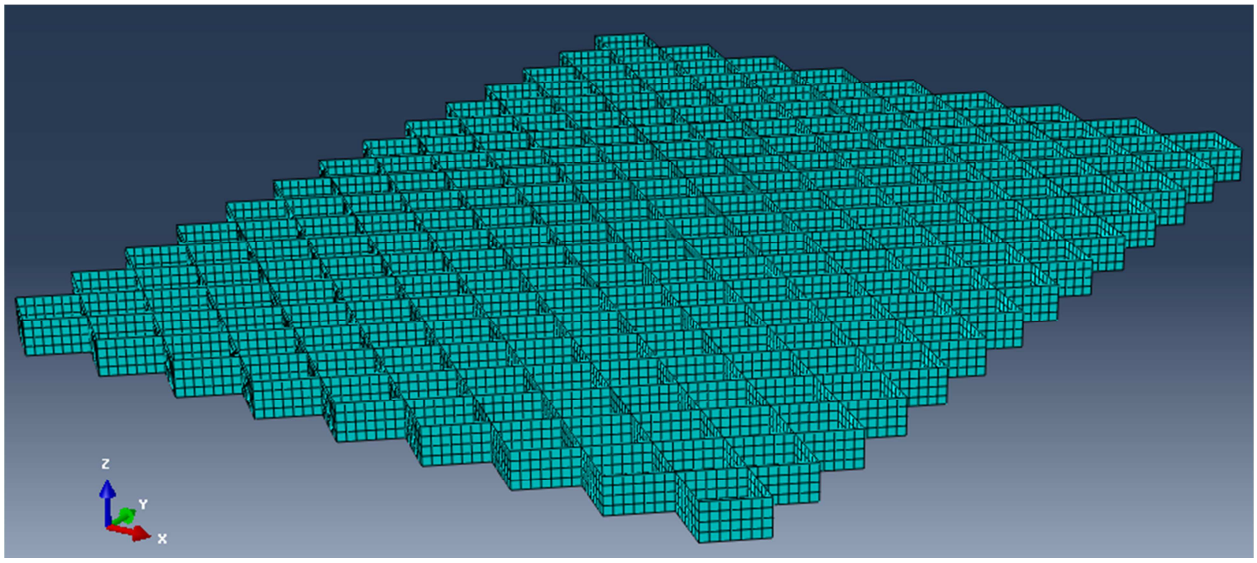

Figure 5-6 Geocell mesh

An embedded region was used to place geocells in the base layer. Embedded regions are a group of elements within a "host" region. The embedded region allows shell elements to be embedded into solid elements, as shown in Figure 5-7. Prevention of infill movement

sandwiched the infill material between the HMA layer and the subgrade. Embedded elements were constrained by the response of the host elements; therefore, no contact friction could be attributed to the geocell wall. However, because the infill had no room to move, the assumption was made that friction between the geocell wall and the infill gave no help or limited help to the reinforcement. This condition differs from the unpaved roads in which the infill has room to move. Infill material in unpaved roads can be pushed out of the cells; therefore, friction is a key factor in developing load resistance in pavement system. The embedded region elements behave in a slab-like motion. The control section was modeled in the FE analysis without embedded geocells.

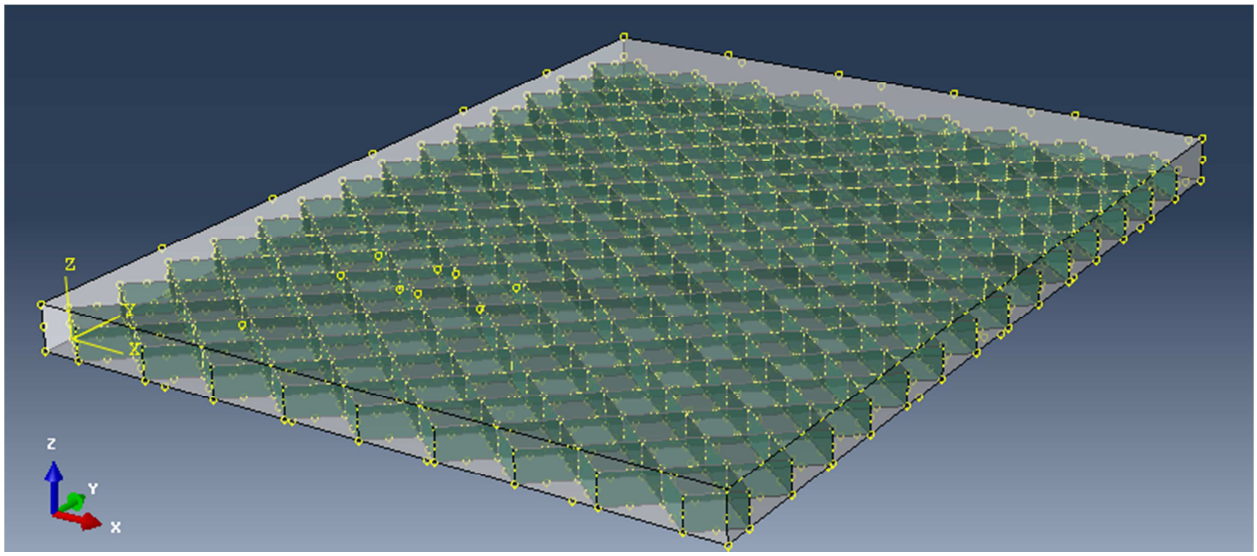

Figure 5-7 Embedded geocells in base layer

5.2.4 Loading

5.2.4.1 Stress and Strain Simulation Loading

Loading of the model occurred over the area of the tire imprint at a given point in the load cycle. Symmetry was used for half of the tire imprint, as shown in Figure 5-8. This type of loading represents results obtained from the sensors. The load was applied as a pressure over an area equal to the tire imprint. The 80-kN (18-kip) total force was applied to the APT loading assembly through two sets of dual tires. A tire pressure of 552 kPa (80 psi) was maintained during testing. Rectangular tire imprints were assumed in this study, resulting in a total tire imprint of 208 mm (8.2 in) wide (measured tire imprint width) by 174.5 mm (6.9 in) long (calculated tire imprint length). The tire imprint length was divided into two loading areas due to

symmetry. One load cycle on a unit tire imprint was calculated to take 0.05 second to pass. The step in the numerical analysis placed a pressure of 552 kPa (80 psi) on the tire imprint for 0.05 second.

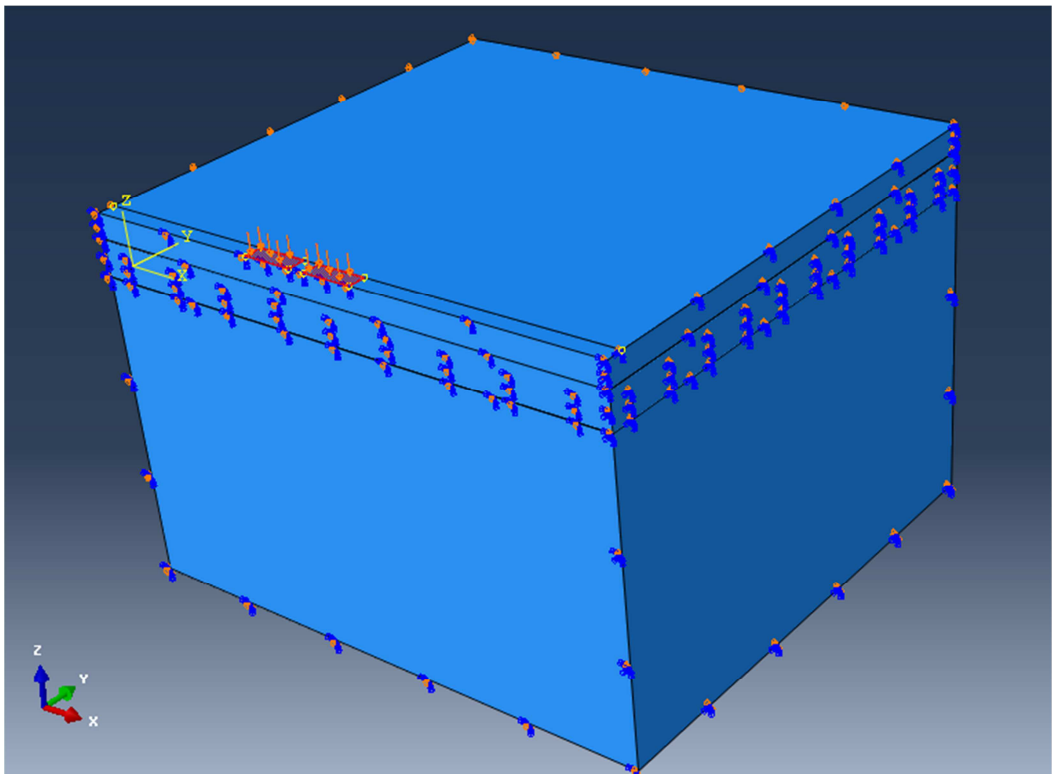

Figure 5-8 Model Loading

5.2.4.2 Rut Simulation Loading

A load pressure of 552 kPa (80 psi) was applied to the tire imprint, as shown in Figure 5-9. Rut depths were taken three times (100,000, 500,000, and 1,000,000 cycles) during the simulation, and seven steps were used to simulate loading. A review of steps is presented in Table 5-4. Lateral wander was not taken into account during rut simulations.

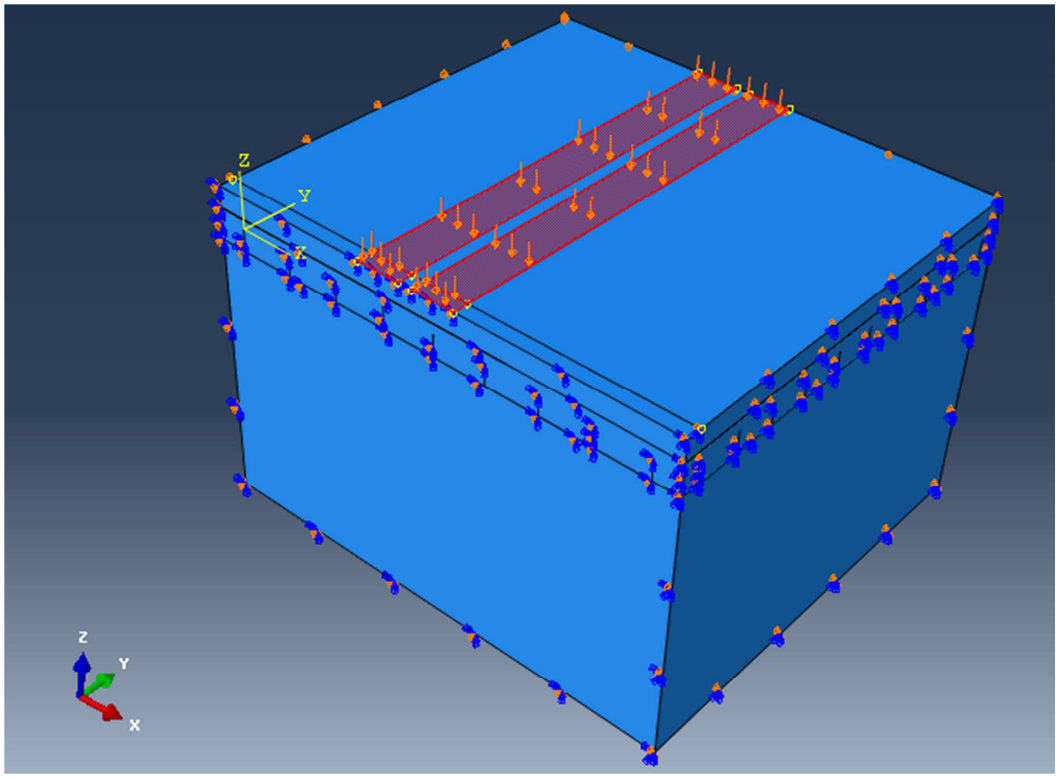

Figure 5-9 Rut simulation loading

Table 5-4 Rut simulation steps

Step	Duration (s)	Loading (kPa)	Comment
Initial	0	0	Setting up of boundary conditions
1	5,000	552	100,000 cycles
2	1	0	First rut depth measurements
3	20,000	552	Total cycles to 500,000
4	1	0	Second rut depth measurements
5	25,000	552	Total cycles to 1,000,000
6	1	0	Third rut depth measurements

Chapter 6 - Results

6.1 APT Test Results

Throughout APT testing, instrumentation was used to record data for one wander cycle at specified load intervals. Vertical pressure on the subgrade, strain at the bottom of the HMA layer, and strain on the body of the geocell were recorded. Transverse profiles were taken at regular intervals in order to measure rut depths.

6.1.1 First Experiment

In the first test, profiles showed dramatic changes in elevation, as shown in Figure 6-1 and Figure 6-2. Heaving, as evident in Figure 6-2, typically corresponds to shear failure of the base and subgrade layers. A high heave area could be due to a localized shear failure in the base or subgrade. In the first set of test sections, the QW section had a localized heaving failure. This failure is believed to have been caused by the subgrade failure. No geocell material was found in the heaved area, and ruts on the control lane did not increase as rapidly as on the geocell-reinforced sections.

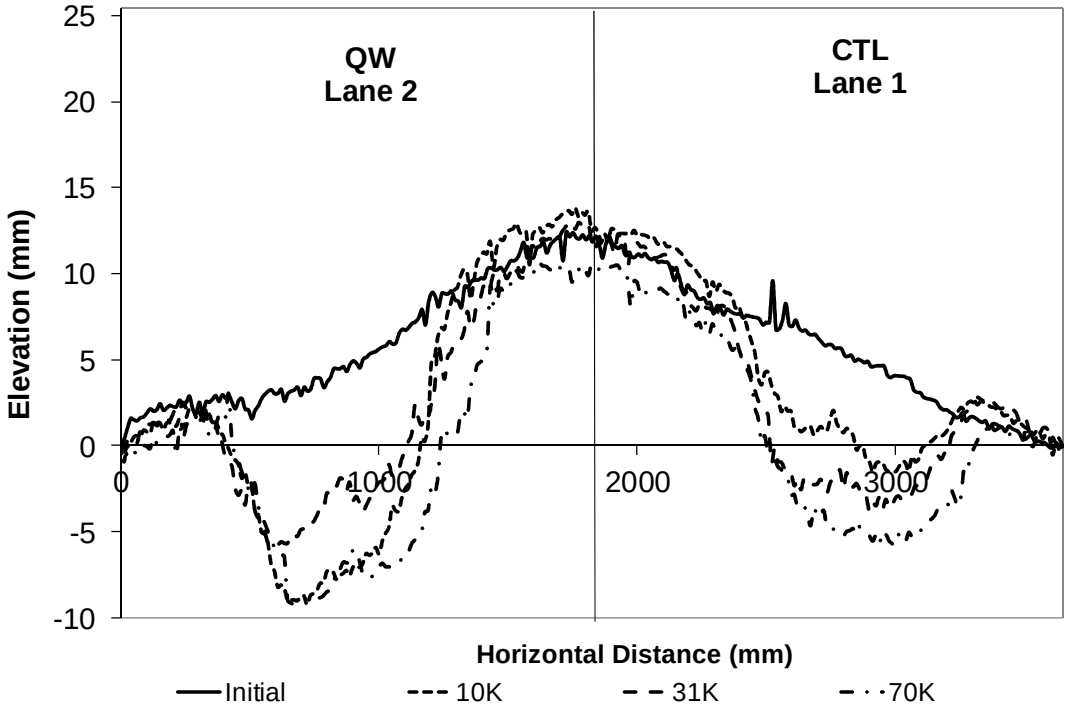

Figure 6-1 Typical middle pit profile first experiment

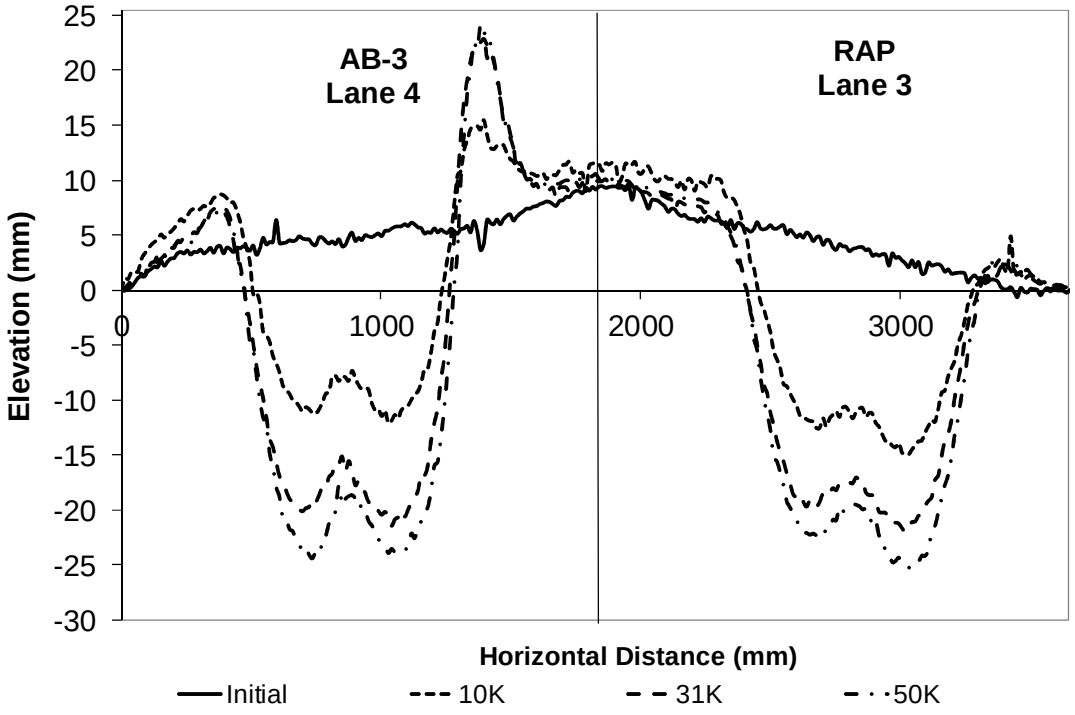

Figure 6-2 Typical south pit profiles first experiment

Vertical pressures on the subgrade, as shown in Figure 6-3 and Figure 6-4, show that all geocell-reinforced sections had higher vertical stress at the top of the subgrade than the control lane. The QW lane showed very high vertical stress in one of the two pressure gauges on that lane. This pressure gauge was located directly below the area that heaved. The pressure was greatly reduced after a steel plate was used to span the failed area. Average vertical pressure readings in the south pit were higher than the 104.6 kPa (15.17 psi) unconfined compressive strength of the subgrade soil.

Many strain gauges on the geocells did not survive construction, as tabulated in Table 6-1. The location of geocell strain gauges in the middle pit was covered with the steel plate; therefore, the strain recorded was not accurate and shown in Table 6-1 Traffic wander induced compression and tension in the geocells. When the geocell strain gauge was located at a distance from the center of the loading, the geocell tended to be under compression while middle geocells were in tension. The RAP lane had the highest peak tensile strain of 3,524 microstrain and the lowest strain (compression) of -1,790 microstrain. The AB-3 lane had the second highest tension and compressive strain, with 2,462 microstrain and -1,254 microstrain, respectively. The QW lane had the lowest tension and compressive strain with 1,403 microstrain and -848 microstrain;

however, the strain was recorded only for the first 676 passes and then the lane heaved, causing the strain readings to no longer be meaningful.

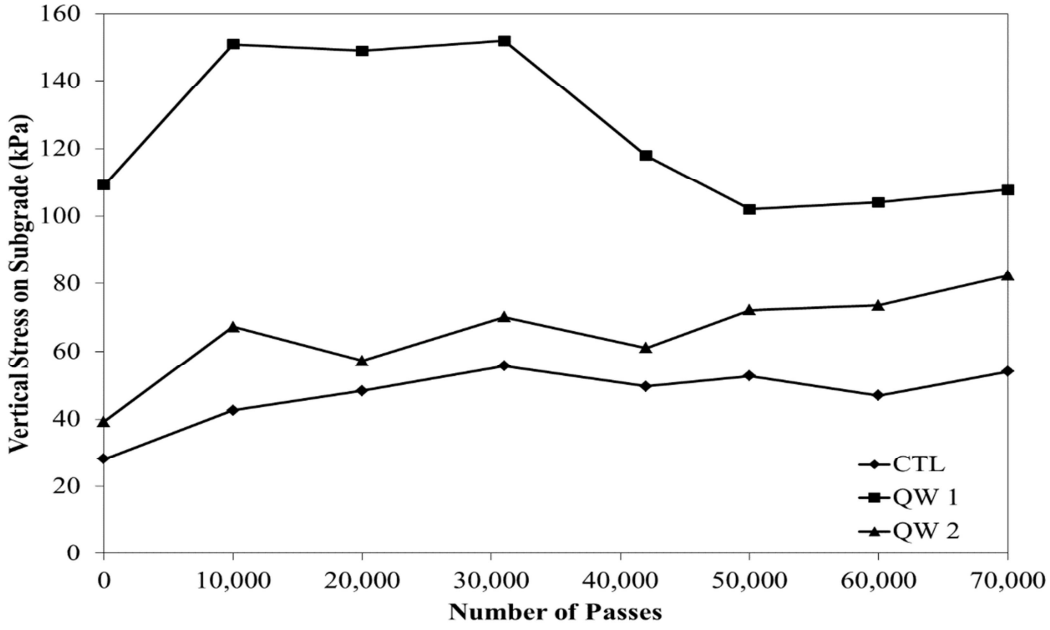

Figure 6-3 Vertical pressure on subgrade of the middle pit during first experiment

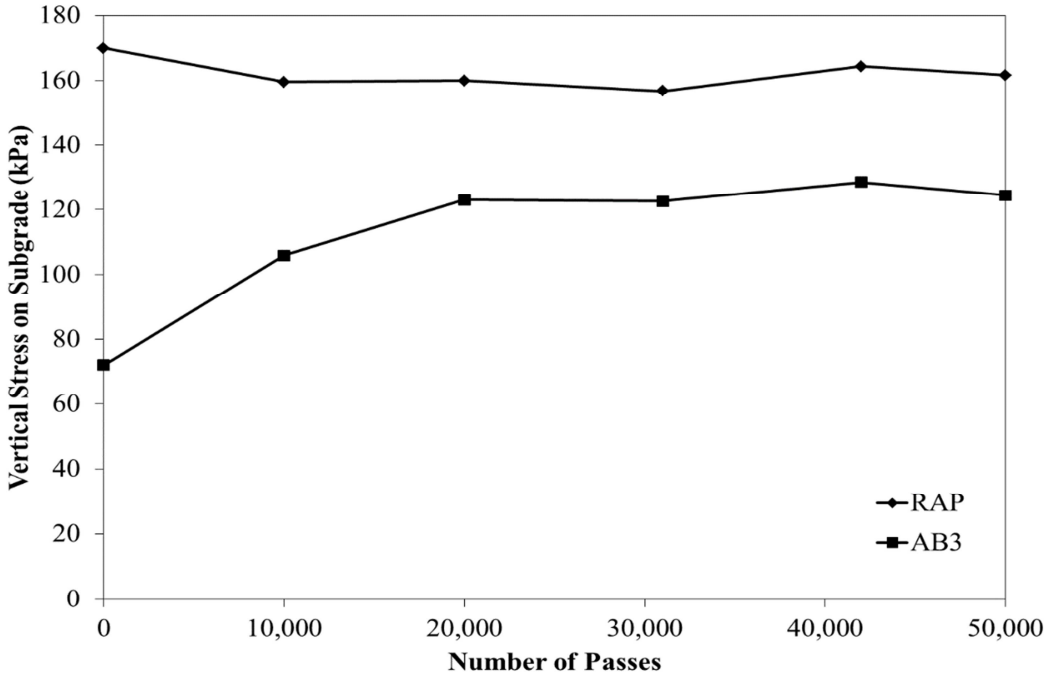

Figure 6-4 Vertical pressure on subgrade in south pit for the first experiment

Table 6-1 Geocell peak horizontal microstrain first experiment (Positive = Tension)

a. Middle Pit (QW Lane)

	Middle Pit				
	S				
Cycle	**1**	**2**	**3**	**4**	**5**
0	-0.000731	-0.000848	0.001403	0.001203	-0.000562
20K					
50K					

b. South Pit (RAP Lane)

	South Pit				
	N				
Cycle	**1**	**2**	**3**	**4**	**5**
0	-0.00179	0.003524		0.003523	
20K	-0.00065				
50K	-0.000677				

c. South Pit (AB-3 Lane)

	South Pit				
	S				
Cycle	**1**	**2**	**3**	**4**	**5**
0	0.000562	0.002252		0.000466	
20K	-0.0009	0.002462		0.00215	
50K	-0.00125	0.00245			

6.1.2 Overlay Experiment

After the overlay, the cross sections with overlays led to rut profiles that did not deteriorate as severely or as quickly, as shown in Figure 6-5 and Figure 6-6. After the overlay was placed, vertical stress was reduced and remained fairly constant during testing as shown in Figure 6-7, and vertical stress in the south pit is shown in Figure 6-8. The south pit had higher vertical stress on the subgrade than the middle pit. This vertical stress was higher than the unconfined compressive strength of the subgrade soil. Although the overlay led to improved performance than earlier, the APT machine was not designed to test pavements with such high elevations. After several major breakdowns, the decision was made to discontinue testing.

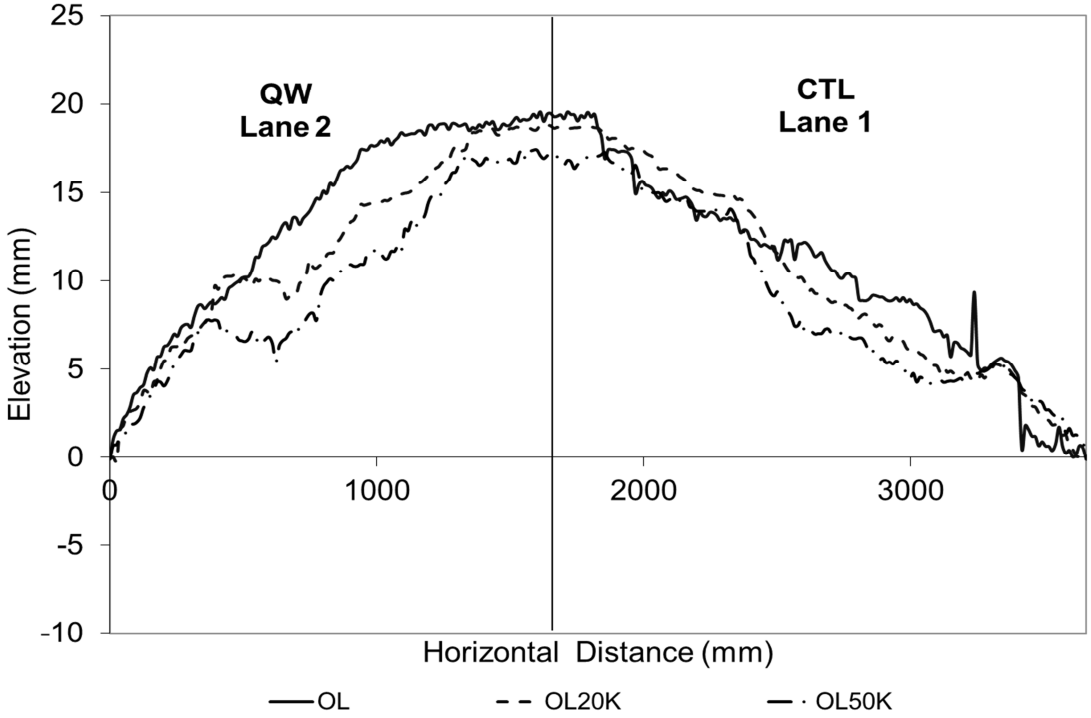

Figure 6-5 Typical middle pit profile profile after overlay

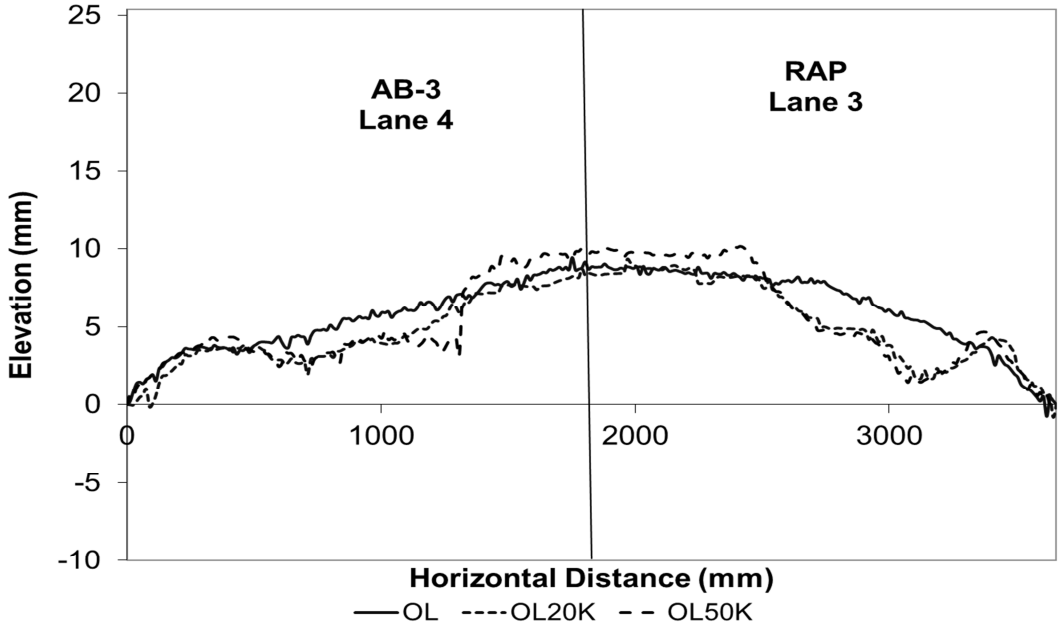

Figure 6-6 Typical south pit profile after overlay

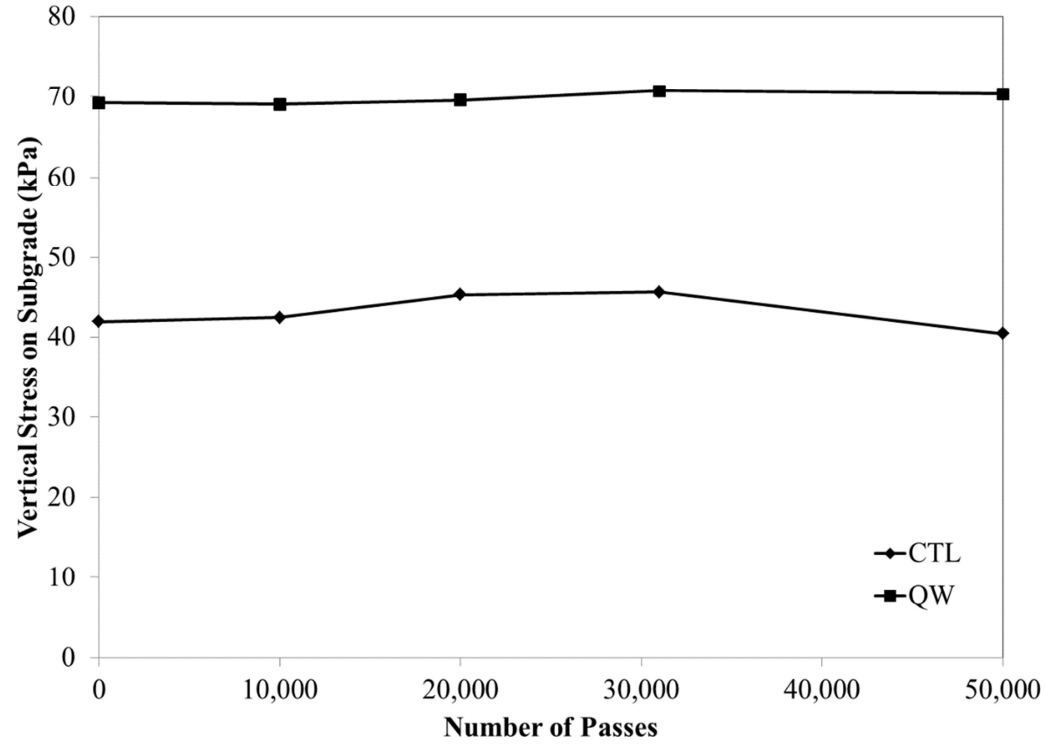

Figure 6-7 Vertical pressure on subgrade of middle pit in overlay experiment

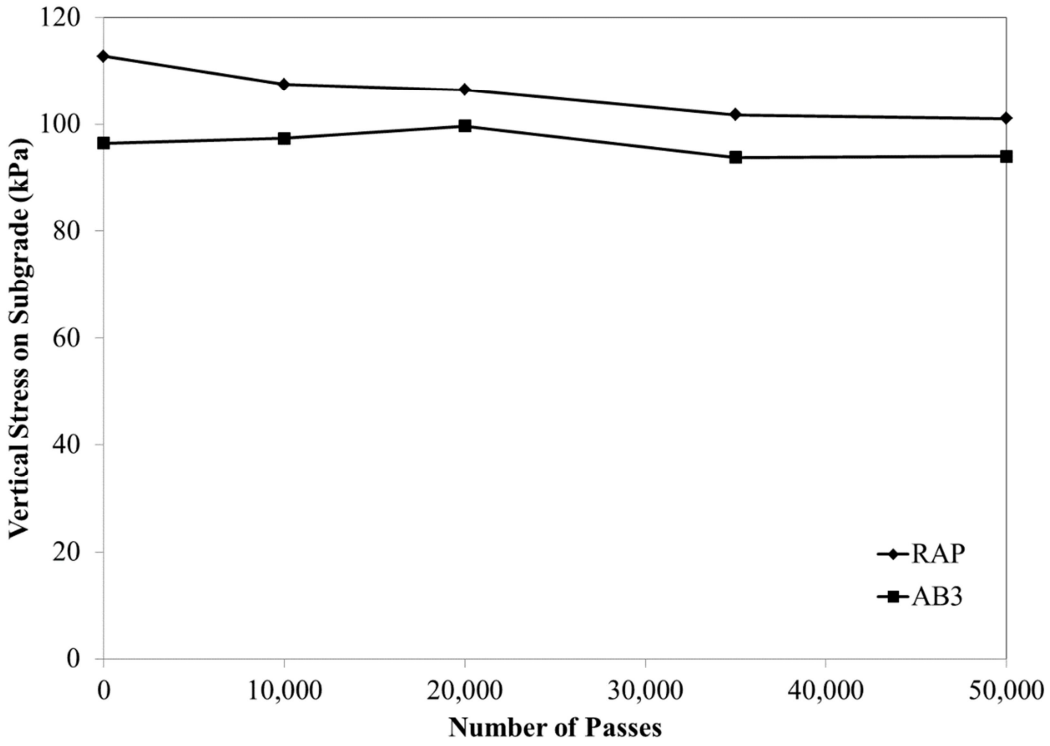

Figure 6-8 Vertical pressure on subgrade of south pit in overlay experiment

Strain results showed that the RAP lane had higher compressive strain than the AB-3 lane, as shown in

Table 6-2 Geocell peak horizontal microstrain overlay experiment (Positive = Tension). Strain in the geocells decreased when the overlay was placed, as exhibited by tensile strain in the AB-3 lane. The strain value decreased from 2,462 microstrain in the first experiment to 1,812 microstrain after the overlay. The thicker HMA section helped reduce strain in the body of the geocells.

Table 6-2 Geocell peak horizontal microstrain overlay experiment (Positive = Tension)

a. South Pit (RAP Lane)

	South Pit				
	N				
Cycle	**1**	**2**	**3**	**4**	**5**
0	-0.000837				
20K	-0.000505				
50K					

b. South Pit (AB3 Lane)

	South Pit				
	S				
Cycle	**1**	**2**	**3**	**4**	**5**
0	-0.000442	0.001812			
20K	-0.000338	0.001760			
50K	-0.000897	0.002462			

6.1.3 Second Experiment

Subgrade protection provided by the thicker cross sections in the second test led to a longer pavement life and lower rut depth, as shown in Figure 6-9 and Figure 6-10. Vertical stress on the subgrade was well below the unconfined compressive strength of the subgrade soil. Figure 6-11 and Figure 6-12 show that as the test progressed, vertical pressure increased; however, this phenomenon began to occur well after the initial test termination point of 500,000 passes, at which point all test sections began to fail. The measured rut depths lent support to this situation because the rut depths increased rapidly after 500,000 passes.

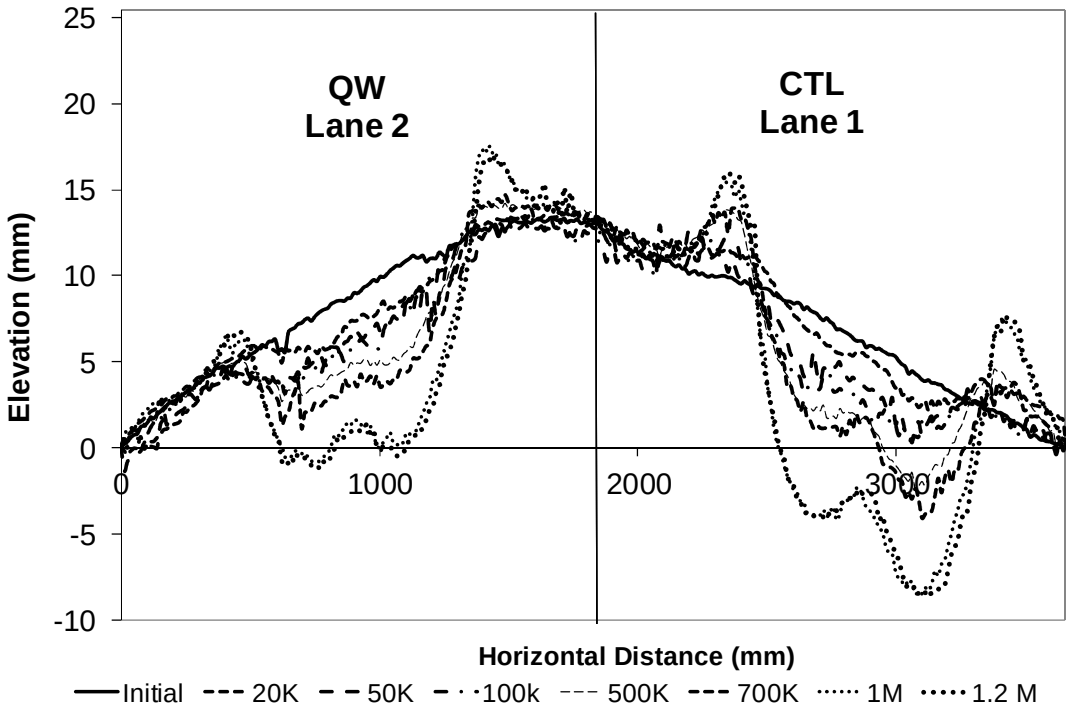

Figure 6-9 Middle pit profiles in second experiment

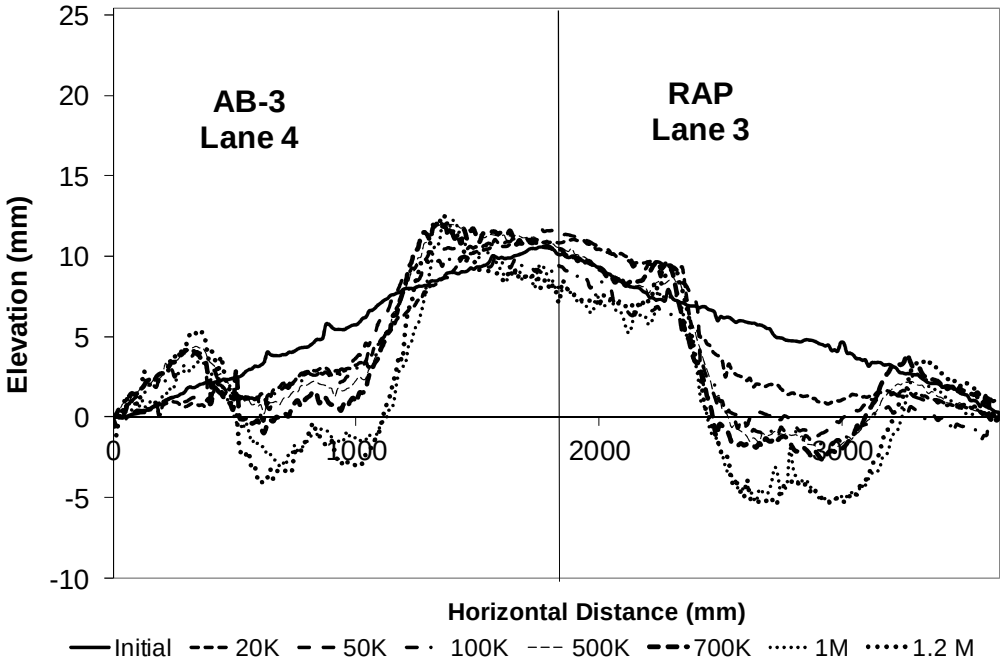

Figure 6-10 South pit profiles second experiment

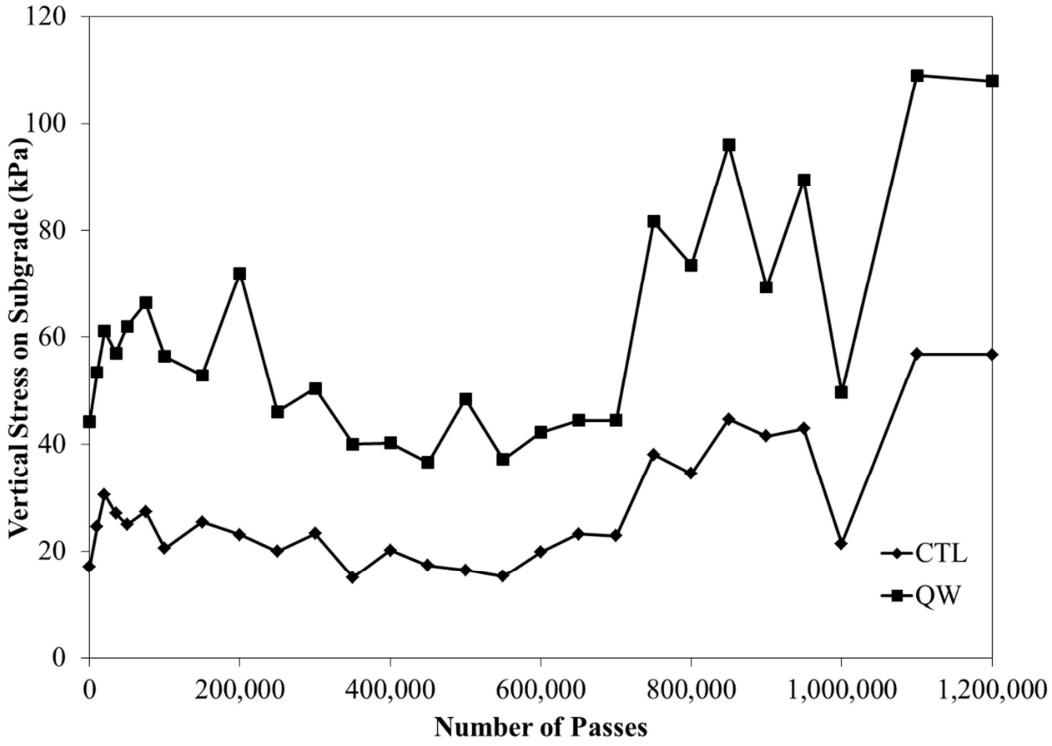

Figure 6-11 Vertical pressure on subgrade of middle pit in second experiment

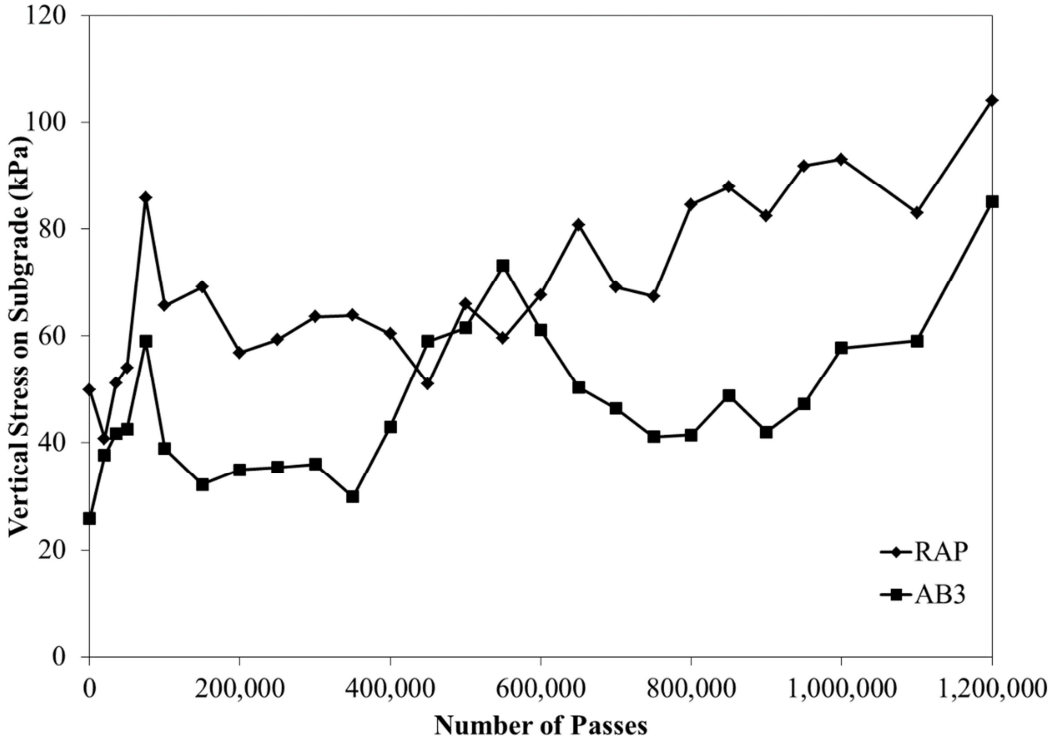

Figure 6-12 Vertical pressure on subgrade of south pit in second experiment

Geocell strain gauges showed that the RAP lane had higher tensile and compressive strains (maximum of 772 microstrain and minimum of -512 microstrain) than the QW (maximum of 477 microstrain and minimum of -254 microstrain) and AB-3 (maximum of 440 microstrain and minimum of -195 microstrain) lanes, as shown in Table 6-3. However, all these strain levels were smaller than the first and overlay experiments.

Table 6-3 Geocell peak horizontal strain second experiment (Positive = Tension)

a. Middle Pit (QW lane)

	Middle Pit				
	S				
Cycle	**1**	**2**	**3**	**4**	**5**
0	0.000263	0.000365	0.000459	-0.000254	-0.000140
20K	0.000260	0.000373	0.000370	-0.000193	-0.000060
50K	0.000210	0.000288	0.000297	-0.000134	-0.000041
100K	0.000230	0.000233	0.000167	-0.000101	-0.000032
500K	0.000230	0.000343	0.000256	-0.000088	0.000035
1,200K	0.000198	0.000477		-0.000250	

b. South Pit (RAP lane)

	South Pit				
	N				
Cycle	**1**	**2**	**3**	**4**	**5**
0	-0.000175	-0.000512	0.000772	0.000649	
20K	-0.000062	-0.000218	0.000314	0.000369	
50K	-0.000505	-0.000512	0.000772	0.000649	
100K	-0.000066	-0.000256	0.000309	0.000299	
500K	-0.000065	-0.000252	0.000318	0.000267	
1,200K	-0.000034	-0.000271	0.000284	0.000181	

c. South Pit (AB3 Lane)

	South Pit				
	S				
Cycle	**1**	**2**	**3**	**4**	**5**
0	0.000401	0.000440	0.000172		
20K	0.000393	0.000268	0.000172		
50K	0.000401	0.000176	0.000172		
100K	0.000436	0.000291	0.000153		
500K	0.000357	0.000300			
1,200K	0.000400	0.000431			

After the second test was completed, a postmortem examination of the test sections was conducted. The geocells changed from typical sinsudial shapes to diamond shapes, as shown in **Error! Reference source not found.**. However, damage to the geocells, as seen in the figures, was caused by a pick used to chip through the base layer. The geocell-reinforced AB-3 base layer was very compact and able to hold its shape after extruding the geocells from the base layer, as shown in Figure 6-14. The QW section showed similar compacted shape retention. During coring of the HMA in the RAP lane, up to 50 mm (2 in.) of RAP was bonded to the HMA layer. Highly compacted base materials behaved like a slab instead of individual cells.

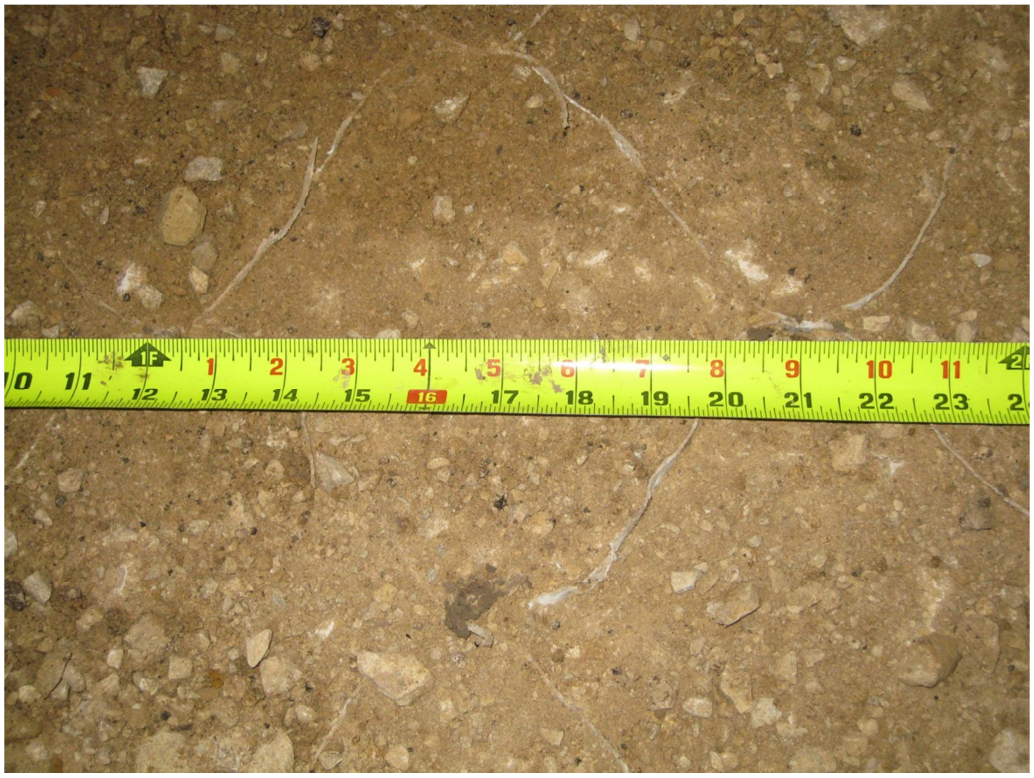

Figure 6-13 AB-3 postmortem after 2nd test

Figure 6-14 AB-3 material after 2nd test

6.1.3 Comparison of First and Second Experiment

Rut depths from the eight sections under this study are compared in Figure 6-15 and Figure 6-16. Thicker cross sections reduced rut depths, rate of rut depth formation, and applied vertical pressure on the subgrade, as shown in Figure 6-17. Pressure on the subgrade was reduced by 43% for the control lane, 40% for the QW lane, 71% for the RAP lane, and 69% for the AB-3 lane after the first 50,000 passes. Strain in the geocells reduced comparably, as shown in Figure 6-18. The QW, RAP, and AB-3 lanes were reduced 68%, 75%, and 83%, respectively. Thicker sections were stronger and had performed better in rutting i.e. they exhibited lower rut depth.

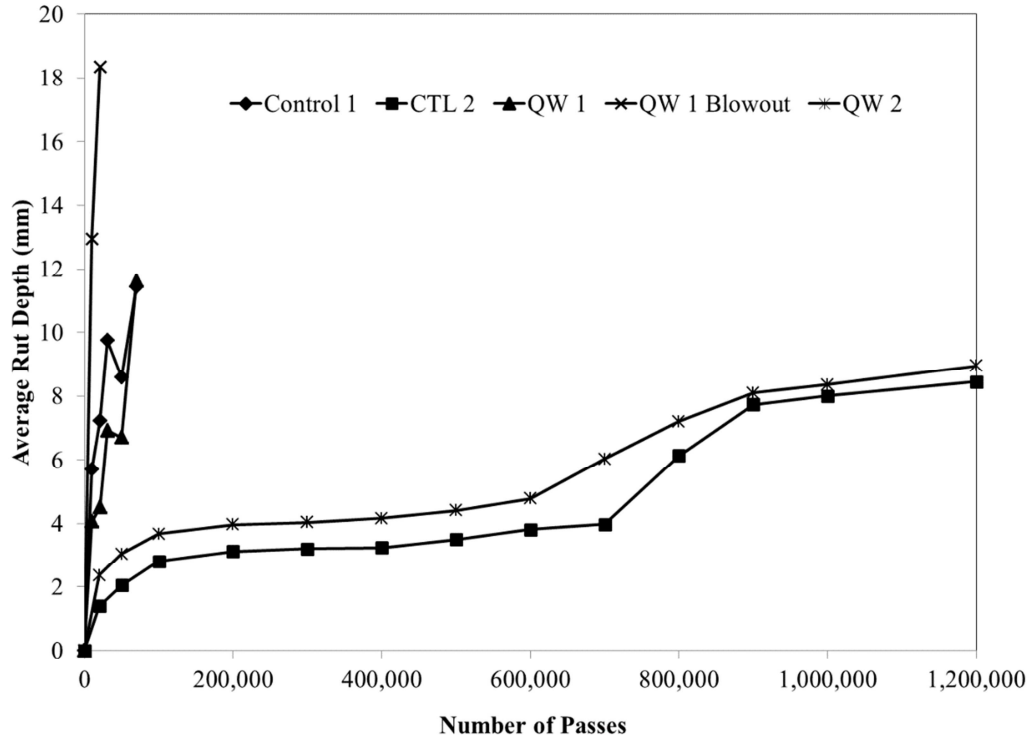

Figure 6-15 Rut depth comparison for middle pit

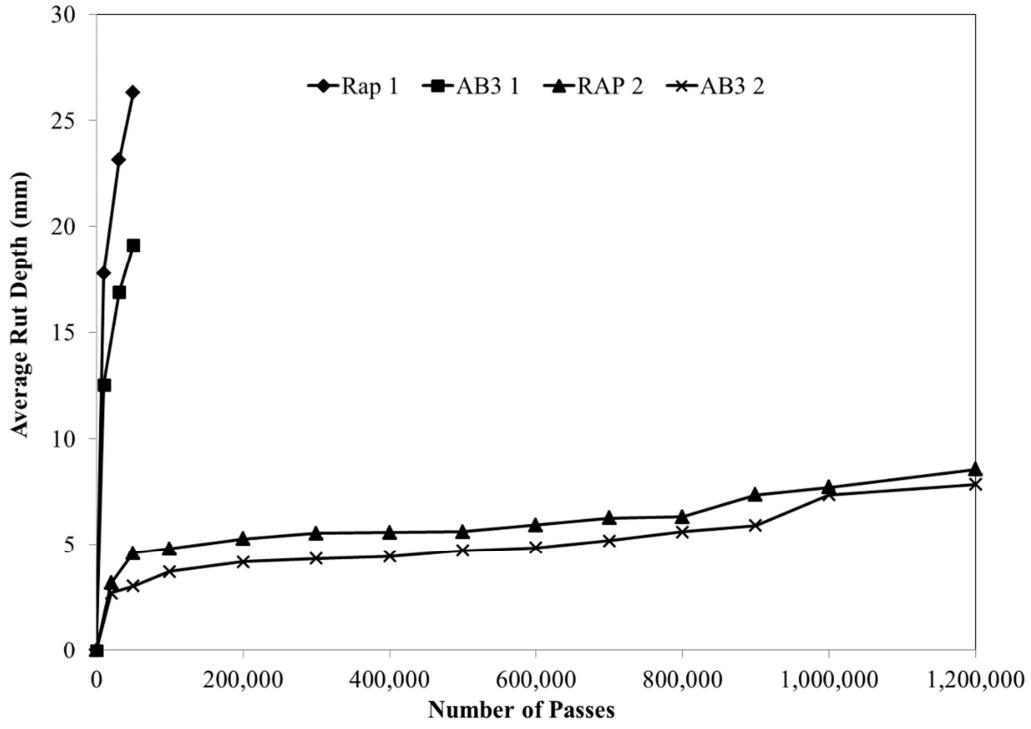

Figure 6-16 Rut depth comparison for south pit

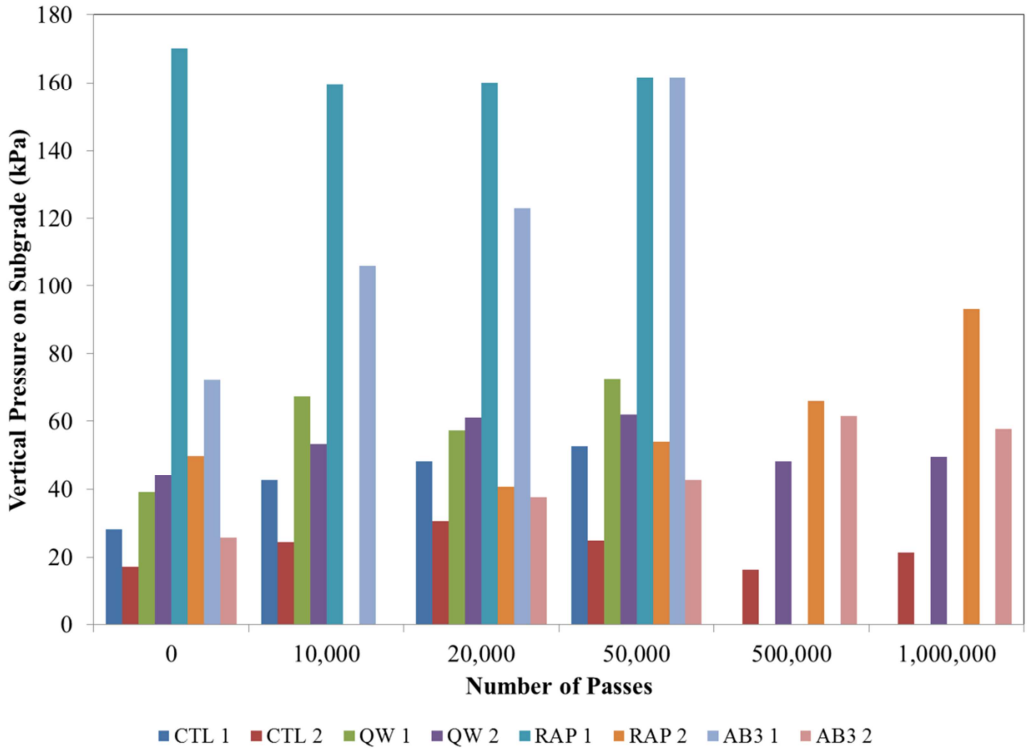

Figure 6-17 Vertical pressure on subgrade comparison

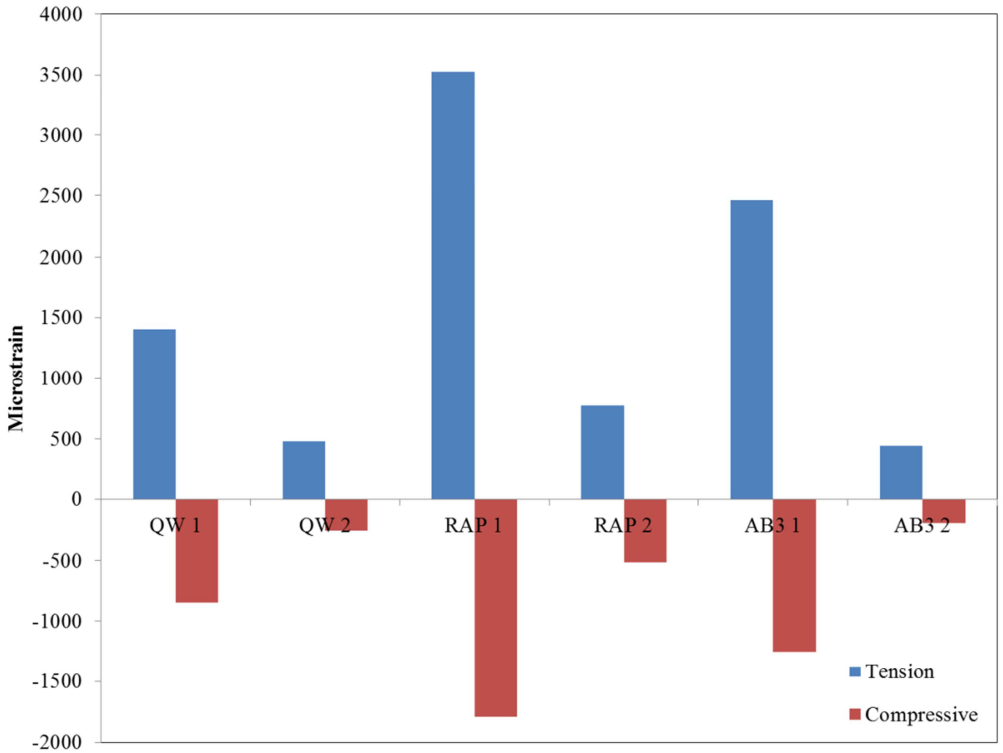

Figure 6-18 Geocell strain comparison

6.2 Layered Elastic (KENLAYER) Analysis

KENLAYER is a computer program that solves for responses of a multilayer elastic system under a circular loaded area (Huang 2004). The program can be used to predict deflections, stresses, and strains in pavement layers under various loading conditions. KENLAYER was used to predict and compare vertical stress on the subgrade and strain at the bottom of the HMA layer. Backcalculation using FWD data was used to find the moduli of the layers in the test sections. However, KENLAYER does not have the capability to account for 3-D reinforcing elements such as geocells. Predicted responses were compared to measured responses for the first set of data, as shown in Table 6-45 and Table 6-56.

Two pressure cells were placed in each lane. Individual gauge readings for each lane are shown in Table 6-4. KENLAYER predicted higher vertical stress on the subgrade in the first test than the second test. Vertical stress on subgrade for the RAP lane was most significantly underestimated, with an average of 57% underestimation in the first test and 23% in the second test. Sensor 3 on the QW section was directly below the area on the lane that eventually heaved. That sensor showed much higher pressure than its companion gauge in the same lane; suggesting overstressing of the subgrade and possible failure. Differences in individual gauge readings can be attributed to differences in initial compaction of the base layers, thereby inducing variable loading on the pressure cells.

Strain gauges were placed beneath the HMA layer. KENLAYER estimates principal strains at the desired locations. Again, KENLAYER calculated higher strains in the first test compared to the second test. The QW lane strain gauge showed 6,330 microstrain, indicating that the HMA layer was failing quickly. In the second test, KENLAYER predicted stain values closer to the measured values, with all predicted values being within 25% of the measured values.

Table 6-4 KENLAYER vertical pressure results (6.89 kPa = 1 psi)

	Control Lane 1		QW Lane 2		RAP Lane 3		AB3 Lane 4	
	Pressure on Subgrade		Pressure on Subgrade		Pressure on Subgrade		Pressure on Subgrade	
First Test								
KENLAYER (kPa)	58.3		121.7		130.5		132.0	
Sensor	1	2	3	4	1	2	3	4
MEASURED (kPa)	29.5	54.1	130.0	56.6	186.1	222.6	92.5	157.4
% Difference	49.5%	7.3%	-6.8%	53.5%	-42.6%	-70.6%	29.9%	-19.2%
Second Test								
KENLAYER (kPa)	39.9		43.2		52.2		54.1	
Sensor	1	2	3	4	1	2	3	4
MEASURED (kPa)	32.2	22.9	52.8	54.4	46.4	81.3	40.6	38.0
% Difference	19.3%	42.5%	-22.1%	-25.8%	11.0%	-56.0%	25.0%	29.8%

Table 6-5 KENLAYER HMA strain

	Control	QW	RAP	AB3
	Strain (Below HMA)	Strain (Below HMA)	Strain (Below HMA)	Strain (Below HMA)
First Test				
KENLAYER	-0.0003631	-0.0008571	-0.0009215	-0.0009024
MEASURED	-0.000369	-0.00633	-0.000429	-0.000273
% Difference	-1.6%	-638.5%	53.5%	69.85%
Second Test				
KENLAYER	-0.0001626	-0.0001897	-0.0002456	-0.0002535
MEASURED	-0.00014	-0.000146	-0.000209	-0.00022
% Difference	13.9%	23.0%	14.9%	13.2%

6.3 Numerical Analysis Results

6.3.1 Response Comparison

6.3.1.1 Stress and Strain Numerical Analysis

Results for various simulations are shown in Table 6-6. During analysis, strain on the geocell was analyzed at two locations. A path was set along five geocells in which strain gauges were located, as shown in Figure 6-19. Maximum and minimum strain values along the path were obtained, and then maximum and minimum strain values on the entire geocell were obtained.

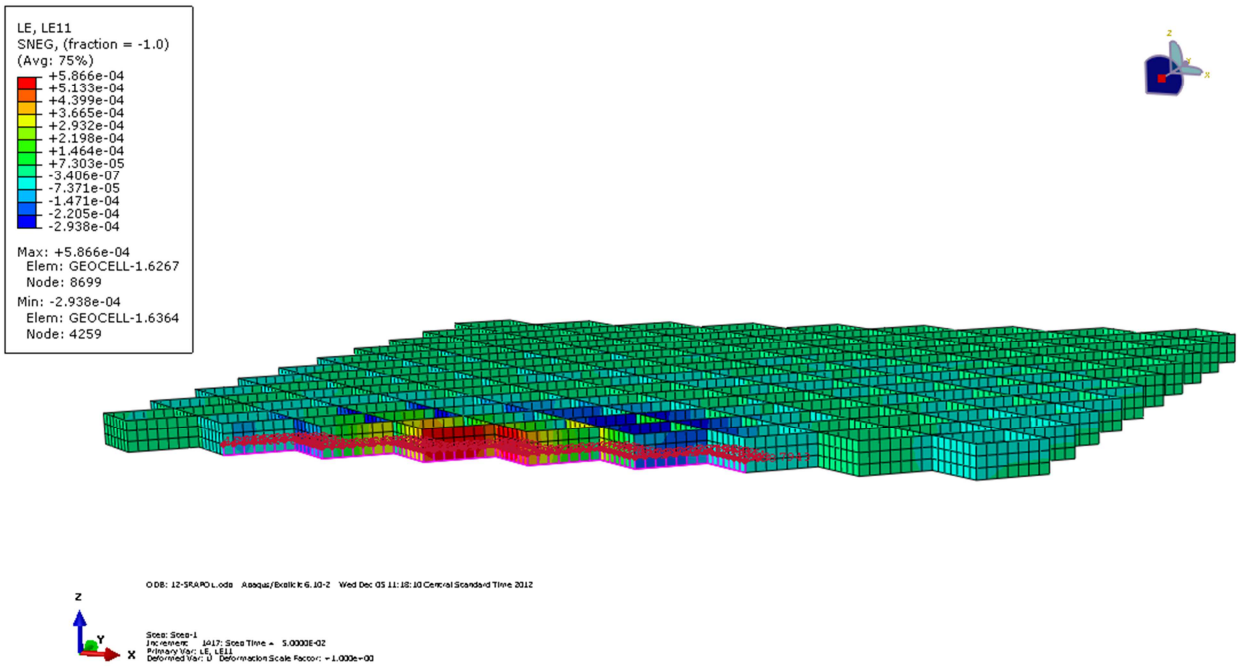

Figure 6-19 Geocell path

Results followed the assumption that thicker and stronger sections would allow less stress to be applied to the subgrade, resulting in lower strain in the geocell and HMA layers. Table 6-7 compares numerical analysis results to measured results. The control lane model results showed close corespondence to the measured strain results, with the highest difference among all three experiments being 11%. However, numerical analysis tended to overpredict HMA strain.

Table 6-6 Numerical response analysis results

Lane	Test #	HMA Strain	GC Path Strain Max	GC Path Strain Min	GC Max Strain	GC Min Strain	Subgrade Stress
		microstrain					kPa
CTL	1	414					92
CTL	OL	250					72
CTL	2	148					28
QW	1	496	803	-271	817	-450	90
QW	OL	328	493	-157	494	-264	70
QW	2	159	313	-57	393	-140	43
RAP	1	651	911	-313	930	-511	119
RAP	OL	441	560	-187	587	-293	91
RAP	2	162	220	-63	328	-180	40
AB3	1	641	870	-299	883	-500	124
AB3	OL	433	531	-182	564	-297	95
AB3	2	186	334	-82	407	-194	41

Table 6-7 HMA strain comparison

	Control	QW	RAP	AB3
	Microstrain (Below HMA)	Microstrain (Below HMA)	Microstrain (Below HMA)	Microstrain (Below HMA)
First Test				
Numerical Analysis	414	496	651	641
MEASURED	369	6330	429	273
% Difference	10.87%	-1176.21%	34.10%	57.41%
Overlay Test				
Numerical Analysis	250	328	441	433
MEASURED	240	-	421	-
% Difference	4.00%	-	4.54%	-
Second Test				
Numerical Analysis	148	159	162	486
MEASURED	140	146	209	220
% Difference	5.41%	8.18%	-29.01%	54.73%

A comparison of subgrade stress results from the numerical analysis and measured values is shown in Table 6-9. These stress results varied depending upon location, possibly due to the construction of the base layer and initial layer compaction because of loading. AB-3 demonstrated unique results, with one sensor measuring response below the predicted value and one sensor measuring response above the predicted value. Numerical analysis underpredicted the subgrade pressure on all RAP sections. Subgrade stress results from numerical simulations of the second set of test sections were closer to the measured strains in all cases with the exception of one sensor in the RAP section.

Table 6-8 Subgrade stress comparison

	Control		**QW**		**RAP**		**AB3**	
	Pressure on Subgrade		**Pressure on Subgrade**		**Pressure on Subgrade**		**Pressure on Subgrade**	
First Test								
Numerical Analysis (kPa)	92.0		90.0		119.0		124.0	
Sensor	1	2	3	4	1	2	3	4
MEASURED (kPa)	29.5	54.1	130.0	56.6	186.1	222.6	92.5	157.4
% Difference	68.0%	41.2%	-44.4%	37.1%	-56.4%	-87.1%	25.4%	-26.9%
Overlay Test								
Numerical Analysis (kPa)	72.0		70.0		91.0		95.0	
Sensor	1	2	3	4	1	2	3	4
MEASURED (kPa)	42.2	41.6	-	47.7	104.3	121.3	87.7	109.1
% Difference	41.4%	42.2%	-	31.9%	-14.6%	-33.3%	7.7%	-14.8%
Second Test								
Numerical Analysis (kPa)	28.0		43.0		40.0		41.0	
Sensor	1	2	3	4	1	2	3	4
MEASURED (kPa)	32.2	22.9	52.8	54.4	46.4	81.3	35.2	48.2
% Difference	-14.9%	18.1%	-22.7%	-26.4%	-16.0%	-103.4%	14.2%	-17.5%

Because numerical simulations were run using Abaqus/Explicit, the HMA layer was modeled as consisting of linear elastic materials; therefore, rutting results could not be extracted from these numerical simulations.

6.3.1.2 Rut Numerical Analysis

The rut numerical analysis did not predict the rapid accumulation of rut depths observed in the first test. The rut profile shape was similar to profiles seen during the APT test. Simulated profiles are presented in Appendix A. Simulations showed a W-shaped profile and heaving at the edge of the tires, similar to the APT test. Differences were observed in material properties, as tabulated in Table 6-9, which shows height of the heave, depth of the rut, and total difference in elevation from heave to rut. Numerical analysis did not show significant rutting in the first 50,000 cycles, so each APT test was simulated to 1,000,000 cycles. Simulation results of the second set of test sections were closer to the measured values in all analyses. Unique results came from the overlay simulation. The overlay simulation demonstrated deeper rutting than the first test simulation in all the base materials. All inputs were being the same as the simulation without overlay, the only difference was a thicker HMA layer.

Table 6-9 Rut depths

		Highest Elevation			Lowest Elevation			Difference in Elevation		
	Cycle	100,000	500,000	1,000,000	100,000	500,000	1,000,000	100,000	500,000	1,000,000
Control	1	0.95	1.86	2.49	-1.71	-2.94	-3.78	2.65	4.80	6.27
	OL	0.90	1.79	2.39	-1.95	-3.33	-4.28	2.85	5.11	6.67
	2	1.11	2.03	2.66	-2.03	-3.47	-4.41	3.14	5.50	7.07
QW	1	1.04	2.04	2.73	-2.59	-4.28	-5.40	3.63	6.32	8.13
	OL	1.01	2.02	2.72	-2.79	-4.68	-5.92	3.80	6.70	8.64
	2	1.04	2.00	2.66	-1.96	-3.55	-4.61	3.00	5.55	7.26
RAP	1	1.03	2.04	2.72	-2.68	-4.45	-5.60	3.71	6.49	8.32
	OL	1.01	2.02	2.72	-2.71	-4.67	-5.98	3.73	6.70	8.70
	2	1.01	1.97	2.64	-2.25	-3.89	-4.99	3.25	5.86	7.63
AB3	1	1.03	2.04	2.72	-2.60	-4.34	-5.48	3.63	6.38	8.20
	OL	1.02	2.03	2.73	-2.63	-4.58	-5.87	3.65	6.61	8.60
	2	1.01	1.98	2.64	-2.01	-3.65	-4.76	3.02	5.63	7.40

Table 6-10 compares results from the second set of APT test sections and numerical analysis results. Numerical analysis underestimated the rut depth by at least 130%. However, when actual rut depth was compared to the difference between the bottom of the rut and the top of the heave obtained from the numerical analysis, results were similar on the south pit (within 1%).

Table 6-10 Rut depth comparison after one million repetitions

	Control	QW	RAP	AB3
	Rut Depth (mm)	Rut Depth (mm)	Rut Depth (mm)	Rut Depth (mm)
Second Test				
Numerical Analysis Rut Depth	3.14	3.00	3.25	3.02
MEASURED	9.12	12.04	7.69	7.34
% Difference	-190.45%	-301.33%	-136.62%	-143.05%
Second Test				
Numerical Analysis Rut Depth + Heave	7.07	7.26	7.63	7.40
MEASURED	9.12	12.04	7.69	7.34
% Difference	-29.00%	-65.84%	-0.79%	0.81%

6.3.2 Parametric Studies of Numerical Simulation

In order to investigate effects of the modulus of the base material and the height of geocells, parametric studies were performed using the FE model. The first simulation study investigated the mechanistic responses in the geocells and the subgrade. HMA rutting was investigated in the second part of the simulation. The modulus of the base material provided insight into the quality of base material and compaction level in the geocells. This analysis used a range of base material elastic modulus, starting from 25 MPa (3,626 psi) to 500 MPa (72,519 psi). In the second study, vertical displacements were measured after 1,000,000 load repetitions.

In the first part of simulation, stronger base material showed a decrease of stress on the subgrade layer up to a point and then continued to level off. Results from this simulation are shown in Figure 6-20. Strain on the geocells increased as the base material modulus increased up to 200 MPa (29,008 psi), and then the strain decreased. Infill material placed in the geocell was shown to significantly impact geocell effectiveness; however, the effect of base material modulus was not profound. In the rutting simulation, when the elastic modulus of the base material exceeded 100 MPa (14,504 psi), HMA displacements leveled out and did not change significantly, as shown in Figure 6-21.

In the geocell height sensitivity analysis, ratios of geocell height, h_{GC}, and two HMA thicknesses ,h_{HMA}, (150 mm [6 in.] and 100 mm [4 in.]), were investigated. In the APT test sections, a 50-mm (2 in.) cover was determined to be the minimum thickness required for

constructability. During this analysis, the height of the base layer was maintained at 50 mm (2 in.) over the height of the geocell. Other parameters in the model were held constant, as shown in Table 6-11.

In the first height study, vertical stress on the subgrade decreased or remained constant as the ratio of geocell height to HMA thickness increased from less than 1 to 2. In both cases, vertical stress on the subgrade increased when the geocell height-to-HMA thickness ratio was greater than 2 and then decreased significantly, as shown in Figure 6-22. Strain in the geocells decreased as this ratio increased, and a decrease in the benefit of reduced strain was observed as the ratio exceeded 2, as shown in Figure 6-23. In the second part of simulation, HMA vertical displacement decreased as the height of the geocell increased, as shown in Figure 6-24. The 150-mm HMA layer consistently had a deeper rut.

Table 6-11 Parametric study material properties

		Subgrade and Geocell Response		Rut Response	
	Study	Base Modulus	Geocell Height	Base Modulus	Geocell Height
Subgrade	Density (tonne/mm^3)	1.52E-06	1.52E-06	1.52E-06	1.52E-06
	E (MPa)	45	45	45	45
	V	0.45	0.45	0.45	0.45
	Friction Angle	0	0		
	Dilation Angle	0	0		
	h (mm)	1274	1274		
	Cohesion (MPa)	0.104	0.104		
	Power Law Multiplier			5.26E-05	5.26E-05
	Eq Stress Order			0.6	0.6
	Time Order			-0.5814	-0.5814
Base	Density (tonne/mm^3)	2.03E-06	2.03E-06	2.03E-06	2.03E-06
	E (MPa)	Variable	150	Variable	100
	V	0.4	0.4	0.4	0.4
	Friction Angle	47.2	47.2		
	Dilation Angle	17.2	17.2		
	h (mm)	150	Geocell height + 50mm	150	Geocell height + 50mm
	Cohesion (MPa)	0.0047	0.0047		
GC	E (MPa)	550	550	550	550
	V	0.45	0.45	0.45	0.45
	h (mm)	100	Variable	100	Variable
HMA	Density (tonne/mm^3)	2.26E-06	2.26E-06	2.26E-06	2.26E-06
	E (MPa)	4000	4000	1500	1500
	V	0.3	0.3	0.3	0.3
	h (mm)	100	100 or 150	100	100 or 150
	Power Law Multiplier			0.0001	0.0001
	Eq. Stress Order			0.47	0.47
	Time Order			-0.5	-0.5

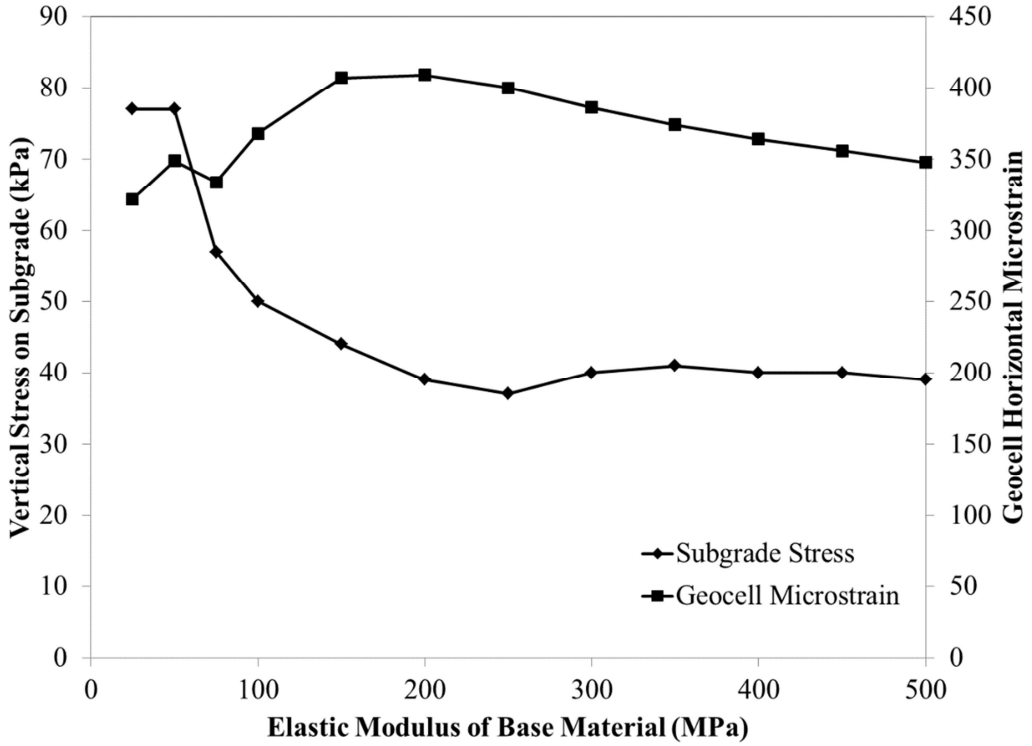

Figure 6-20 Response results for varying base material elastic modulus

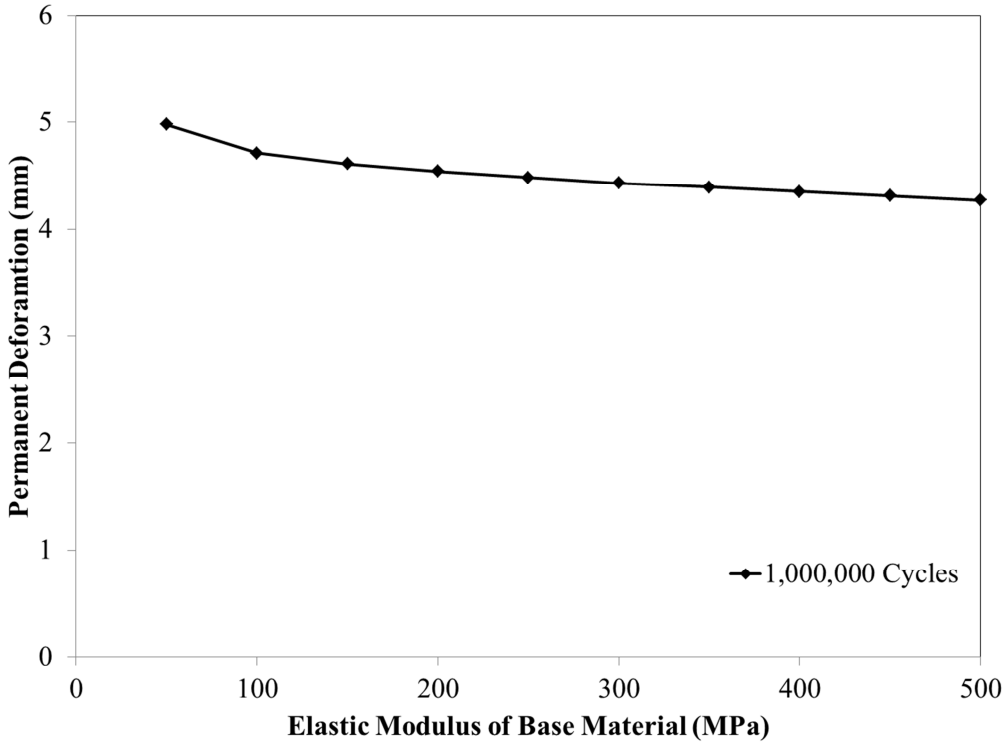

Figure 6-21 HMA vertical displacement for varying base material elastic modulus

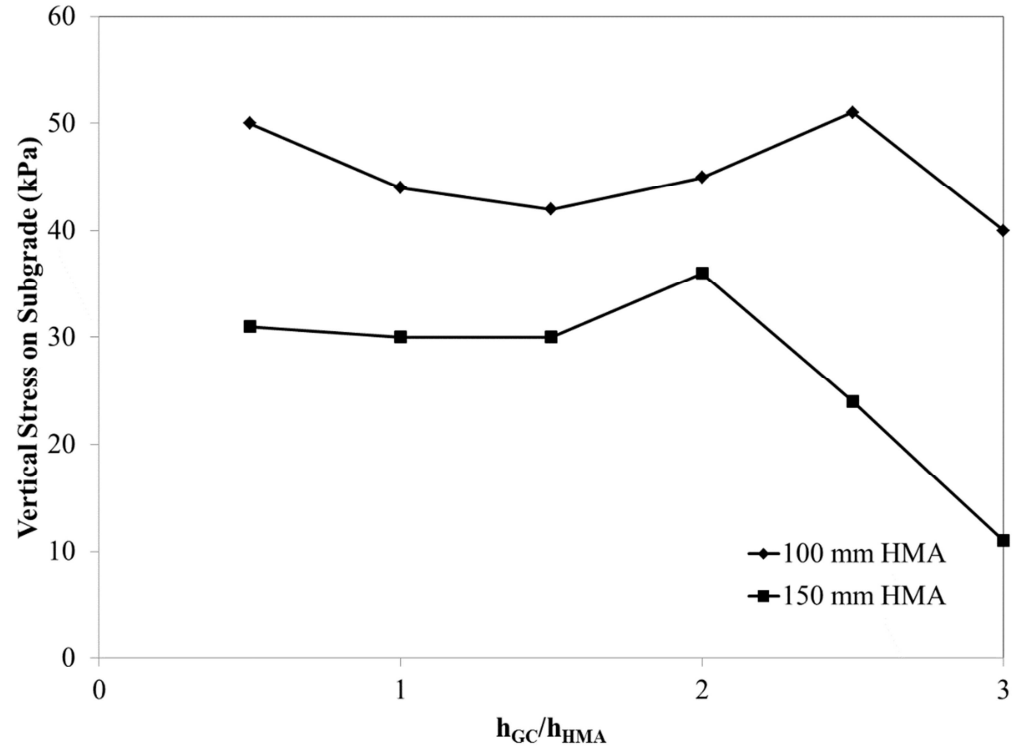

Figure 6-22 Subgrade stress with varying geocell height

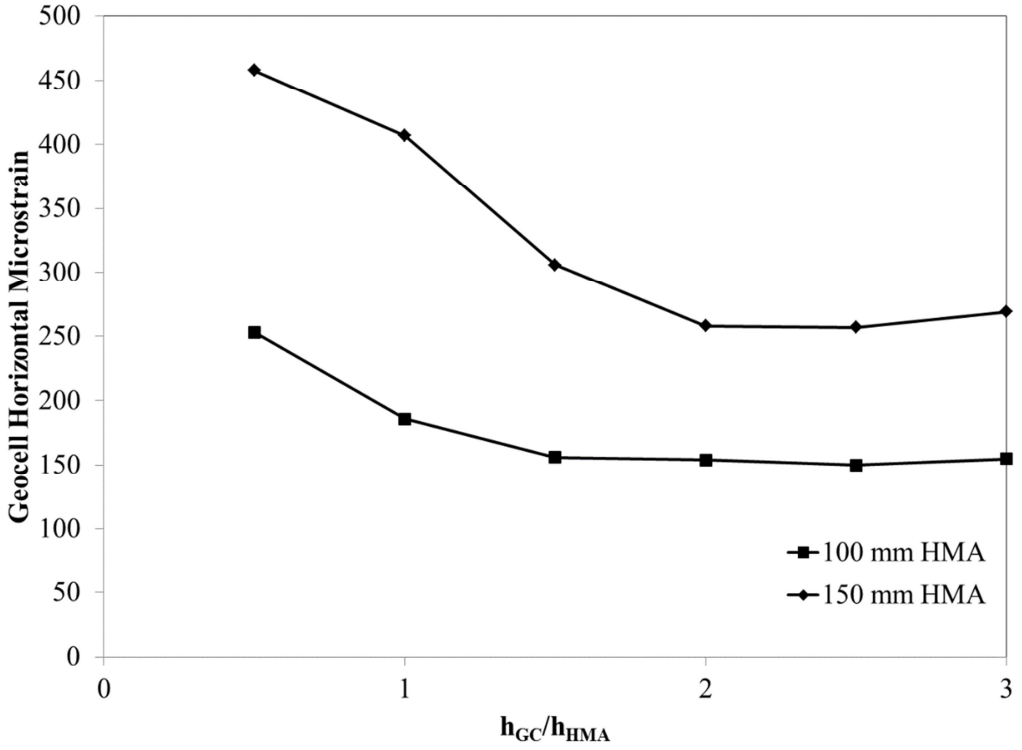

Figure 6-23 Geocell horizontal strain with varying geocell height

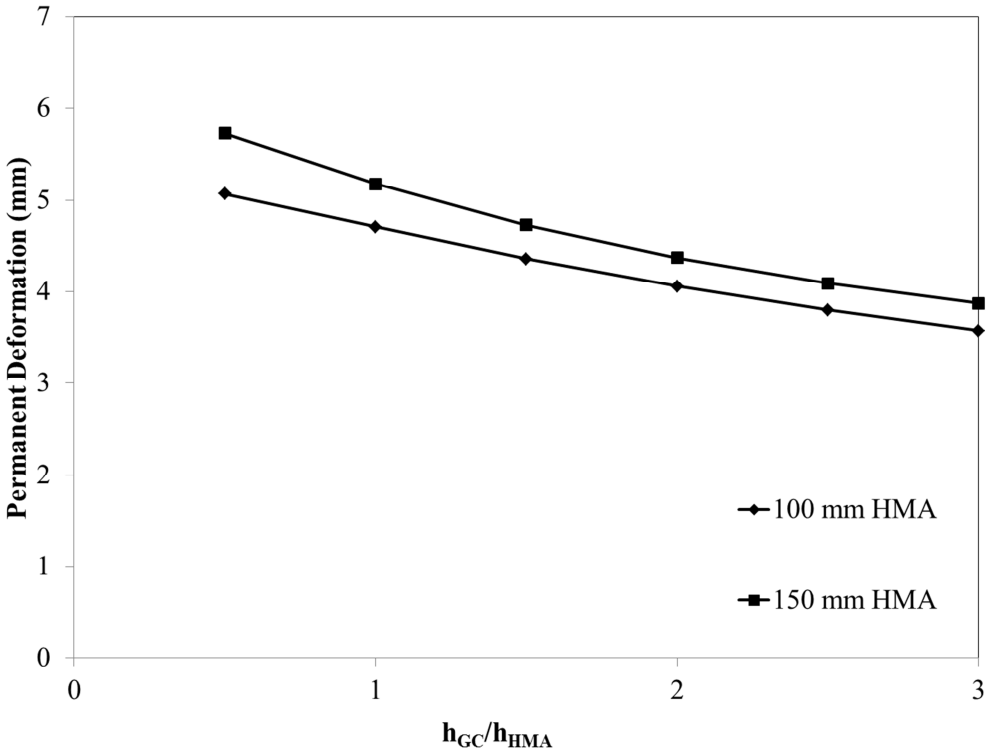

Figure 6-24 HMA vertical permanent deformation for varying geocell height

Chapter 7 - Conclusions, Recommendations & Future Work

In this study, APT was conducted on geocell-reinforced, granular base layers overlaid with HMA. Rut depths, stresses in the subgrade, and strains in the geocells and HMA layers were recorded to study behavior of various infill materials. Experimental data was used to validate the numerical models developed based on the geocell-reinforced pavement sections. Parametric simulations were conducted to evaluate variables in the study.

7.1 Conclusions

Based on this study, the following conclusions can be made for the geocell-reinforced base layers for low-volume paved roads:

1. Under HMA and after initial compaction due to loading, base materials become solidified and begin to behave like a slab instead of individual cells.
2. A 50-mm cover over the geocells ensures higher compaction level of infill materials in the geocells and provides protection to geocells during compaction and HMA placement.
3. A 75-mm thick geocell reinforced base layer approaches maximum capacity of the geocells. A 100-mm thick geocell enhances the load-bearing capacity of the base layer. Taller geocells create more friction to be overcome, thereby increasing bearing capacity. However, numerical analysis showed an increase in vertical subgrade stress when the ratio of height of the geocell to height of the HMA layer approached 2.
4. Lower-quality infill materials can perform as well as high-quality infill materials if adequate height of geocells/base thickness is provided to protect the subgrade from overstressing. Geocells enhance shear strength of lower-quality materials ensuring their usage. Increased quality of the base material increased overall structural stability of the system. However, this benefit diminishes with increasing base modulus.
5. An HMA layer of 50 mm is too thin for the existing legal axle load. Minimum thickness for the HMA layer is recommended to be 100 mm.
6. HMA rutting can be decreased by increasing geocell height. However, HMA rutting has comlex relationships with other factors such as HMA thickness. Level of HMA compaction, etc. that are beyond the scope of this study.

7.2 Recommendations & Future Work

Based on this study, the following recommendations can be made for the geocell-reinforced base layers for low-volume paved roads

1. A minimum of 50-mm cover is required for safe and proper compaction into the geocells.
2. A minimum of 100-mm HMA is required for stability in a geocell reinforced road structure.
3. More study is required to investigate the increase in subgrade vertical pressure as the geocell height ratio increases and then dramatically decreases.
4. Cost studies are needed to determine a breakeven investment for geocell-reinforced pavement structures.

References

AASHTO (2001). Guidelines for geometric design of very low-volume local roads (ADT ≤ 400). American Association of State Highway and Transportation Officials, Washington, D.C.

AASHTO (2008). Mechanistic-empirical pavement design guide, a manual of practice. American Association of State Highway and Transportation Officials, Washington, D.C.

AASHTO TP 79-09 (2009). "Standard method of test for determining the dynamic modulus and flow number for hot mix asphalt (HMA) using the asphalt mixture performance tester (AMPT)," American Association of State Highway and Transportation Officials, Washington, D.C.

AASHTO T 324 (2004). "Standard method of test for Hamburg wheel-track testing of compacted hot-mix-asphalt (HMA)" American Association of State Highway and Transportation Officials, Washington, D.C.

Al-Qadi, I. L., and Hughes, J. J. (2000). "Field evaluation of geocell use in flexible pavements." *Transportation Research Record, No.* 1709, Transportation Research Board, Record, Washington, D.C., pp. 26-35.

Aschenbrener, T., Terrel, R.L., and Zamora, R.A. (1994). "Comparison of the Hamburg wheel-tracking device and the environmental conditioning system to pavements of known stripping performance." *Report No. CDOT-DTD-R-94-1*. Colorado Department of Transportation, Denver, CO.

ASTM D 4439-04 (2004). "Standard terminology for geosynthetics" *ASTM*, Philadelphia, PA.

Bathurst, R.J., and Jarrett, P.M. (1988). "Large-scale model tests of geocomposite mattresses over peat subgrades." *Transportation Research Record*, No.. 1188, Transportation Research Board, Record, Washington, D.C., pp. 28-36.

Bathurst, R.J., and Karpurapu, R.L. (1993). "Large scale triaxial compression testing of geocell reinforced granular soils." *Geotechnical Testing Journal*, Vol. 16, No. 3, pp. 296-303.

Bortz, B.S., Hossain, M., Halami, I., and Gisi, A. (2011). "Innovative uses of quarry waste and reclaimed asphalt pavement." Published in the proceedings of the *International Conference on Sustainable Design and Construction*, Kansas City, Missouri, March.

Boscardin, M.D., Selig, E.T., Lin, R.S., and Yang, G.R. (1990). "Hyperbolic parameters for compacted soils." *Journal of Geotechnical Engineering*. Vol. 116, No. 1. pp.88-104.

Brown, E. R., Kandhal, P., Roberts, F., Kim, Y. R., Lee, D.Y., and Kennedy, T. (2009). Hot mix asphalt materials, mixture design and construction. 3rd edition, *NAPA Research and Education Foundation*, Lanham, Maryland.

Burmister, D. M. (1943). "The theory of stresses and displacements in layered systems and application to the design of airport runways." Proceedings of the *Highway Research Board*, Vol. 23, Highway Research Board, Washington, D.C., pp. 126-144.

Burmister, D. M. (1945). "The general theory of stresses and displacements in layered soil systems I, II, and III." *Journal of Applied Physics*, Vol. 16, pp. 89-94, 126-127, 296-302.

Burmister, D. M. (1958). "Evaluation of pavement systems of the WASHO road test by the layered systems method." *Bulletin 177*, Highway Research Board, Washington, D.C., pp. 26-54.

Button, J.W., Chowdhury, A., and Bhasin, A. (2004). "Design of TXDOT asphalt mixtures using the Superpave gyratory compactor." *Report No. FHWA/TX-05/-4203-1*. Texas Department of Transportation, Austin, TX.

Chang, D.T., Chang, C.H., and Pai S.W., (2007). "Investigation of bearing capacity and dynamic-elastic behavior of mechanical stabilizing of sand subgrade using geocells." Preprint CD-ROM of the *86th Transportation Research Board Annual Meeting*, January 21-25, Washington, D.C.

Chang, D.T., Chang, C.H., Kou, C.H., and Chien T.W. (2008). " Bearing capacity and resilient property studies for sandy soil with confinement of geocells." Preprint CD-ROM of the *87th Transportation Research Board Annual Meeting*, January 13-17, Washington, D.C.

Collins, I.F. Wang, A.P., and Saunders, L.R. (1993). "Shakedown in layered pavements under moving surface loads." *International Journal for Numerical and Analytical Methods in Geotechnics*, Vol. 17, No. 3, pp. 165-174.

Collins, I.F. and Boubibane, M. (2000). "Geomechanical analysis of unbound pavements based on shakedown theory." *Journal of Geotechnical and Geoenviromental Engineering*, Vol. 126, No. 1, pp. 50-59.

Cowland, J.W. and Wong S.C.L (1993). "Performance of road embankment on soft clay supported on a geocell mattress foundation." *Geotextiles and Geomembranes*, Vol. 12 No. 8, pp. 687-705.

Dash, S.K., Rajagopal, K., and Krishnaswamy, N.R. (2001a). "Strip footing on geocell reinforced sand beds with additional planar reinforcement." *Geotextiles and Geomembranes*, Vol. 19, No.8, pp. 529-538.

Dash, S.K., Krishnaswamy, N.R., and Rajagopal, K. (2001b). "Bearing capacity of strip footings supported on geocell-reinforced sand." *Geotextiles and Geomembranes*, Vol. 19 No. 4, pp. 235-256.

Dash, S.K., Sireesh, S., and Sitharam, T.G. (2003). "Model studies on circular footing supported on geocell reinforced sand underlain by soft clay." *Geotextiles and Geomembranes*, Vol. 21, No. 4, pp. 197-219.

Dash, S.K., Rajagopal, K., and Krishnaswamy, N.R.(2004). "Performance of different geosynthetic reinforcement materials in sand foundations." *Geosynthetics International*, Vol. 11, No. 1, pp. 35-42.

De Garidel, R. and Morel, G. (1986). "New soil strengthening techniques by textile elements for low-volume roads." Proceedings of *3rd International Conference on Geotextiles*, pp. 1027-1032.

Duncan, J.M., Byrne, P., Wong, K.S., and Mabry, P. (1980). "Strength, stress-strain and bulk modulus parameters for finite element analyses of stresses and movements in soil masses." *UCB/GT/80-01*, University of California, Berkeley.

Edil, T.B., Benson, C.H,, Shafique, M.S.J., Tanyu, B.F., Kim, W.H. and Senol, A. (2002). "Field evaluation of construction alternatives for roadway over soft subgrade." Preprint CD-ROM of the *81st Transportation Research Board Annual Meeting*, January 13-17, Washington, D.C. USA.

Evan, M.S. (1994). "Geocell mattress effects on the embankments settlements." Proceedings of *Vertical and Horizontal Deformations of Foundations and Embankments Settlement '94*, 584-597.

Fang, H. (2001). Rational approach to rutting rehabilitation decisions. Ph.D. Dissertation, Purdue University, West Lafayette, Indiana.

Gabr, M. (2001). "Cyclic plate loading tests on geogrid reinforced roads." *Research Report to Tensar Earth Technologies, Inc*, North Carolina State University.

Giroud, J.P. and Noiray, L. (1981). "Geotextile-reinforced unpaved road design," *Journal of the Geotechnical Engineering Division*, ASCE Vol. 107, No. GT9, pp. 1233-1254.

Giroud, J.P. and Han, J. (2004a). "Design method for geogrid-reinforced unpaved roads. Part I. Development of Design Method." *ASCE Journal of Geotechnical and Geoenvironment Engineering*, Vol. 130, No. 8, pp. 775-786.

Giroud, J.P. and Han, J. (2004b). "Design method for geogrid-reinforced unpaved roads – Part II: calibration and verification." *ASCE Journal of Geotechnical and Geoenviornmental Engineering*." Vol. 130, No. 8, pp. 787-797.

Gourves, R., Reffsteck, P. and Vignon, J.F. (1996). "Study of confinement effect in geocells." *Geosynthetics: Applications, Design and Construction*, pp. 455-458.

Hadi, M. N. S and Bodhinayake, B. C. (2003). "Non-linear finite element analysis of flexible pavements." *Advances in Engineering Software*, Vol. 34, pp.657-662.

Hammit, G.M. (1970). "Thickness requirement for unsurfaced roads and airfields, bare base support, Project 3782-65." *Technical Report S-70-5*, U.S. Army Engineer Waterways Experiment Station, Vicksburg, Mississippi.

Han, J., Yang, X., Leshchinsky, D., and Parsons, R. (2008a). "Behavior of geocell-reinforced sand under a vertical load." *Transportation Research Record*, Vol. 2045, Transportation Research Board, Record, Washington, D.C., pp. 95-101.

Han, J., Yang, X., Leshchinsky, D., and Parsons, R. (2008b). "Numerical analysis for mechanism of a geocell-reinforced base under a vertical load." Proceeding of *4th Asian Regional Conference on Geosynthetics*, June 17-20, Shanghai, China, pp. 741-746.

Han, J., Pokharel, S.K., Leshchinsky, D., Parsons, R.L., and Halahmi, I. (2010). "Effect of infill material on the performance of geocell-reinforced bases." Proceedings of the *9th International Conference on Geosynthetics*, May 23-27, Brazil.

Han, J., Pokharel, S.K., Yang, X.M., Manandhar, C., Leshchinsky, D., Halahmi, I., and Parsons, R.L. (2011). "Performance of geocell-reinforced RAP bases over weak subgrade under full-scale moving wheel loads." *Journal of Materials in Civil Engineering*, Vol. 23, pp. 1525-1534.

Henkel, D.J., and Gilbert, G.D. (1952). "The effect of the rubber membrane on the measured triaxial compression strength of clay samples." *Geotechnique*, Vol. 3, No. 1, pp. 20-29.

Hua, J. (2000). Finite element modeling analysis of accelerated pavement testing devices and rutting phenomenon. Ph.D. Dissertation, Purdue University, West Lafayette, IN.

Huang, Y. H. (1967). “Stresses and displacements in viscoelastic layered systems under circular loaded areas.” Proceedings of the *2nd International Conference on the Structural Design of Asphalt Pavements*, pp. 225-244.

Huang, Y. H. (1968). “Stresses and displacements in nonlinear soil media.” *Journal of the Soil Mechanics and Foundation Division*, Vol. 97, No. HW2, pp. 115-128.

Huang, H. (1995). Analysis of accelerated pavement tests and finite element modeling of rutting phenomenon. Ph.D. Dissertation, Purdue University, West Lafayette, Indiana.

Huang, B. (2000). Fundamental characterization and numerical simulation of large stone asphalt mixtures. Ph.D. Dissertation, Louisiana State University, Baton Rouge.

Huang, Y. H. (2004). Pavement analysis and design. 2nd edition, *Prentice Hall*, New Jersey.

Jamnejad, G, Kazerani, G., Harvey, R.C., and Clarke, J.D. (1986). “Polymer grid cell reinforcement in pavement construction.” Proceedings of the *2nd International Conference and Bearing Capacity of Roads and Airfields*, Plymouth, U.K., pp. 537-546.

Janbu, N. (1963). “Soil compressibility as determined by oedometer and triaxial tests.” Proceedings of the *European Conference on Soil Mechanics and Foundation Engineering*, Montreal, Germany, pp. 19-25.

Kazerani, G. and Jamnejad, G. (1987). “Polymer grid cell reinforcement in construction of pavement structures.” *Geosynthetics ’87 Conference*, New Orleans, LA. Feb. pp. 56-68.

Kim, M. and Tutumluer, E. (2006). “Modeling nonlinear, stress-dependent pavement foundation behavior using a general-purpose finite element program.” *Geotechnical Special Publication No. 154*, ASCE, Reston, VA, pp.29-36.

Koerner, R.M. (2005). Designing with geosynthetics. Fifth Edition, *Prentice Hall*, New Jersey.

Konder, R.L. (1963). “Hyperbolic stress-strain response: cohesive soils.” *Journal of the Soil Mechanics and Foundations Division*, ASCE, 89 (SM 1), pp. 115-143.

Kraus, H. (1980). Creep Analysis. *John Wiley & Sons, Inc*., New York, N.Y.

Krishnaswamy, N.R., Rajagopal, K. and Madhavi Latha, G., (2000). “Model studies on geocell supported embankments constructed over a soft clay foundation.” *Geotechnical Testing Journal*, Vol.23, No. 1, March, pp. 45-54.

Leshchinsky, B. and Ling, H. (2013). “Effects of geocell confinement on strength and deformation behavior of gravel.” *Journal of Geotechincal and Geoenviromental Engineerin*, Vol. 139, No. 2, pp. 340-352.

Lewis, P. (2008). "Lessons learned from the operations management of an accelerated pavement testing facility." Proceedings of the *3rd Intl. Conference On Accelerated Pavement Testing*, Madrid, Spain, October.

Madhavi Latha, G. and Rajagopal, K. (2007) "Parametric Finite Element Analyses of Geocell Supported Embankments." *Canadian Geotechnical Journal*, Vol. 44, No. 8, pp. 917-927.

Madhavi Latha, G., Rajagopal, K., and Krishnaswamy, N.R. (2006). "Experimental and theoretical investigations on geocell-supported embankments." *International Journal of Geomechanics*, Vol. 6 , No. 1, pp. 30-35.

Madhavi Latha, G., Dash, S.K., and Rajagopal, K. (2008). "Equivalent continuum simulations of geocell reinforced sand beds supporting strip footings." *Geotechnical and Geological Engineering*, Vol. 26, No. 4, pp. 387-398.

Madhavi Latha, G., Dash, S.K. and Rajagopal, K. (2009). "Numerical simulation of the behavior of geocell reinforced sand in foundations." *International Journal of Geomechanics*, Vol.9, No.4, pp.143-152.

Madhavi Latha, G. and Amit Somwanshi (2009) " Effect of reinforcement form on the performance of square footings on sand." *Geotextiles and Geomembranes*, Vol. 27, pp. 409-422.

Mandal, J. N. and Gupta, P. (1994). "Stability of geocell-reinforced soil." *Construction and Building Materials.* Vol. 8, No. 1, pp. 55-62.

MAPA. Asphalt Pavement Recycling Facts. <http://moasphalt.org/facts/environmental/facts.htm> (Sept, 2012).

Mengelt, M., Edil, T.B. and Benson, H.H. (2006). "Resilient modulus and plastic deformation of soil confined in a geocell." *Geosynthetics International*, Vol. 13, No. 5, pp. 195-205.

Mhaiskar, S.Y. and Mandal, J.N. (1992a). "Soft clay subgrade stabilization using geocells." *Geotechnical Special Publication*, Vol. 2, No. 30, pp. 1092-1103.

Mhaiskar, S.Y. and Mandal, J.N. (1992b). "Comparison of a geocell and horizontal inclusion for paved road structure." Proceedings of the *International Symposium on Earth Reinforcement Practice*, Vol. 1, p. 641.

Mhaiskar, S.Y. and Mandal, J.N. (1994). "Three dimensional geocell structure: performance under repetitive loads." Proceedings of *5th International Conference on Geotextile, Geomembranes and Related Products,* Singapore, pp. 155-158.

Mhaiskar, S.Y. and Mandal, J.N. (1996). “Investigations on soft clay subgrade strengthening using geocells.” *Construction and Building Materials*, Vol. 10, No. 4, pp. 281-286.

Mitchell, J.K., Kao, T.C., and Kavazanjian, E. (1979). “Analysis of Grid Cell Reinforced Pavement Bases.” *Report GL-79-8*. Geotechnical Laboratory, U.S. Army Engineer Waterways Experiment Station, Vicksburg, MS.

Moaveni, S. (1999). Finite element analysis: theory and application with ANSYS. *Prentice Hall*, New Jersey.

NCHRP (2002). Simple performance test for superpave mix design. Report 465, Washington, D.C.

NCHRP (2011). Guide for Mechanistic-Empirical Design of New and Rehabilitated Pavement Structures. *ARA, Inc*., ERES Consultants Division, Champaign, IL.

Onyango, M. (2009). Verification of mechanistic prediction models for permanent deformation in asphalt mixes using accelerated pavement testing. Ph.D. Dissertation, Kansas State University, Manhattan.

Perkins, S.W. (2004). Development of design methods for geosynthetic reinforced flexible pavements. *DTFH61-01-X-00068*, Federal Highway Administration, Washington, D.C.

Pokharel, S.K., Han, J., Leshchinsky, D., Parsons, R.L., and Halahmi, I. (2009a). “Experimental evaluation of influence factor for single-geocell-reinforced sand.” Preprint DVD-ROM of the *88th Transportation Research Board Annual Meeting*, January 11-15, Washington, D.C.

Pokharel, S.K., Han, J., Leshchinsky, D., Parsons, R.L., and Halahmi, I. (2009b). “Behavior of geocell-reinforced granular bases under static and repeated loads.” Proceedings of the *International Foundation Congress and Equipment Expo*, March 15-19, 2009, Orlando, Florida.

Pokharel, S.K., Han, J., Parsons, R.L., Qian, Y., Leshchinsky, D., and Halahmi, I. (2009c). “Experimental study on bearing capacity of geocell-reinforced bases.” Proceedings of the *8th International Conference on the Bearing Capacity of Roads and Airfields*, June 29-July 2, Champaign, Illinois.

Pokharel, S.K., Han, J., Leshchinsky, D., Parsons, R.L., and Halahmi, I. (2010). “Investigation of factors influencing behavior of single geocell-reinforced bases under static loading.” *Geotextiles and Geomembranes*, Vol. 28, No. 6, pp. 570-578.

Pokharel S.K. (2010). Experimental study on geocell-reinforced bases under static and dynamic loading. Ph.D. Dissertation, University of Kansas, Lawrence.

Pokharel, S.K., Han, J., Manandhar, C., Yang, X.M., Leshchinsky, D., Halahmi, I., and Parsons, R.L. (2011). "Accelerated pavement testing of geocell-reinforced bases over weak subgrade." Proceedings of the *10th International Conference on Low-Volume Roads*, July 24–27, Lake Buena Vista, Florida, USA.

Rajagopal, K., Krishnaswamy, N.R. and Latha, G.M. (1999). "Behavior of sand confined with single and multiple geocells." *Geotextiles and Geomembranes*, Vol. 17, No. 3, pp. 171-184.

Rea, C. and Mitchell, K. (1978). "Sand reinforcement using paper grid cells." Proceedings of the *Symposium on Earth Reinforcement, ASCE Annual Convention*, Pittsburgh, PA. pp. 644-663.

Rodriguez-Roa, F. (2000). "Observed and calculated load-settlement relationship in a sandy gravel." *Canadian Geotechnical Journal*, Vol. 37, pp.333-342.

Sekine, E., Muramoto, K., and Tarumi, H. (1994). "Study on properties of road bed reinforced with geocell." *Quarterly Report of RTRI (Railway Technical Research Institute) (Japan)*, Vol. 35, No. 1, pp. 23-31.

Sharp, R., and Booker, J. (1984). "Shakedown of pavement under moving surface loads." *Journal of Transportation Engineering*, Vol. 110, No. 1, pp. 1-14.

Shimizu, M. and Inui, T. (1990). "Increasing the bearing capacity of ground with geotextile wall frame." *Geotextiles, Geomembranes and Related Products*, pp. 254.

Sitharam, T.G, Sireesh, S., and Dash, S.K. (2005). "Model studies of a circular footing supported on geocell-reinforced clay." *Canadian Geotechnical Journal*, Vol. 42, No. 2, pp. 693-703.

Simulia (2011). Abaqus analysis user's manual. Dassault Systemes.

Sivasubramaniam, S. (2005). Validation of Superpave mixture design and analysis procedure using the NCAT test track. Ph.D. Dissertation, Purdue University, West Lafayette, Indiana.

Tingle, J.S. and Jersey, S.R. (2007). "Empirical design methods for geosynthetic-reinforced low-volume roads." *Journal of the Transportation Research Board*, Vol. 1989, No. 2, pp. 91-101.

TxDOT (2008). ftp://ftp.dot.state.tx.us/pub/txdot-info/cst/tips/falling_weight_deflectometer.pdf

Webster, S. L. and Watkins, J. E. (1977). Investigation of Construction Techniques for Tactical Approach Roads Across Soft Ground. *Report S-77-1*. Soils and Pavements Laboratory, U.S. Army Engineer Waterways Experiment Station, Vicksburg.

Webster, S. L. and Alford, S. J. (1978). Investigation of Construction Concepts for Pavements Across Soft Ground. *Report S-78-6*. Geotechnical Laboratory, Waterways Experiment Station, U.S. Army Corps of Engineers, Vicksburg, MS.

Webster, S. (1979a). Investigation of beach sand trafficability enhancement using sand-grid confinement and membrane reinforcement concepts; report 1, sand test sections 1 and 2. *Technical report GL-79-20*. Waterways Experiment Station Geotechnical Laboratory, U.S. Army Corps of Engineers, Vicksburg, MS.

Webster, S. L. (1979b). Investigation of beach sand trafficability enhancement using sand-grid confinement and membrane reinforcement concepts. *Report GL-79-20 Report 2*, U.S. Army Engineer Waterways Experiment Station, U.S. Army Corps of Engineers, Vicksburg, MS.

Webster, S. L. (1986). Sand-Grid Demonstration Roads Constructed for JLOTS II Tests at Fort Story, Virginia. *Technical Report GL-86-19*, U.S. Army Corps of Engineers, U.S. Army Corps, Vicksburg, MS..

Werkmeister, S., Dawson, A.R., and Wellner, F. (2003). "Design concepts of unbound granular layers in pavement constructions." Proceedings of the *21st ARRB and 11th REAA Conference*, Cairns, Australia.

WSDOT (2005). http://www.wsdot.wa.gov/NR/rdonlyres/0C02BB7B-C345-4958-AA08-089E5E512B96/0/EverseriesUserGuidePart1.pdf

Wu, Z. (2001). Finite element simulation of rutting on superpave pavements. Ph.D. Dissertation, Kansas State University, Manhattan.

Wu, Z., Chen, X., Yang, X., and Zhang, Z. (2011). "A finite element model for rutting prediction of flexible pavement with cementitiously-stabilized base/subbase." Preprint DVD-ROM of the *90th Transportation Research Board Annual Meeting*, Jan. 23-27, Washington, D.C..

Yang, X. (2010). Numerical analyses of geocell-reinforced granular soils under static repeated loads. Ph.D. Dissertation, University of Kansas, Lawrence.

Yuu, J., Han, J., Rosen, A., Parsons, R.L., and Leshchinsky, D. (2008). "Technical review of geocell-reinforced base courses over weak subgrade." Proceedings of the *First Pan American Geosynthetics Conference & Exhibition*, March 2-5, Cancun, Mexico.

Zhao, Y. (2002). Permanent deformation characterization of asphalt concrete using a viscoplastic model. Ph.D. Dissertation, North Carolina State University, Raleigh.

Zhou, H. and Wen, X. (2008). “Model studies on geogrid-or geocell-reinforced sand cushion on soft soil.” *Geotextile and Geomembranes*, Vol. 26, No. 3, pp. 231-238.

Appendix A - **Numerical Analysis Profiles**

The figures in the appendix show profile results of numerical analysis. Each figure shows simulated rut profiles at 100,000, 500,000, and 1,000,000 cycles. The conversion factor is 25.4 mm to 1 inch.

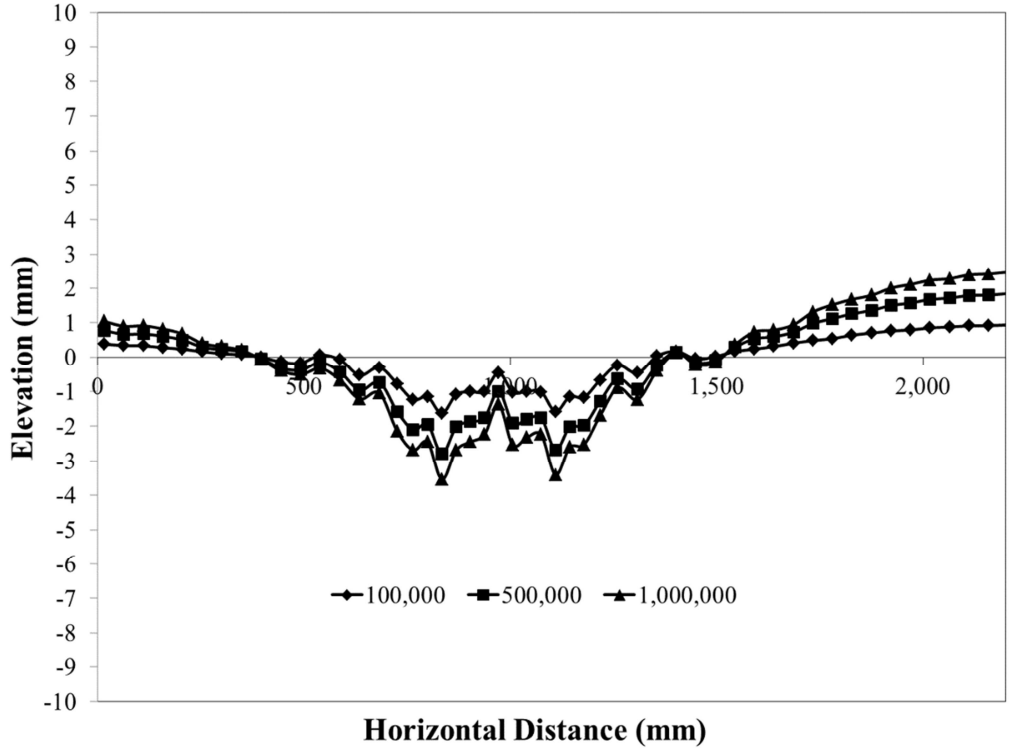

Figure A-1 Simulated control rut profiles for first test

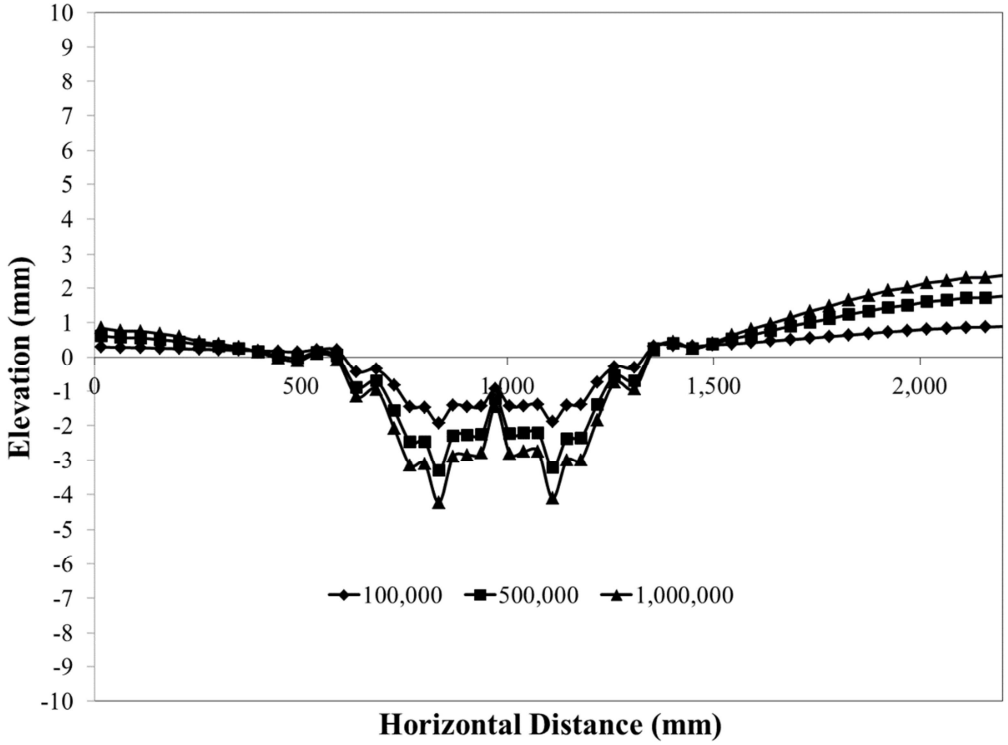

Figure A-2 Simulated control rut profiles for overlay test

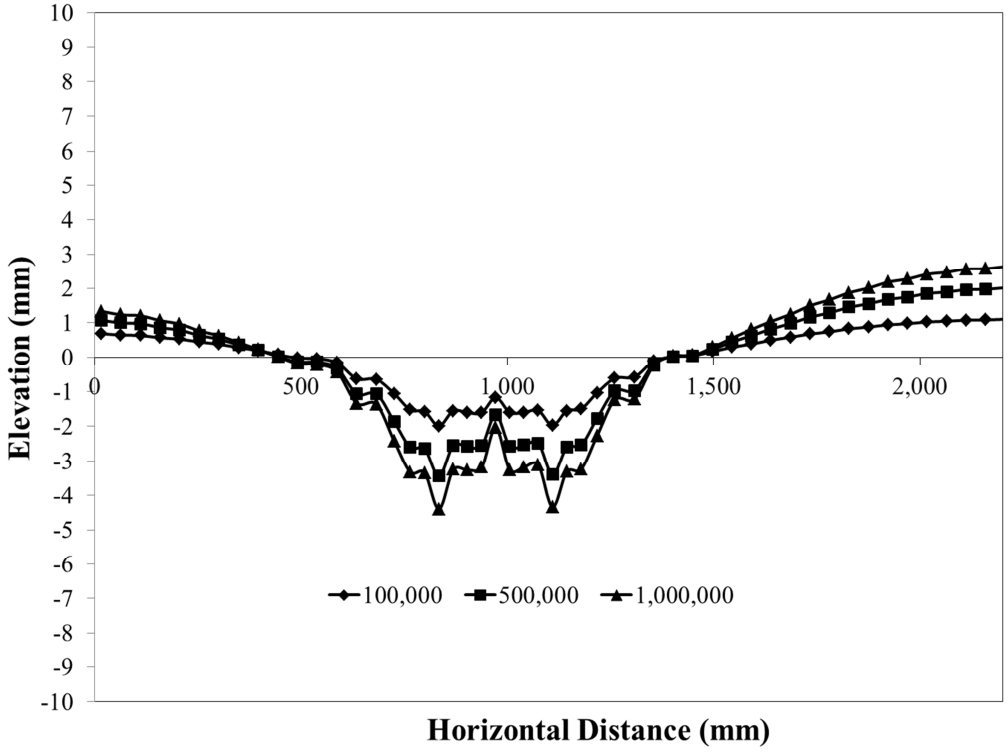

Figure A-3 Simulated control rut profiles for second test

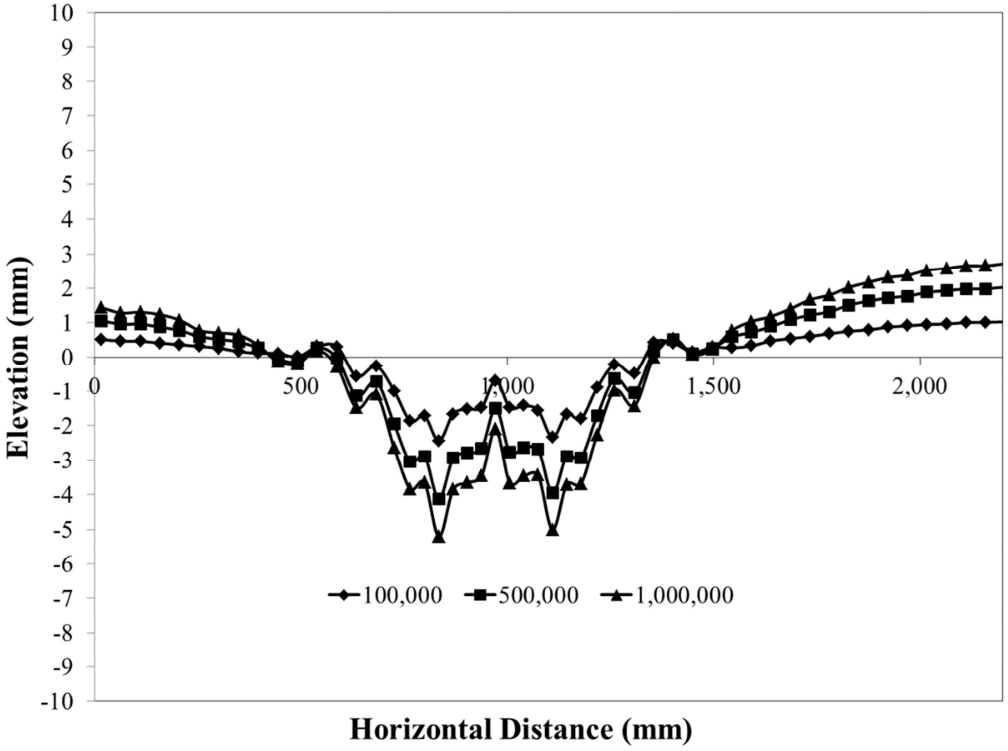

Figure A-4 Simulated quarry waste rut profiles for first test

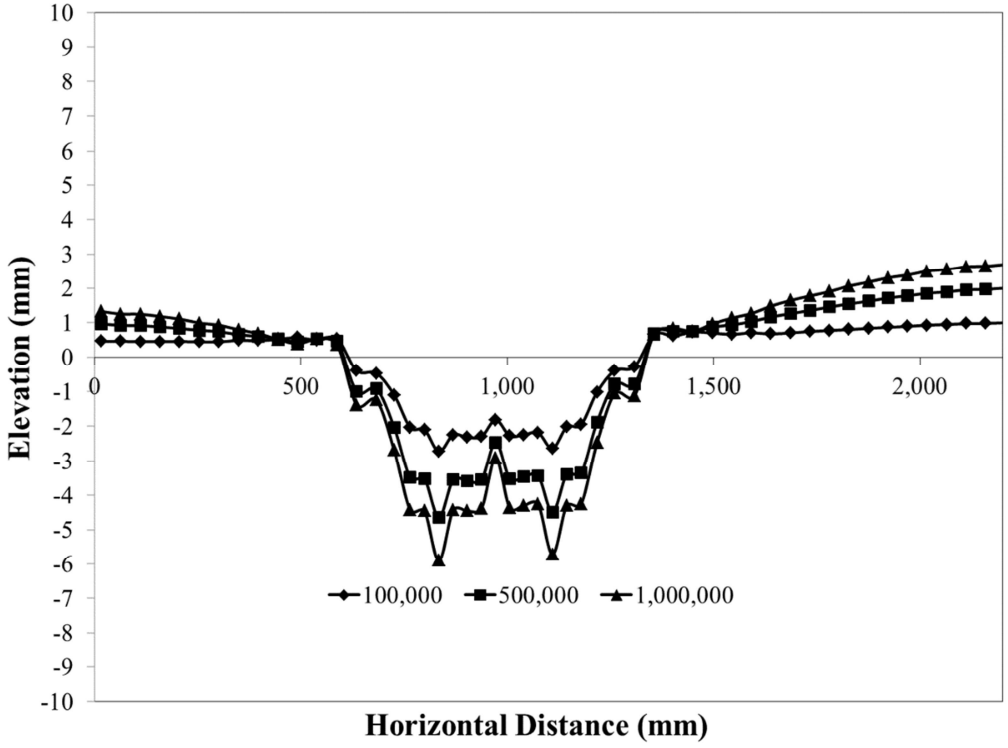

Figure A-5 Simulated quarry waste rut profiles for overlay test

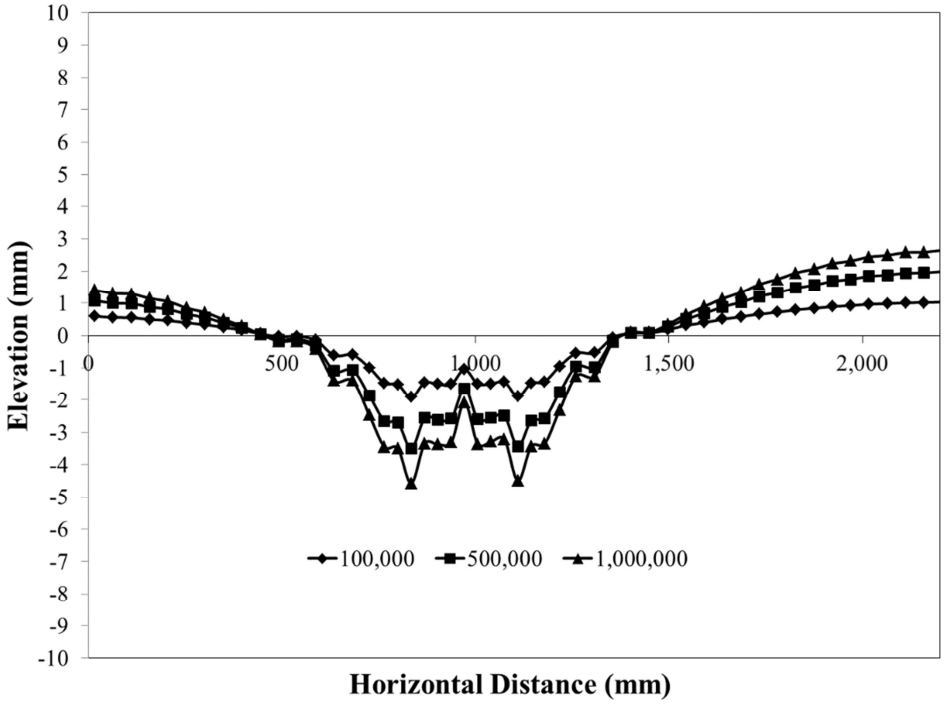

Figure A-6 Simulated quarry waste rut profiles for second test

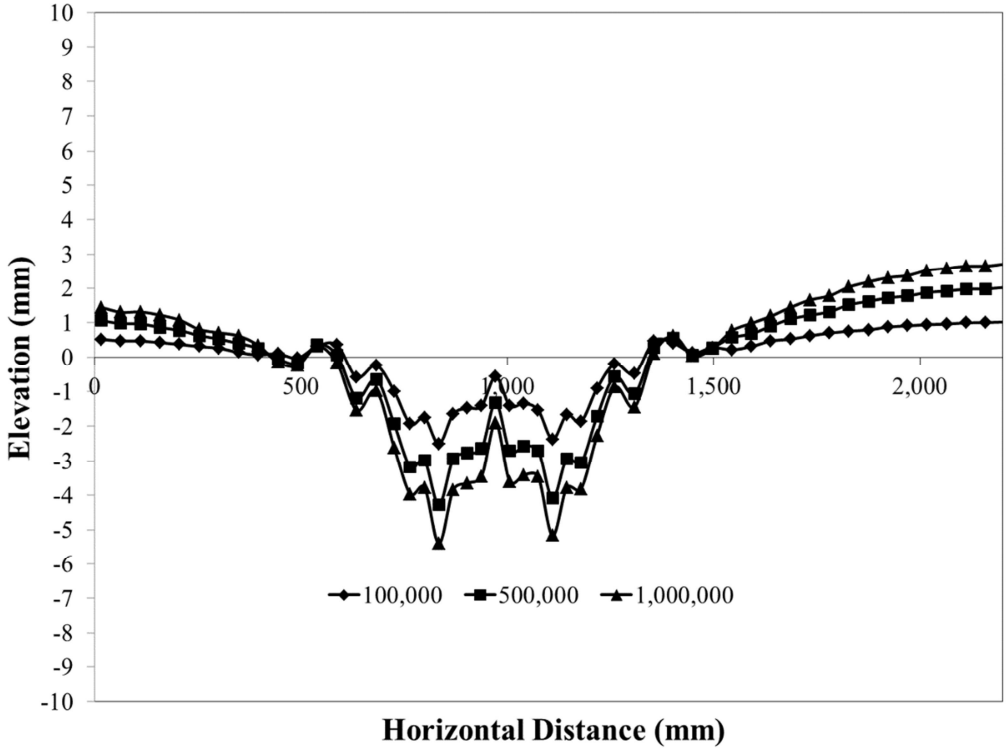

Figure A-7 Simulated RAP rut profiles for first test

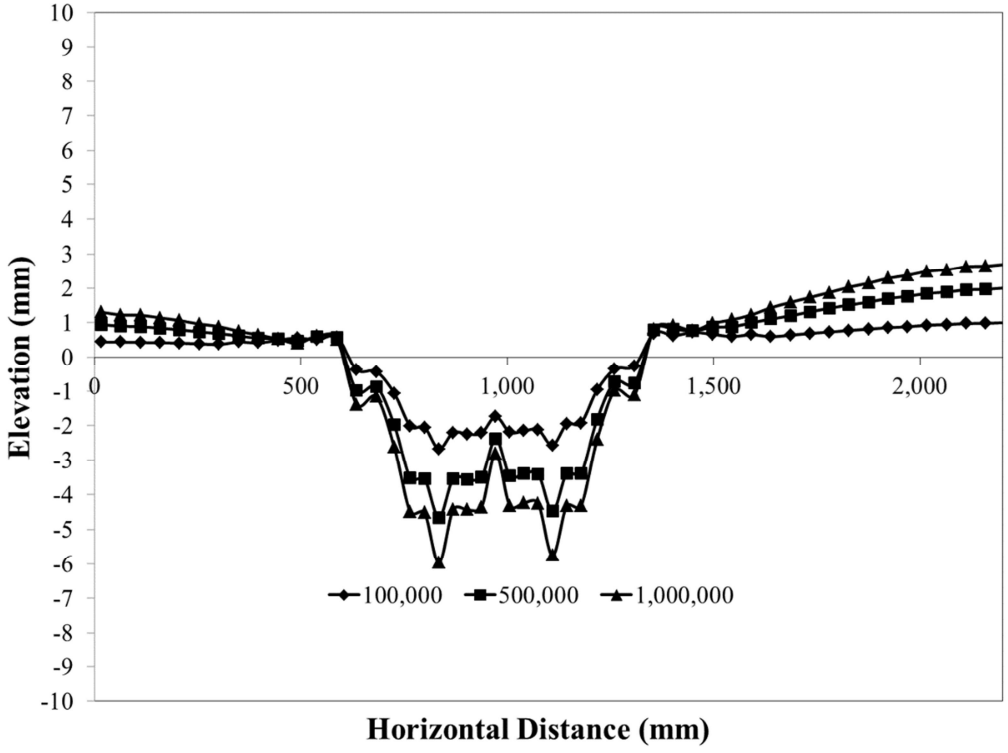

Figure A-8 Simulated RAP rut profiles for overlay test

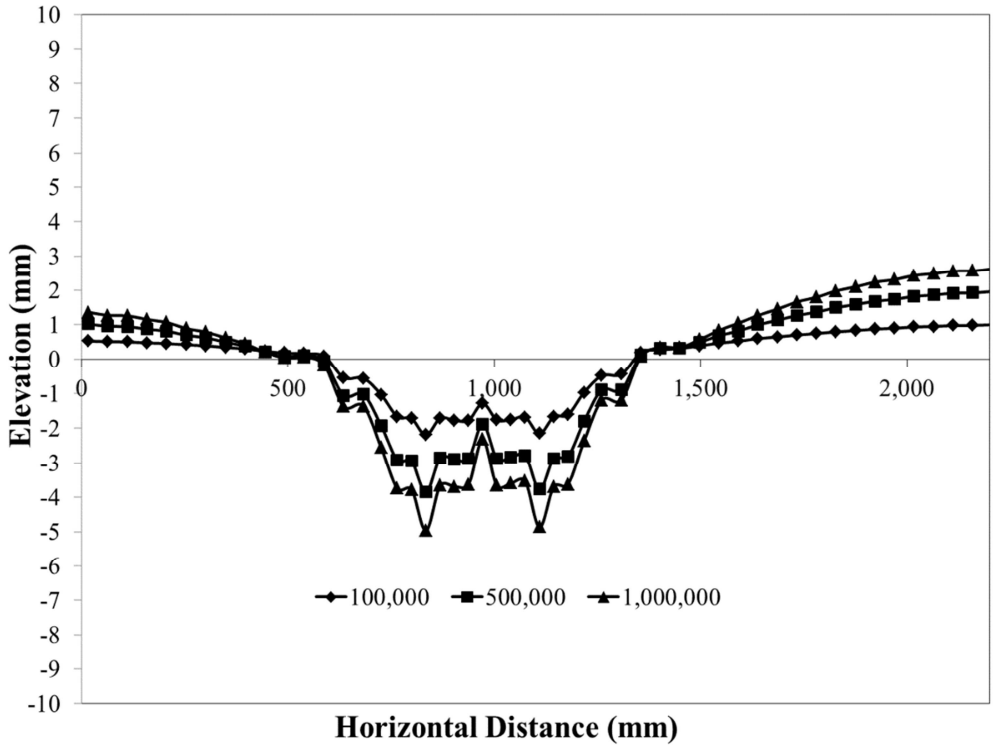

Figure A-9 Simulated RAP rut profiles for second test

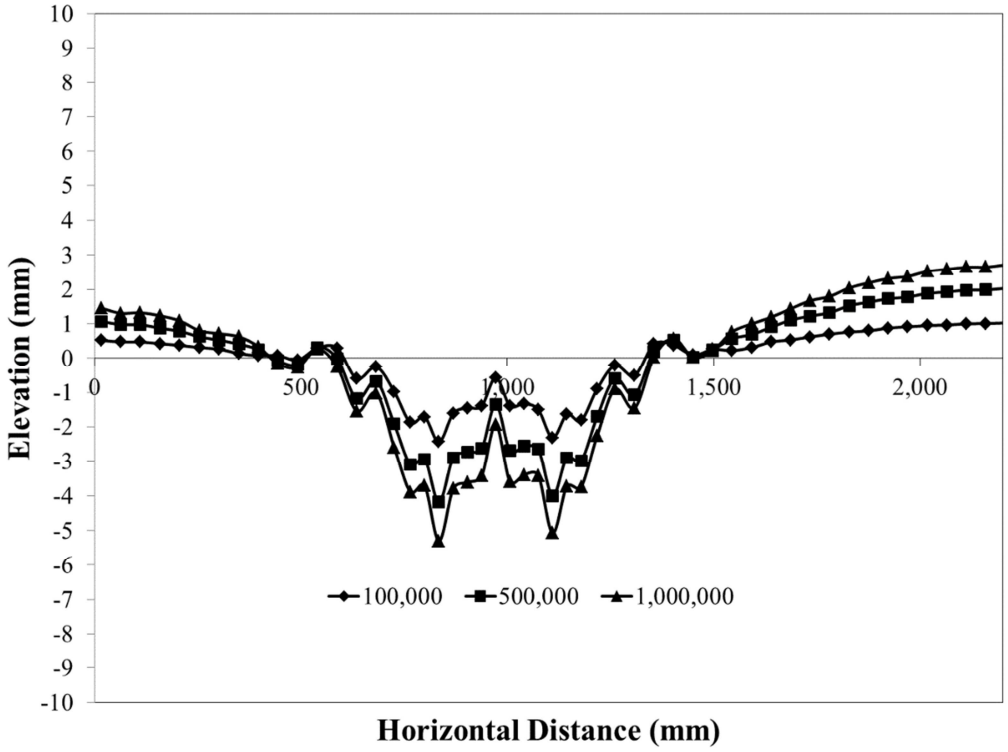

Figure A-10 Simulated AB3 rut profiles for first test

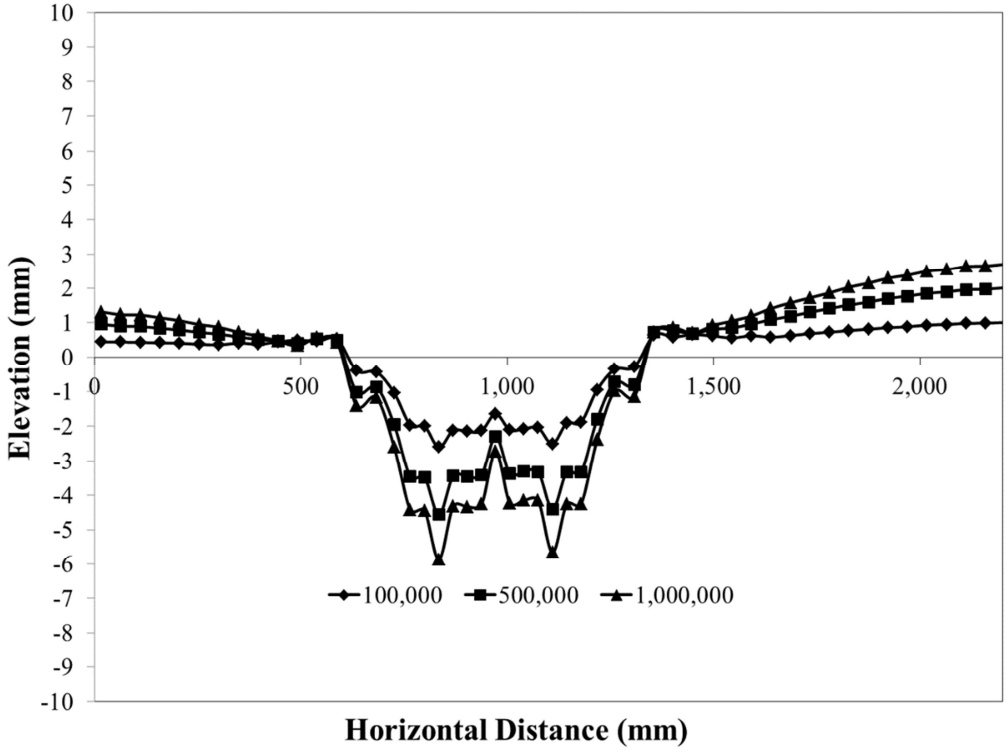

Figure A-11 Simulated AB3 rut profiles for overlay test

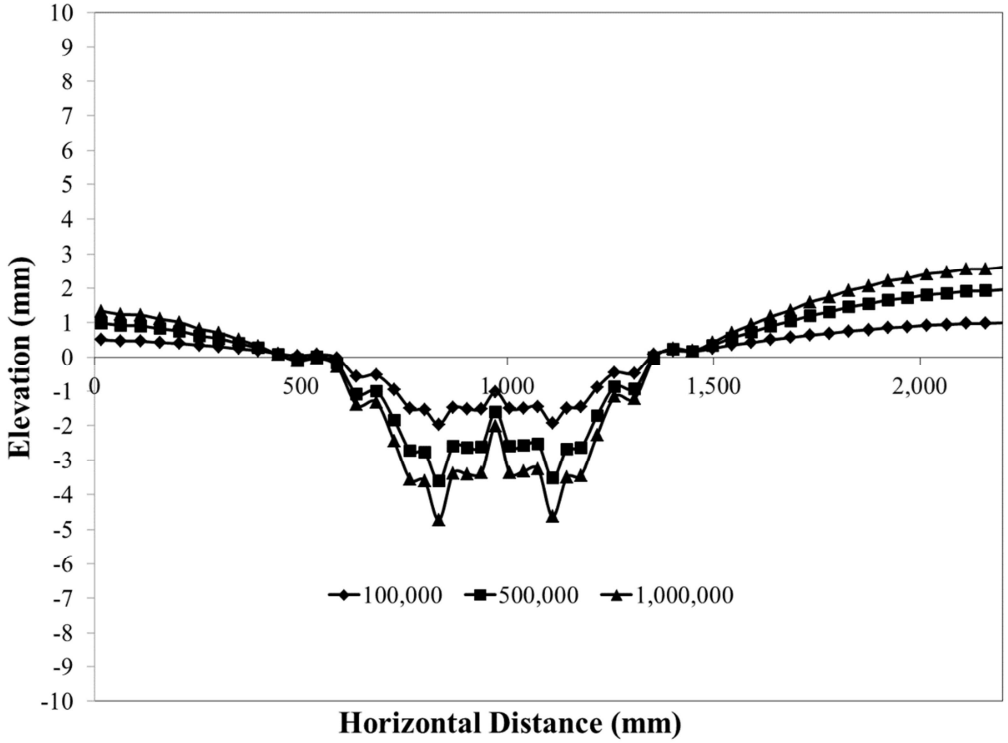

Figure A-12 Simulated AB3 rut profiles for second test